UTS UNIVERSITY OF TECHNOLOGY SYDNEY

Atmospheric Water Harvesting with Polymeric Hydrogels

by An Feng

Thesis submitted in fulfilment of the requirements for
the degree of

Doctor of Philosophy

under the supervision of Associate Professor Qiang Fu and
Professor Long D. Nghiem

University of Technology Sydney
Faculty of Engineering and Information Technology

February 2025

Certificate of Original Authorship

I, An Feng, declare that this thesis is submitted in fulfilment of the requirements for the degree of Doctor of Philosophy, in the School of Civil and Environmental Engineering, Faculty of Engineering and Information Technology at University of Technology Sydney.

This thesis is wholly my own research work unless otherwise referenced or acknowledged. In addition, I certify that all information sources and literature used are indicated in the thesis.

This document has not been submitted for qualifications at any other academic institution.

This research is supported by the Australian Government Research Training Program.

Signature: Production Note: Signature removed prior to publication.

Date: 01/02/2025

Acknowledgements

First and foremost, I would like to extend my sincerest gratitude to Associate Professor Qiang Fu, my principal supervisor throughout my doctoral study at the Faculty of Engineering and IT, University of Sydney. Associate Professor Fu is a dedicated and passionate academic, characterized by his meticulousness in scholarly research and his approachable demeanor towards students, demonstrating a profound sense of responsibility. In the tumultuous year of 2020, his academic guidance and unwavering support served as invaluable pillars, enabling me to navigate through the challenges posed by the COVID-19 pandemic. Without Associate Professor Fu's assistance, I would not have been able to complete my doctoral studies. Additionally, I wish to express my gratitude to my co-supervisor, Professor Long D. Nghiem. Professor Long is a friendly person, and I am deeply impressed by his academic advice and support. It was my great honor to complete my PhD under their supervision.

Secondly, I would like to thank my four group members, including Miss. Shudi Mao, Miss. Yihan Shi, Miss. Stella (Xin) Zhang, and Mr. Casey Onggowarsito. Their help and support to me is not only reflected in scientific research, but also integrated into my daily life. I would also like to say thank you to my friends at FEIT including Dr. Huan Liu, Dr. Lan Wu, Miss. Ting Zhou, Dr. Chen Wang, Mr. Jiaqi Zhang, Mr. Xingdong Shi, Mr Jibin Li, Mr. Haoding Xu, Dr. Derek (Qiang) Hao, Dr. Zehao Zhang, Dr. Feng Shan, Dr. Li Wang, Dr. Fulin Qu, Dr. Bing Zhang, Dr. Xuan Zhang, Mr. Chao Mai, Mr. Ramos (Xuqun) Lin, Miss. Lehan Chen, Miss. Jinru Xue, Mr. Yipu Guo, Mr. Qingyun Wu etc.

They brought me a lot of warmth and happiness during my PhD study.

Thirdly, I would like to thank the UTS laboratory technical support officers, including Dr. Mohammed AH. Johir, Dr. Nirenkumar Pathak, Dr. Herbert Yuan, and Dr. Linda Xiao. It was they who taught me how to operate SEM, FTIR, Raman, NMR, ICP-MS and other laboratory characterization instruments, allowing me to know the testing methods well during my research.

Fourthly, I would like to express my gratitude to my parents, Mr. Bo Feng and Mrs. Xiaoqin Huang, thanks to them for their help, encouragement, and endless love over the past 29 years.

List of Publications

1. **Feng, A**., Akther, N., Duan, X., Peng, S., Onggowarsito, C., Mao, S., ... & Kolev, S. D. (2022). Recent development of atmospheric water harvesting materials: a review. *ACS Materials Au*, 2(5), 576-595.
2. **Feng, A**., Onggowarsito, C., Mao, S., Qiao, G. G., & Fu, Q. (2023). Divide and Conquer: A Novel Dual-Layered Hydrogel for Atmospheric Moisture Harvesting. *ChemSusChem*, 16(14), e202300137.
3. **Feng, A**., Mao, S., Onggowarsito, C., Naidu, G., Li, W., & Fu, Q. (2023). Tillandsia-inspired composite materials for atmospheric water harvesting. *ACS sustainable chemistry & engineering*, 11(15), 5819-5825.
4. **Feng, A**., Shi, Y., Onggowarsito, C., Zhang, X. S., Mao, S., Johir, M. A., ... & Nghiem, L. D. (2024). Structure-Property Relationships of Hydrogel-based Atmospheric Water Harvesting Systems. *ChemSusChem*, e202301905.
5. Shi, Y., **Feng, A**., Mao, S., Onggowarsito, C., Zhang, X. S., Guo, W., & Fu, Q. (2024). Hydrogels in solar-driven water and energy production: Recent advances and future perspectives. *Chemical Engineering Journal*, 152303.
6. Mao, S., **Feng, A**., Zhang, S., Onggowarsito, C., Chen, Q., Su, D., & Fu, Q. (2023). Investigation of structure–property–application relationships of a hydrogel-based solar vapor generator. *Journal of Materials Chemistry A*, 11(42), 23062-23070.
7. Onggowarsito, C., **Feng, A**., Mao, S., Zhang, S., Ibrahim, I., Tijing, L., ... & Ngo, H. H. (2022). Development of an innovative MnO_2 nanorod for efficient solar vapor generator. *Environmental Functional Materials*, 1(2), 196-203.

8. Onggowarsito, C., **Feng, A**., Mao, S., Nguyen, L. N., Xu, J., & Fu, Q. (2022). Water harvesting strategies through solar steam generator systems. *ChemSusChem*, 15(23), e202201543.
9. Mao, S., Onggowarsito, C., **Feng, A**., Zhang, S., Fu, Q., & Nghiem, L. D. (2023). A cryogel solar vapor generator with rapid water replenishment and high intermediate water content for seawater desalination. *Journal of Materials Chemistry A*, 11(2), 858-867.
10. Mao, S., Johir, M. A. H., Onggowarsito, C., **Feng, A**., Nghiem, L. D., & Fu, Q. (2022). Recent developments of hydrogel based solar water purification technology. *Materials Advances*, 3(3), 1322-1340.
11. Onggowarsito, C., Mao, S., Zhang, X. S., **Feng, A**., Xu, H., & Fu, Q. (2024). Updated Perspective on Solar Steam Generation Application. *Energy & Environmental Science*.
12. Zhang, X. S., Mao, S., Wang, J., Onggowarsito, C., **Feng, A**., Han, R., ... & Huang, Z. (2024). Boron nanosheets boosting solar thermal water evaporation. *Nanoscale*, 16(9), 4628-4636.

List of Acronyms

AWH	Atmospheric Water Harvesting
AEtMA	[2-(acryloyloxy)ethyl]trimethylammonium chloride solution
APtMA	(3-acrylamidopropyl) trimethylammonium chloride solution
AMPS	2-acrylamido-2-methyl-1-propanesulfonic acid
BiC	Bioinspired Composite
COFs	Covalent-Organic Frameworks
CCW	Conical Copper Wire
CNT	Carbon Nano tube
DLP	Digital Light Processing
DLH	Dual-Layered Hydrogel
DAA	Diacetone acrylamide
EPD	Electrostatic Potential Difference
HICs	Hygroscopic Inorganic Compounds
ILs	Ionic Liquids
LHL	Light-to Heat Layer
LCST	Lower Critical Solution Temperature
MOFs	Metal-Organic Frameworks
MWCO	Molecular Weight Cut-Off
MMFF	Merck Molecular Force Field
NPs	Nanoparticles
PAN	Polyacrylonitrile
PMMA	Poly(methylmethacrylate)
PP	Polypropyene
POG	Photothermal Organogel
PDA	Polydopamine
PTM	Photothermal Material
SR	Swelling Ratio
SA	Sodium Alginate
SVG	Solar Vapor Generation
TEMED	N,N,N′,N′-tetramethylethylenediamine
WAL	Water Adsorption Layer
XL	Crosslinker

List of Tables

List of Figures

Table of Contents

Abstract

Water is essential for life, playing critical roles in maintaining electrolyte balance and excreting metabolites in the human body. However, despite Earth's abundant water resources, only a tiny fraction is accessible, with surface freshwater, atmospheric water vapor, and shallow groundwater comprising less than 0.03% of total water. Geographic and climatic factors result in 2.8 billion people in 48 countries, especially in Africa, the Middle East, and Oceania, experiencing freshwater scarcity, a number projected to reach 4 billion. Although the utilization of solid and liquid water is common, capturing atmospheric water vapor has been largely overlooked. Traditional methods such as dew collection, seawater desalination, and river diversion are expensive, maintenance-intensive, and environmentally detrimental. Atmospheric water harvesting (AWH) systems, employing chemical water adsorption materials like structured surface materials, metal-organic frameworks (MOFs), and functional hydrogels, offer a promising alternative. These materials leverage properties such as Laplace pressure gradients and tunable intermolecular spaces to efficiently harvest atmospheric water, providing a low-cost, energy-efficient solution.

Despite the potential of various chemical water adsorption materials like inorganic hygroscopic salts and MOFs, challenges remain, including unstable physical forms, difficult residual water separation, and ion leaching. Hydrogel-based water vapor adsorption materials, when combined with single-stage solar distillation, emerge as a promising next-generation AWH solution.

This thesis explores hydrogel-based AWH composite materials, focusing on the relationship between structure and properties, the thermodynamics and kinetics of adsorption/desorption, and the biomimetic structures of hydrogels. It also includes a preliminary design of an AWH device based on engineering heat-mass transfer principles. The chemical structure of polymer networks, including crosslink density and functional groups, significantly influences the water vapor adsorption kinetics of hydrogels. On a macroscopic level, pore size, density, and wall thickness are shaped by hydrogel chemistry and processing techniques, which jointly affect adsorption kinetics. The unique desorption process in hydrogels is thermodynamically distinct, requiring more energy due to the higher evaporation enthalpy associated with breaking hydrogen bonds. Additionally, double-layered composite hydrogel materials show a 58.71% increase in water adsorption capacity compared to single-layered hybrids, highlighting the efficacy of independent functional components. A 3D printed hydrogel with customized morphology is tested in an AWH device, demonstrating that hydrogel-based AWH materials meet the preliminary requirements for commercialization.

Keywords: Atmospheric water harvesting, Structure-property relationship, Multilayer material, Adsorption/desorption kinetics, 3D-Printing

Chapter 1 Introduction

1.1 Background

The water content in the Earth's atmosphere accounts for 3% of the total freshwater on the surface, approximately 1.31 × 10^{11} tons. The concentration of this water in the air is mainly influenced by temperature and humidity, existing in the forms of saturated water (fog) and unsaturated water (water vapor). Although atmospheric fog collection yields high water production, requires simple equipment, and has low construction/maintenance costs, its widespread application in different regions throughout all weather conditions is hindered by stringent atmospheric conditions. Moreover, there has been almost no large-scale commercialization of devices for harvesting unsaturated water to date.

The lack of efficient and low-cost AWH devices has led to heavy reliance on reverse osmosis membrane seawater desalination technology in the Middle East, as well as the continued deterioration of water scarcity issues in impoverished regions. Against this backdrop, the development of advanced materials for AWH has become a hot topic in the 21st-century environmental engineering field. So far, novel materials with proven water adsorption capabilities under unsaturated air conditions include partial metal-organic frameworks (MOFs), covalent organic frameworks (COFs), hygroscopic inorganic compounds (HICs), ionic liquids (ILs), and inorganic oxides (IOs). However, MOF materials among them are difficult to store, with a challenging control over specific surface area, and exhibit complex water behavior within the material. HICs have a closer connection with water molecules that are hard to separate, and inorganic oxides have relatively small water adsorption capacities. These characteristics have hindered the commercial application of these materials. Therefore, an integrated composite material with high efficiency, large capacity for water adsorption/storage, and rapid desorption is considered to further reduce costs, enhance the water adsorption capacity per unit time, and promote the commercial application of AWH technology.

Hydrogels are hydrophilic polymer networks with swelling characteristics and customizable functionalities, thus possessing the capability to be endowed with water vapor adsorption, high-capacity water storage, and environmentally responsive functions. In existing literature, functionalized hydrogels based on polyacrylamide (PAM) or sodium alginate (SA) have achieved high water adsorption capacities of 1.2-2 g g^{-1} at 60% relative humidity (RH) and over 3 g g^{-1} at 90% RH. Moreover, they reached desorption temperatures of 75 °C and 60 °C under sunlight irradiation, respectively[1-2]. Additionally, hydrogels incorporating chlorine-doped polypyrrole (PPy-Cl) achieved a water adsorption capacity of 3.1 g g^{-1} at 60% RH and released over 85% of stored water after 1.5 h of sunlight exposure[3]. Compared to other AWH materials such as hygroscopic salts, hygroscopic oxides, and ionic liquids, these materials offer significant advantages including lightweight, low cost, and simple installation and maintenance of auxiliary equipment.

Indeed, the research on hydrogel AWH materials has shown an explosive growth due to the advantages of easy fabrication method, low cost, high AWH performance and easy scaling up of the device. However, there is still a knowledge gap in the detailed thermodynamics and kinetics of the adsorption-desorption processes of hydrogel AWH materials. For example, no fundamental studies have been conducted on the chemical structure-property relationships of hydrogel materials and the thermodynamics of water molecules during desorption/evaporation process. In addition, the vast majority of AWH materials are hybrid hydrogels prepared by simply incorporating a hygroscopic salt that facilitates adsorption and a photothermal material that facilitates desorption into hydrophilic polymer network. This configuration may cause these components to interfere with each other, resulting in compromised performance. For example, hygroscopic salt additives used for vapor liquefaction should be exposed to air as much as possible to maximize adsorption properties, but the fact is that they are often encapsulated in hydrogels.

Therefore, for the development of next-generation AWH materials, the following issues urgently required to be investigated:

- The effect of different chemical structures (e.g. functional groups) on the adsorption properties of hydrogel AWH materials.
- Phase change and energy required (e.g. enthalpy of evaporation) for water desorption and a microscopic interpretation of desorption kinetics.

  AWH performance of novel Janus hydrogel material, which consists of an adsorption surface and a desorption surface to ensure that the two processes of adsorption/desorption do not interfere with each other.

1.2 Research Objectives

The aim of this PhD research project is to investigate the adsorption/desorption mechanisms of hydrogel-based AWH composite materials and to demonstrate novel engineering strategies to optimize the performance of AWH hydrogels. This includes four sub-objectives:

1. To comprehensively study the water adsorption behavior during AWH process through the intrinsic properties of the microscopic chemical structure and functional groups of the polymer precursors, as well as the macroscopic pore structure of the AWH hydrogels.

2. To fully elucidate the desorption thermodynamics of AWH hydrogels by examining the state of water (e.g. free water or intermediate water) stored in the hydrogel and their enthalpy of evaporation.

3. To maximize the AWH performance of hydrogel materials by making the water adsorption and desorption functions independent of each other through a ‘divide-and-conquer’ strategy.

4. To develop an AWH device with high energy efficiency and high water production rate through engineering design, and to explore the potential for future commercialization of AWH technology.

1.3 Thesis Outline

This thesis is structured into seven chapters, as outlined below:

Chapter 1: Introduction: This chapter highlights the global water crisis and the limited applications of AWH technologies, and then discusses the characteristics, current applications, and the challenges faced in the development of hydrogel AWH materials. Research objectives are also included.

Chapter 2: Literature Review: This chapter reviews the development of AWH materials over the past two decades as well as compares their AWH properties, positioning AWH technology as an emerging research area.

Chapter 3: A comprehensive investigation of the chemical structure-property relationships of AWH hydrogels at the molecular level. In this chapter, the effects of the chemical structure and functional groups of a variety of AWH hydrogels on the water adsorption properties are investigated by molecular simulation methods as well as experimental methods.

Chapter 4: The desorption process of different AWH hydrogels was investigated from a thermodynamic point of view. In this chapter, the ratios of free, intermediate and bound water in different hydrogels were measured by Raman spectroscopic and DSC thermal analysis methods, and different enthalpy of evaporation were determined to analyze the desorption process of hydrogels thermodynamically.

Chapter 5: Janus Hydrogel: The adsorption and desorption functions of AWH hydrogels are realized independently through a ‘divide-and-conquer’ strategy. This chapter describes the development of a new Janus hydrogel (dual layer hydrogel) and investigates the adsorption/desorption behavior of this AWH material, demonstrating the positive impact of the "independent functions" on the performance of AWH materials.

Chapter 6: Inspired by biomimetic structures, this chapter describes the utilization of nonwoven fibers as carriers of hygroscopic salts to overcome the significant axial stresses exerted on the polymer network by the hydrogel swelling behavior, thus effectively enhance the physical strength of the Janus (dual layer) hydrogels.

Chapter 7: Conclusion and Outlook. This chapter summarizes the key findings from all preceding chapters and provides perspectives for the development of next generation, cost-effective AWH materials and AWH devices.

The illustration of thesis outline is also provided as **Figure 1.1**.

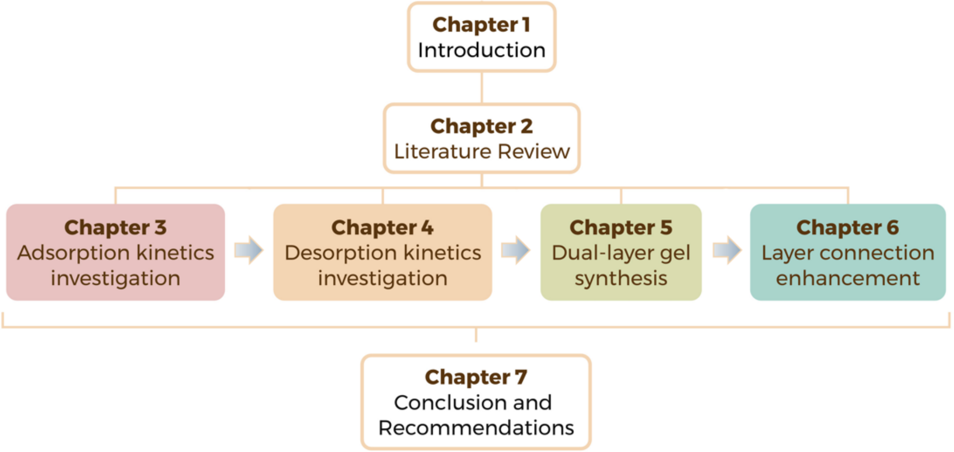

Figure 1.1 Detailed thesis outline diagram

Chapter 2 Literature Review

Related publication:

Feng, A., Akther, N., Duan, X., Peng, S., Onggowarsito, C., Mao, S., ... & Kolev, S. D. (2022). Recent Development of Atmospheric Water Harvesting Materials: A Review. *ACS Materials Au*, 2(5), 576-595.

This chapter provides a comprehensive overview of recent advancements in materials for atmospheric water harvesting (AWH), highlighting innovations in hydrogels, metal-organic frameworks, and ionic liquids that enhance water adsorption capabilities. While the chapter effectively presents the technological progress in AWH, it also identifies gaps, particularly in addressing the challenges related to material scalability and environmental impact. For AWH technologies to become sustainable, long-term solutions to water scarcity, future research must focus on overcoming these challenges and incorporating antibacterial properties to ensure functionality in outdoor environments. Such developments are crucial for advancing the field toward practical, sustainable applications.

2.1 Introduction

Water is essential for all life on Earth, crucial for maintaining human electrolyte balance, and excreting unwanted metabolites. Although Earth's water resources are vast (ca. 1.46 × 10^{16} cubic meters), 99.97% is seawater or deep groundwater, leaving less than 0.03%

easily accessible [4-6]. This accessible water includes surface freshwater, water vapor, and shallow groundwater. Currently, freshwater shortages affect 2.8 billion people in 48 countries, a figure potentially rising to 4 billion, especially in Africa, the Middle East, and Oceania [7-8]. Therefore, next-generation freshwater harvesting technologies with low cost, high adsorption capacity, and ease of use are increasingly vital globally.

Water exists in air as solid (e.g., snow, hail), liquid (e.g., rain, dew), and gas (e.g., vapor). Historically, humans utilized solid and liquid forms but overlooked gaseous water. Modern constraints in geography, technology, and climate affect water conservation in deserts and wastelands. Methods like active dew collection (e.g., electricity-driven condensers), water transfer facilities, and seawater desalination require high investments [9-10], maintenance [11], operational costs [12-13], high environmental impacts, inflexible installation (fixed location), environmental impacts, inflexible installations, and intermittent supply [14]-[15]. Recently, 'passive' water production technologies gained attention for not consuming secondary energy. Solar vapor generators (SVGs), comprising hydrophilic matrix and photothermal materials, float on water surfaces to produce clean water using solar energy [16-17]. Additionally, synthetic materials for AWH are promising due to low cost, low energy use, ease of installation, and high performance, especially when rapid harvesting or insufficient electricity is required [18]. Chemically designed AWH materials, including structured surfaces, metal-organic frameworks (MOFs), hygroscopic inorganic compounds (HICs), and functional hydrogels, are increasingly significant. Unlike traditional methods like reverse osmosis desalination, which use secondary energy or phase change condensation with cold fluids, these materials leverage their physical and chemical properties (e.g., Laplace pressure gradients, polymer chain modifications, tunable intermolecular spaces, and open metal sites).

Here, we focus on the research output of passive technologies for atmospheric (gaseous) water harvesting in the last decade and provide comprehensive discussion on the state-of-the-art materials from the perspective of materials chemistry. According to the degree of water saturation, these materials are divided into two categories: (a) structured surface used for saturated atmospheric water collection and (b) MOFs, HICs and its derivatives, ionic liquids (ILs), and (c) functional hydrogels used for unsaturated vapour capture and water production. Future perspectives and potential optimization approaches are also presented which can further improve the water production performance so that it can meet energy sustainability and carbon neutral economy requirements.

2.2 Water harvesting from saturated air

Saturated water consists of tiny droplets dispersed in the air under a supersaturated state. **Figure 2.1** shows the psychrometric chart for gas-water mixtures and the saturated water collection mechanism. Unsaturated water collection occurs in two steps (**Figure 2.1A**): water vapor is first adsorbed on the surface of hydrophilic AWH material. A temperature drop to the dew point raises humidity to 100% (saturated state, point 1 to point 2), liquefying and storing water molecules in the AWH materials. Fog harvesting involves accumulating small water droplets into larger ones on cold surfaces. In the past decade, this has been observed in metal networks and spider webs, leading to the development of various network materials with different structures, shapes, angles, and mesh densities for saturated water harvesting [19-20]. Numerous systems using electricity to condense water have been developed and reviewed elsewhere, but this review will focus on spontaneous saturated water harvesting materials.

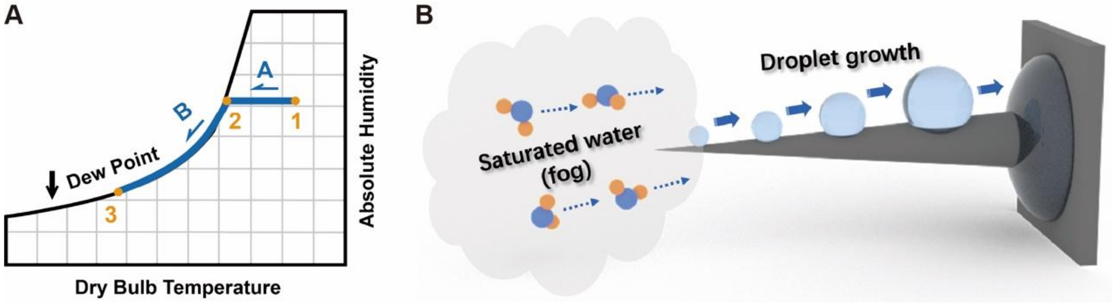

Figure 2.1 (A) Psychrometric chart for air-water system and water condensation mechanism. (B) Schematic illustration of dew water growth and transportation on biomimic conical spine.

Biomimetic materials for AWH applications have a long history, inspired by animals and plants in desert areas. Various functional materials, such as amphiphilic surfaces and artificial cactus spines, have been developed for fog water harvesting [21-23]. For example, Andrew et al. created a biomimetic surface inspired by the Stenocara beetle [24], which has an irregular textured shell with hydrophilic sites on its hydrophobic shell background[25-29]. Mimicking this, hydrophobic polystyrene (PS) and hydrophilic poly(4-vinylpyridine) (P4VP) were coated on a substrate to form a dual-layered coating (**Figure 2.2**). Under high-temperature annealing, isolated P4VP spheres formed on the PS layer, gathering small water droplets that grew and flowed to a freshwater container along the hydrophobic PS surface. A condensation rate of 3,400 mL m^{-2} h^{-1} was achieved at an air flow rate of 9.8 L min^{-1}, higher than pure PS or P4VP surfaces. Similarly, Zhang's group developed a hybrid surface with fluoro-alkyl silanes (FAS) modified with TiO_2 and SiO_2 nanoparticles (NPs). [30] UV irradiation made TiO_2 NPs hydrophilic, while SiO_2 NPs remained hydrophobic. This staggered arrangement enabled efficient water collection. Hydrophilic regions promoted droplet formation, while hydrophobic areas aided fusion and flow, achieving a maximum water harvesting capacity of 1,700 g m^{-2} h^{-1}. The efficiency was influenced by the humid air flow rate, surface area, NP density, and surface angle. Adjusting the droplet transfer process optimized water production. Other saturated water (fog) harvesting surfaces made of asymmetric fiber[31], polyacrylonitrile/poly(methyl methacrylate) (PAN/PMMA) nanocomposite fibers[32], and polypropyene (PP) surface embedded with polydopamine NPs[33] have also been reported.

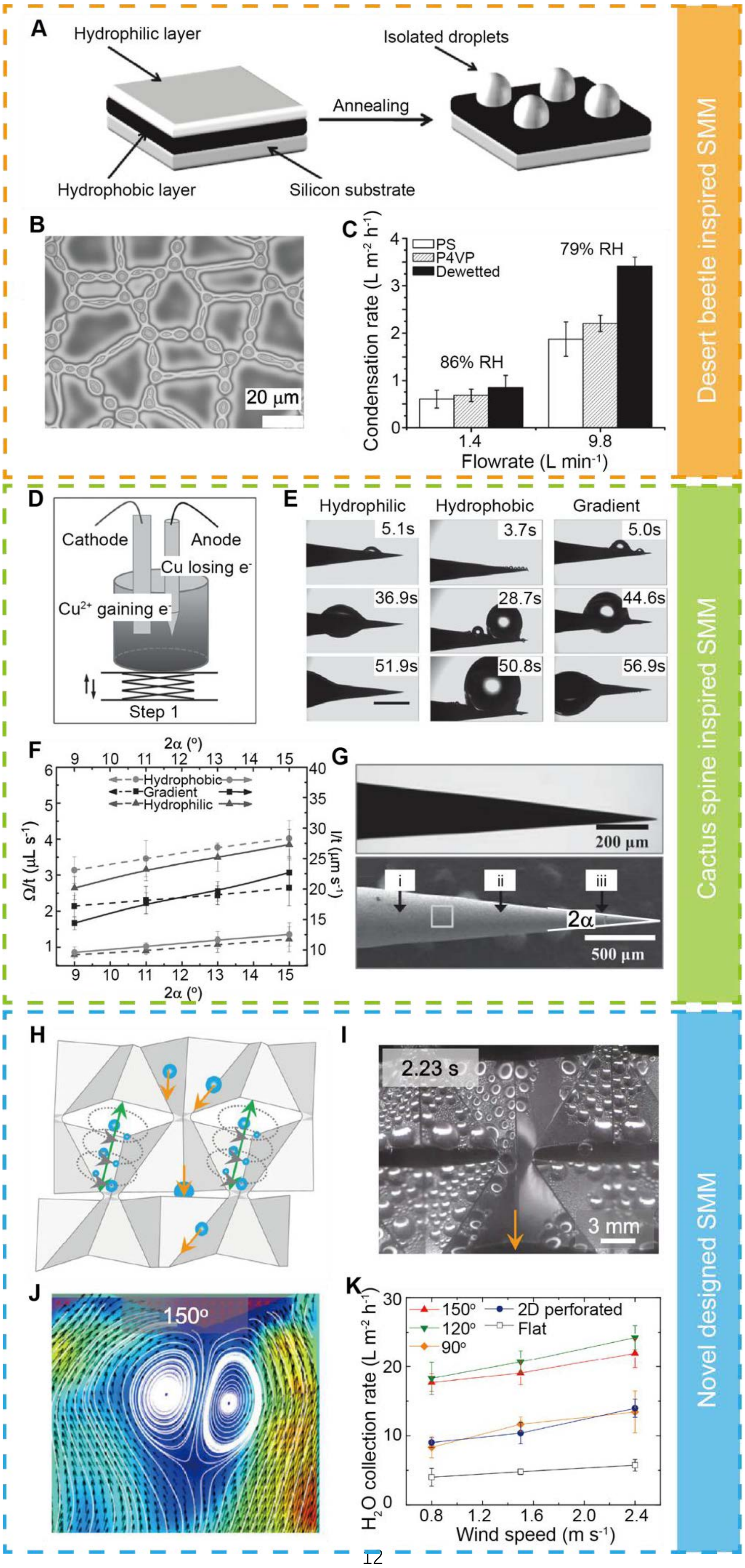
Desert beetle inspired SMM
A
Hydrophilic layer
Isolated droplets
Annealing
Hydrophobic layer
Silicon substrate
B
20 μm
C
Condensation rate (L m-2 h-1)
PS
P4VP
Dewetted
79% RH
86% RH
0
1
2
3
4
1.4
9.8
Flowrate (L min-1)
Cactus spine inspired SMM
D
Cathode
Anode
Cu losing e-
Cu2+ gaining e-
Step 1
E
Hydrophilic
Hydrophobic
Gradient
5.1s
3.7s
5.0s
36.9s
28.7s
44.6s
51.9s
50.8s
56.9s
F
2α (°)
9
10
11
12
13
14
15
Hydrophobic
Gradient
Hydrophilic
Ω/t (μL s-1)
l/t (μm s-1)
1
2
3
4
5
6
10
15
20
25
30
35
40
G
200 μm
i
ii
iii
2α
500 μm
Novel designed SMM
H
I
2.23 s
3 mm
J
150°
K
H2O collection rate (L m-2 h-1)
150°
120°
90°
2D perforated
Flat
0
10
20
30
0.8
1.2
1.6
2.0
2.4
Wind speed (m s-1)

Figure 2.2 (A) Illustration of the dual-layered saturated water harvesting membrane. The top layer (plate or isolated droplets) and the middle layer (black) are made of P4VP and hydrophobic PS, respectively. (B) Optical microscopy image of the dewetted P4VP solid droplets. The dark background is the hydrophobic PS layer. (C) Rate of fog condensation on pure hydrophilic P4VP surface, pure hydrophobic PS surface, and PS plate decorated with P4VP solid droplets at 1.4 L min^{-1} and 9.8 L min^{-1} of humid air flowrate. (E) Electrodeposition process in the CCW fabrication. (F) Simulation of the fog water harvesting process for pure hydrophilic, pure hydrophobic, and gradient modified CCWs within a 60 s period. (G) Saturated water harvesting rate (μL s^{-1}) and water droplet moving velocity (μm s^{-1}) for pure hydrophilic, pure hydrophobic, and gradient modified CCWs. (H) SEM images of a CCW that has a hydrophilicity gradient between its hydrophilic wider end and hydrophobic narrow end. (I) The structural design of karigami 3D surface using Al-coated PET sheet, and the schematic of the formation of addy currents. (J) Standard optic photo of the water droplets formation on the surface of PET sheet. (K) Mathematical modelling of addy current at the surface of karigami surface. (L) Saturated water harvesting rates changing with increased flowrate of moist air for the karigami surface with flat (180^{o}), 90^{o}, 120, and 150^{o} bending. (A) to (C) are adapted with permission from ref [24]. Copyright 2011 John Wiley & Sons. (D) to (G) are adapted with permission from ref [34]. Copyright 2013 John Wiley & Sons. (H) to (K) are adapted with permission under a Creative Commons CC BY License from ref [35] . Copyright 2021 Springer Nature.

Unlike 2D horizontal surfaces inspired by desert beetles, vertically designed 3D water harvesters efficiently condense and transfer gaseous water in oversaturated environments [36]. Cone-shaped cactus spines, made of cellulose, lignin, arabinan, and other polysaccharides, have high water affinity, aiding fog collection in deserts [37-39]. Mimicking this structure, Jiang's group developed a conical copper wire (CCW) with axial gradient wettability for saturated water harvesting [34] (**Figure 2.2D-G**). Fabricated by gradient electrochemical corrosion and surface modification, the hydrophobic narrow end (region F, **Figure 2.2G**) supports small droplet growth, while the hydrophilic wider end (region D, **Figure 2.2G**) promotes droplet movement due to contact angle differences. The CCW exhibited a higher water harvesting rate (2.5 μL s^{-1}) and faster droplet movement (22.5 μm s^{-1}) than hydrophobic and hydrophilic counterparts. Other similar systems have been also reported elsewhere [40-45].

In these research, it is easily found that the main bottleneck in harvesting saturated water is the contact pattern between humid air and the conical spine, specifically the aerodynamics and fluid mechanics near the material surface. Inspired by eddy currents, Yang et al. explored water harvesting surface morphology, creating a kirigami-like 3D surface that promoted eddy currents in moist air, accelerating fog harvesting, and achieving an ultra-high rate of 24.5 L m^{-1} h^{-1} at a humid air flow rate of 2.4 m s^{-1}. They used ultra-thin Al-coated PET sheets (127 μm thick) to create the desired kirigami-like 3D surface (**Figure 2.2H-K**). They evaluated the water harvesting rate with bending angles of 180°, 90°, 120°, and 150°, with humid air (0.8 - 2.4 m s^{-1}) flowing perpendicular to the surface. And mathematical modeling confirmed eddy current generation. This kirigami-like 3D surface achieved significantly higher fog collection efficiency than all previously published structured surfaces for saturated water harvesting [35].

Water droplets condense on hydrophilic surfaces and move on hydrophobic surfaces, making designs inspired by desert beetles and cactus spines mainstream for saturated atmospheric water harvesters, and **Table 2.1** provides representative studies of saturated AWH materials and their performance. However, water harvesting capacity and condensation rates vary due to differences in surface chemical structures and conical spine density. During droplet growth and transfer, avoiding water molecule accumulation in surface microstructures is crucial, as residual water impacts efficiency and transfer kinetics. Biomimetic conical spines are characterized by neat arrangement, consistent orientation, and uniform shape, but the high cost of manufacturing with small abrasives hinders commercial application. Thus, 3D printing biomimetic conical spines offers a potential solution. In 2020, Wang et al. used projection micro stereolithography 3D printing to create closely-arranged Janus spines (inspired by aloe vera), revealing the water droplet growth and transport mechanism [46]. This approach offers new prospects for next-generation air-saturated water harvesting materials.

Table 2.1 Representative research outcomes of saturated water harvesting materials.

Material	Preparation method	Character	Capacity / rate	Year	Ref.
PS, P4VP	• Spin-coating	• Staggered hydrophilic-phobic arrangement	0.17 L m^{-2} h^{-1}	2011	[24]
TiO_2, SiO_2 fluoro-alkyl silane	• UV-irradiated fabrication	• Hybrid super-wettable surface • Composite material	1.75 L m^{-2} h^{-1}	2018	[30]
PDMS, alginate	• Microfluidic controlled fabrication • 3D-printing	• Inspired by desert beetle • Asymmetric arrangement	39.24 L m^{-2} h^{-1}	2021	[31]
PAN, PMMA TiO_2, Al-NPs	• Electro-spinning	• Composite material • TiO_2 NPs embedded	6 L m^{-2} h^{-1}	2020	[32]
PDA, SU-8	• Negative photolithography	• Multi-layered design	0.97 L m^{-2} h^{-1}	2017	[33]
ZnO	• Vapor phase approach	• Manipulated branched nanowire array	12 μL h^{-1}	2014	[44]
PDMS, Co-NPs	• Magnet-assisted molding	• Magnetic responsible • Spine direction controllable	84 μL h^{-1}	2015	[40]
MPAM, MPs	• Magnet-assisted molding	• IR heating fabrication • Magnetic responsible	10.84 L m^{-2} h^{-1}	2013	[41]
Al, PET	• Electro-deposition	• Janus membrane with hydrophobic (inside) and hydrophilic (outside) surface	3.3 L h^{-1}	2018	[42]
PMHS, Al	• Spray-coating	• Arc, triangle, and rectangle shape array	4.5 L m^{-2} h^{-1}	2021	[43]

The field of saturated water harvesting materials faces several challenges. Structured surface materials for saturated water harvesting mainly follow two designs: hydrophilic functional patterns on hydrophobic surfaces for condensation and transport, and conical spines with gradient hydrophilicity (gradient Laplace pressure). While lab-scale experiments achieved an average water harvesting capacity of 3 g g^{-1}, industrial-scale production faces difficulties due to complex manufacturing processes involving control of direction, length, and hydrophilicity of the spines, and high costs. However, advancing 3D printing technology is expected to address these issues, producing cost-effective, stable water harvesting systems. Additionally, efficient water transport on the material surface (e.g., grooves connected to spines) is crucial for reducing residual water and improving collection efficiency.

2.3 Water harvesting from unsaturated air

The water harvesting materials aforementioned are able to capture supersaturated moisture droplets in the air (>100% R.H.). However, over-saturated water vapor is not always available due to difficulties associated with the temperature below dew point. Consequently, research has shifted towards unsaturated water harvesting, i.e., collecting water molecules from the ambient environment. This process is more complex than saturated water harvesting, requiring novel hydrophilic materials and different driving forces for effective water condensation and transfer. AWH can be passive or active. Hygroscopic materials absorb water from moist air, followed by electricity-driven condensation (active dewing). Alternatively, water can be passively collected by adsorption onto cold, hydrophilic surfaces (passive dewing). Active dewing devices utilizing wind power and various water adsorption beds have been proposed [47-48]. employing unique structures and/or external energy to enhance water harvesting. Here, we focus on materials for spontaneous unsaturated water harvesting, including MOFs, HICs and derivatives, ILs, and functional hydrogels. We explore their structure-property-performance relationships from a materials chemistry perspective. These materials contain strong polar ionic, coordination bonds, or functional groups to attract water molecules. Their cavities enable water molecules to adsorb, condense, and flow for storage. Captured water can be collected by evaporation-condensation or direct extraction due to hydrogel shrinkage or environmental deformation.

2.3.1 Metal-Organic Frameworks (MOFs)

Metal-organic frameworks (MOFs) are a sub-class of coordination materials consisting of metal ions/clusters and organic ligands (aka. metal cluster linkers) connected via coordination bonds[49]. Since first reported in 1997, MOFs have been widely applied in the fields of gas separation, hydrogen storage, drug delivery system, catalysis, and chemotherapy[50-54]. Due to their high affinity for the polar water molecules, porous MOF materials with diverse porous structures and enhanced water stability have exhibited great potential for wastewater treatment and heavy metal removal [55-58] (**Figure 2.3**).

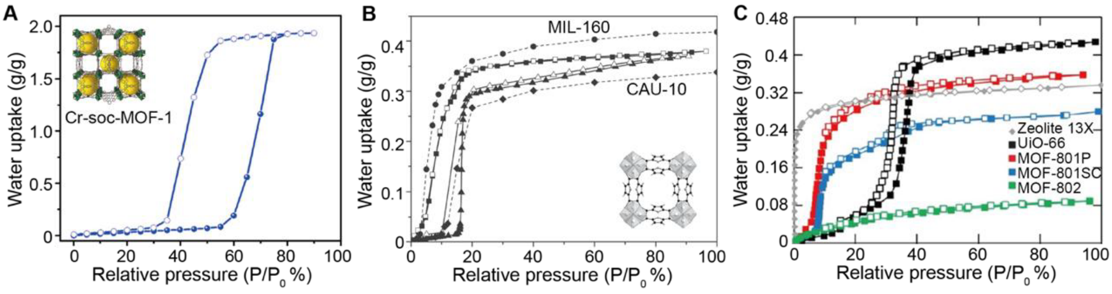

Figure 2.3 MOF water harvesters. (A) is adapted with permission from ref [59] . Copyright 2018 Elsevier. (B) is adapted with permission from ref [60] . Copyright 2015 John Wiley & Sons. (C) is adapted with permission from ref [61] . Copyright 2014 American Chemical Society.

MOF materials, typically powdered, can be used alone, as additives, or in special designs (e.g., shell-core composites) for the adsorption, transport, and storage of water molecules. Metal ions in MOFs connect with surrounding organic structures via strong polar coordination bonds. The molecular-sized cavities in MOFs store water molecules, which are adsorbed from the surface and drawn into the cavity by the polar units. Some water remains in the cavity during desorption, potentially reducing efficiency. However, MOFs can adsorb water in low-humidity environments, making them significant in AWH research.

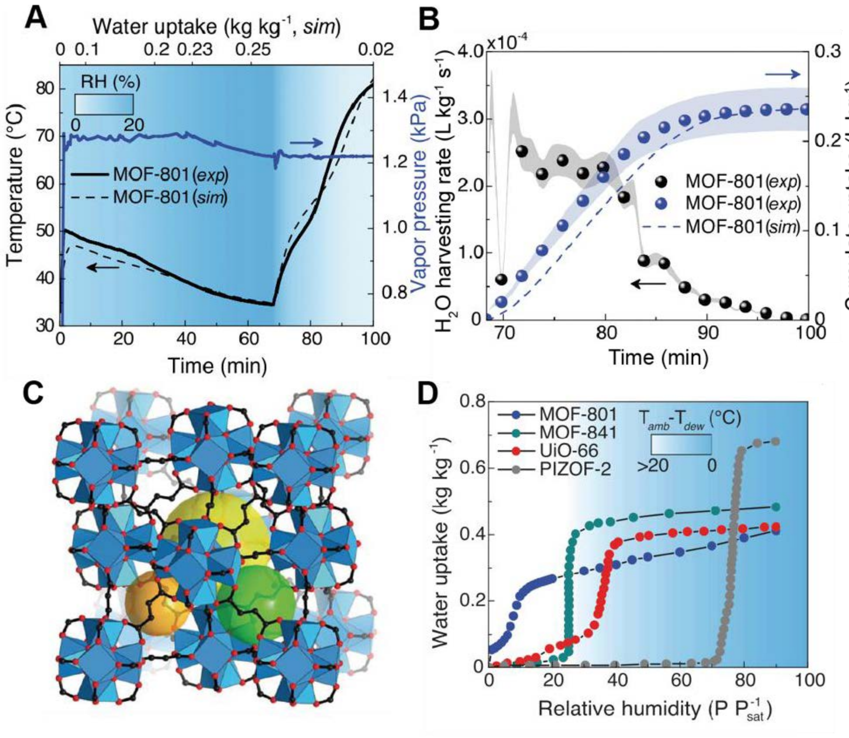

Figure 2.4 (A) Illustration of AWH system with forced thermoelectric (TE) cooler. (B) Water adsorption rate and cumulative value for MOF-801. (C) Schematic of the structure of MOF-801, with three porous areas (green, orange, and yellow spheres). Black and red dots refer to carbon and oxygen atoms, respectively. The Zr atom is located at the centre of each blue polyhedral. (D) AWH isotherms of MOF-801, MOF-841, UiO-66, and PIZOF-2. (A) to (D) are adapted with permission from ref [62] . Copyright 2017 The American Association for the Advancement of Science.

In 2017, Wang et al. developed MOF-801 $[Zr_6O_4(OH)_4(fumarate)_6]$ and proved its potential for harvesting unsaturated atmospheric water for the first time (**Figure 2.4A**) [62]. Thereafter, more than 20 types of MOF materials have been developed for AWH applications [63]. MOF-801 was selected as the favour material due to its well-recognized outstanding water adsorption behaviour and high chemical stability

(**Figure 2.4C**). The unsaturated water vapor can be introduced into the three cavities inside the secondary building units (**Figure 2.4D**) in a vacuum container to achieve water adsorption. MOF-801 has shown a water adsorption capacity of 0.4 g water per g of dry MOF (i.e., g g^{-1}) at 90% RH and 0.28 g g^{-1} under 20% RH (**Figure 2.4B**), which is the highest capacity compared with other MOF materials, such as MOF-841, UiO-66 and PIZOF-2. Under medium RH conditions (26-75%), MOF-841 has also shown the highest capacity, while PIZOF-2 has exhibited a greater water adsorption capacity at the high RH region (>80%). In a separate study, the water uptake of MOF-based materials is proved to be proportionally correlated with their pore size and Langmuir surface area[61]. The larger surface area provides more possibility for the water molecules to enter the MOF cavities, while the larger cavity size leads to less water transfer resistance, benefiting the water adsorption capacity. The cavity connection is controlled by the MOF topology, which is also related to the water adsorption kinetics. As an example, MOF-808 with 'spn' topology has seven small cavities surrounding a large cavity. Its water uptake has doubled compared to that of MOF-805/806 ('fcu' topology) with a larger average cavity size [61, 64]. Other water adsorption MOFs with different topologies have been reported elsewhere [65-70]. Although MOF-based materials with porous secondary building units have strong water affinity, the water adsorption capacity is still not sufficient for large scale water production. The exploration of MOF-based composite materials with greater water adsorption capacity and stimuli-response (i.e., thermal-induced) water release have greater potential for practical applications.

2.3.2 Hygroscopic Inorganic Compounds and Derivatives (HICs and derivatives)

The use of inorganic water sorbents for AWH dates back to 1998, when Gordeeva et al. used $CaCl_2$ and LiBr to collect water from moist air [71]. The absorbed water was then evaporated and condensed for collection. Over 20 years, this method remains a basic design strategy in modern AWH systems. Recently, Wang et al. developed manganese oxide (MnO_2) particles for AWH [72]. By adjusting the ratio of birnessite and cryptomelane, they synthesized MnO_2 particles with various surface morphologies and lattice structures. Birnessite-rich samples had greater water adsorption due to their large surface area and porous structure (**Figure 2.5A-C**). MnO_2-1 showed excellent photo-thermal conversion efficiency with a broad light absorption range and increased surface area, reducing reflection (**Figure 2.5A**). The key difference between birnessite and cryptomelane lies in the ratio and arrangement of manganese and oxygen atoms, affecting the lattice structure and surface properties. A challenge is preventing birnessite-based MnO_2 from reducing to cryptomelane.

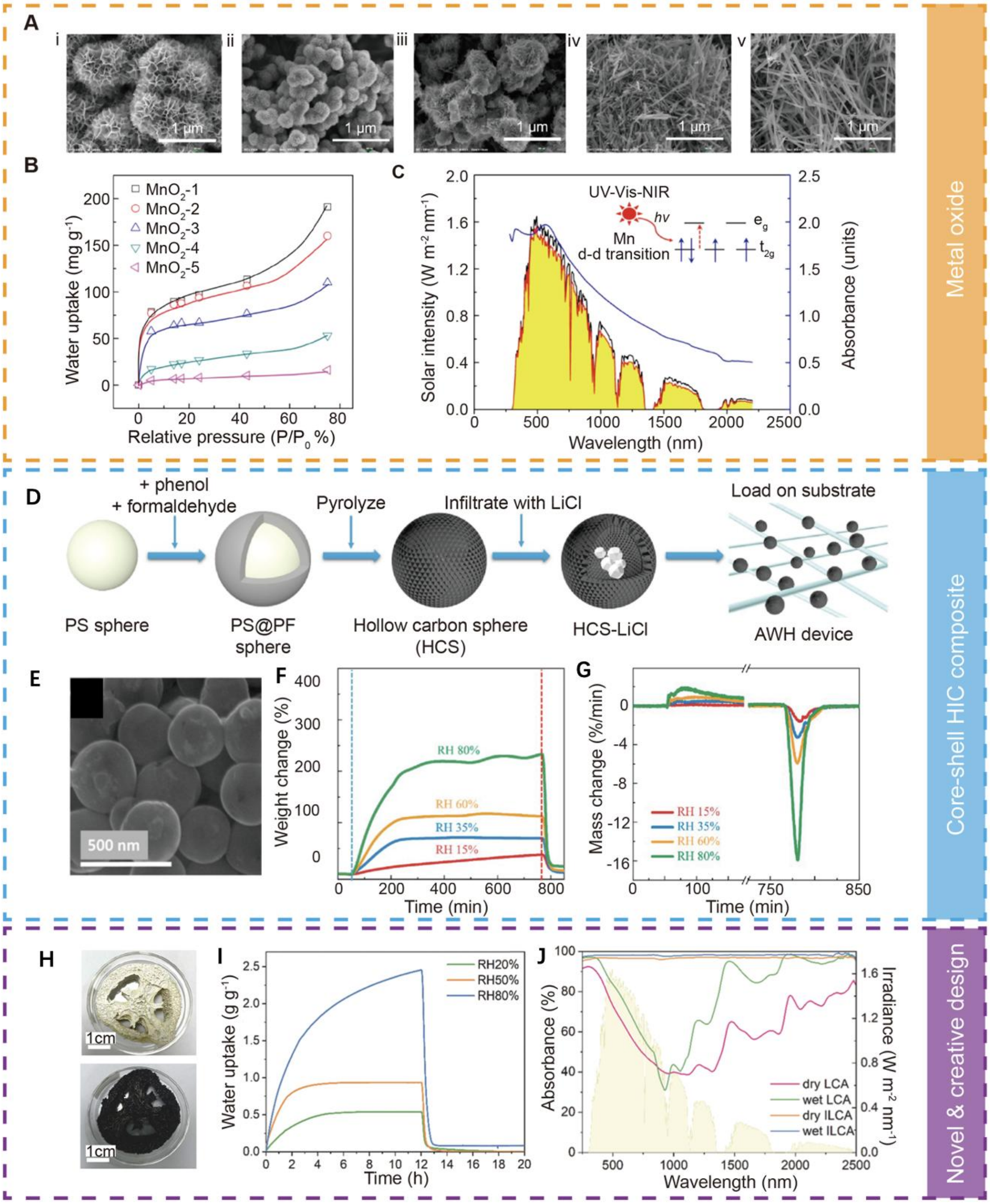

Figure 2.5 (A) SEM images of MnO_2 particles. Left to Right: pure birnessite to pure cryptomelane (MnO_2-1, MnO_2-2, MnO_2-3, MnO_2-4, MnO_2-5). (B) Atmospheric water adsorption isotherms for the five MnO_2 samples at 25 °C. (C) Equipment illustration of practical AWH system using MnO_2-1 sample. (D) Schematic of HCS-LiCl nanoscale sorbent. (E) SEM image of HCS-LiCl nanoparticle sorbent. (F) Adsorption and desorption behaviour of HCS-LiCl nanoparticle sorbent. (G) Weight change and temperature profile of HCS-LiCl nanoparticle

sorbent. (H) Morphology of loofah with SA matrix crosslinked inside the loofah structure (LCA) (top side) and Morphology of loofah with SA matrix crosslinked inside and SA+carbon covered outside of the loofah (ILCA) (bottom side). (I) Water uptake of SA and carbon modified loofah material in simultaneous thermal analyser (STA). (L) The absorbance of the modified loofah sponge with wet and dry state. (A) to (C) are adapted with permission from ref [72]. (D) to (G) are adapted with permission from ref [73]. (H) to (L) are adapted with permission from ref [74] .

To address the structural fragility of HICs, various designs have been used to embed HICs into encapsulation materials. Wang's group, for example, prepared nanoscale hollow carbon spheres (300 nm diameter) for encapsulating hygroscopic salt (**Figure 2.5D&G**), achieving a hygroscopic capacity of 2.3 g g^{-1} at 80% RH and 91.3% water desorption efficiency within 1 hour (**Figure 2.5F**) [73]. They also developed another AWH material using a sodium alginate matrix, $CaCl_2$, and modified loofah fiber support (**Figure 2.5H**), which absorbs solar irradiation from 300-2500 nm (**Figure 2.5J**) [74]. This material had a water adsorption capacity of 2.45 g g^{-1} at 80% RH and 0.85 g g^{-1} at 50% RH (**Figure 2.5I**). Similar studies are reported elsewhere [75-78].

HICs have shown excellent unsaturated water adsorption but suffer from low structural stability, resistance to ionization, and poor response to stimuli, limiting their applications. The two major challenges are instability of the crystal structure and limited response to environmental stimuli, reducing cycle performance and water release rate. Recent research has focused on HIC-embedded hybrid materials, such as HIC/MOF and HIC/ACF or SVG systems, to overcome these obstacles.

2.3.3 Ionic Liquids (ILs)

The idea of using ILs for AWH originated from their potential in gas adsorption. In 2002, Zhang et al. demonstrated ILs' efficiency in sulfur removal from flue gas, suggesting potential for water vapor adsorption [79-80]. In 2019, Zhu et al. reported an IL-based AWH application [81]. In this work, an IL pair (1-ethyl-3-methyl-imidazolium cation $[EMIM]^+$/acetate anion $[Ac]^-$) was selected as a strong water vapor adsorbent (**Figure 2.6A**). Polar water molecules connect with $[EMIM]^+/[Ac]^-$ through hydrogen bonds at the liquid surface, then move inward following the concentration gradient. The hydrogen bond energy decreases from 93.64 kJ mol^{-1} to 53.99 kJ mol^{-1} as water adsorption reaches its maximum of ca. 1.12 g g^{-1} at 80% RH. However, this IL pair only achieves 0.18 g g^{-1} and 0.1 g g^{-1} at 20% and 10% RH, respectively (**Figure 2.6B**). Another IL-based AWH composite material, reported by Chen's group [82], involves a composite IL $[C_2OHmim][Cl]$ and LiCl (in ethanol) mixed with CNT (photothermal material). The mixture is dispersed in cotton rods and oven-dried (**Figure 2.6C**). The resultant CNTs-CILs@cotton rod presented a wide UV-Vis-NIR absorption range (**Figure 2.6D**) and a high water adsorption capacity of 1.15 g g^{-1} at 25 ºC and 80% RH (**Figure 2.6E**). This composite material also achieves a maximum water evaporation rate of 2.0 kg m^{-2} h^{-1} and 70% water-release efficiency under 1.0 sunlight irradiation. Similar research results are available [83].

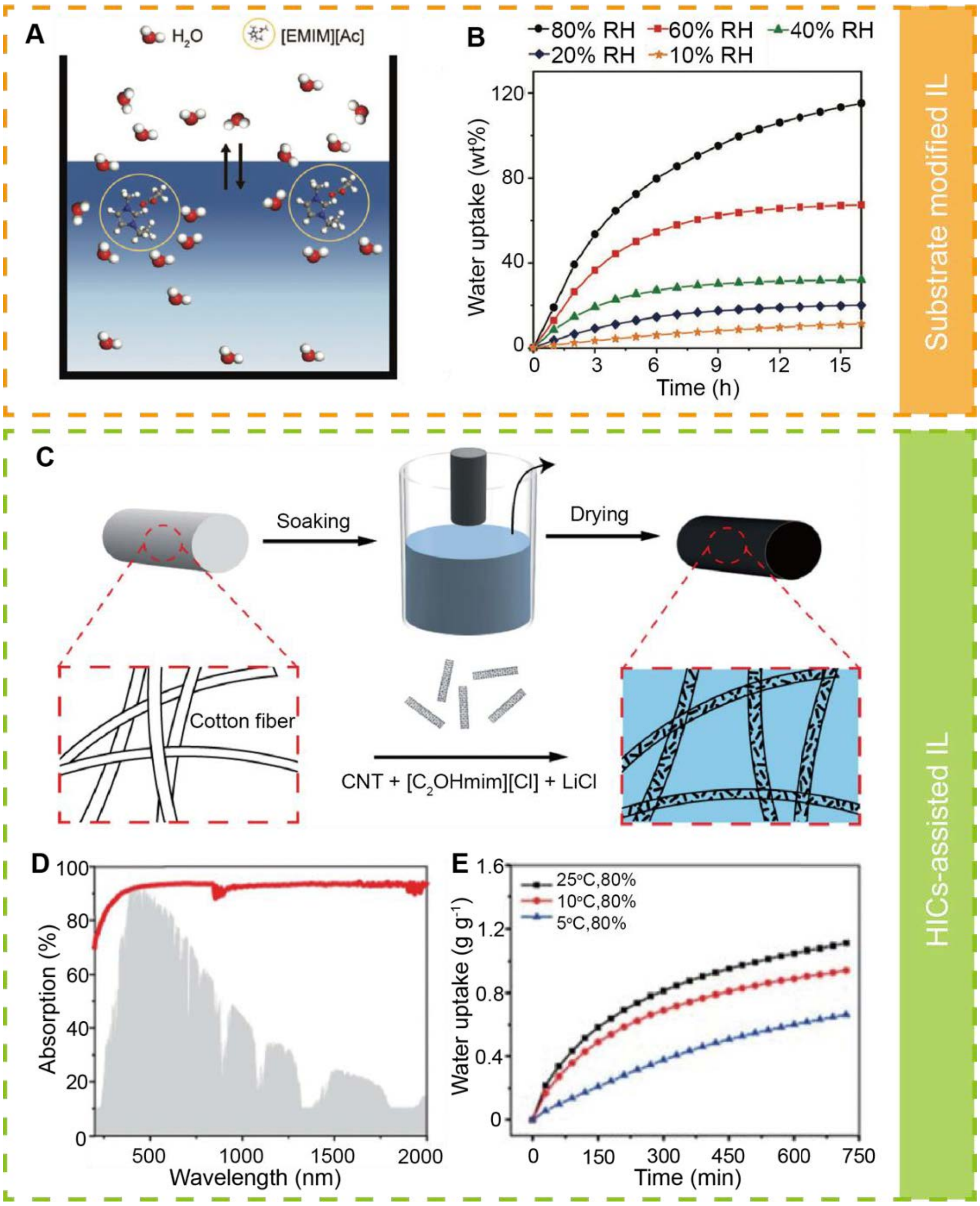

Figure 2.6 (A) Schematic of the water adsorption mechanism of [EMIM][Ac] ionic liquid. (B) Water adsorption capacity of [EMIM][Ac] ionic liquid at 10%, 20%, 40%, 60%, and 80% RH at 25 °C. (C) Schematic illustration of the fabrication procedure of the CNTs-CILs@cotton rod. (D) UV-Vis-NIR absorption spectrum of the CNTs-CILs@cotton rod. (E) The static water adsorption curves of CILs at different temperatures under 80% RH. (A) and (B) are adapted with permission from ref [81] . Copyright 2019 John Wiley & Sons. (C) to (E) are adapted with permission from ref [82] . Copyright 2021 The Royal Society of Chemistry.

Unfortunately, the strong affinity of IL materials for water vapor makes desorption of water molecules challenging. Additionally, transportation difficulties, higher weight compared to porous solid adsorbers, and high residual water content are bottlenecks for their practical application in AWH.

2.3.4 Functional Hydrogels

Hydrogel is a hydrophilic gel with a three-dimensional network structure that can expand and hold a large amount of water without damage. The network consists of polymer chains and crosslinking points with functional groups. Hydrogels are diverse and can be classified by crosslinking methods into physically and chemically crosslinked gels [84], by raw materials into natural and synthetic hydrogels [85], or by response to stimuli into traditional and stimuli-responsive hydrogels [86-89]. Hydrogels used in AWH are typically synthetic and stimuli-responsive, allowing for controlled water release. These hydrogels offer high design flexibility, strong water adsorption, and autonomous water release. The mechanism of water adsorption and transportation in AWH hydrogels is shown in **Figure 2.7**. Water vapor is adsorbed on the hydrogel surface, forming an adsorption layer as water molecules move vertically. They then flow towards the hydrogel 'walls' and transport through interconnected pores due to capillary forces and concentration gradients.

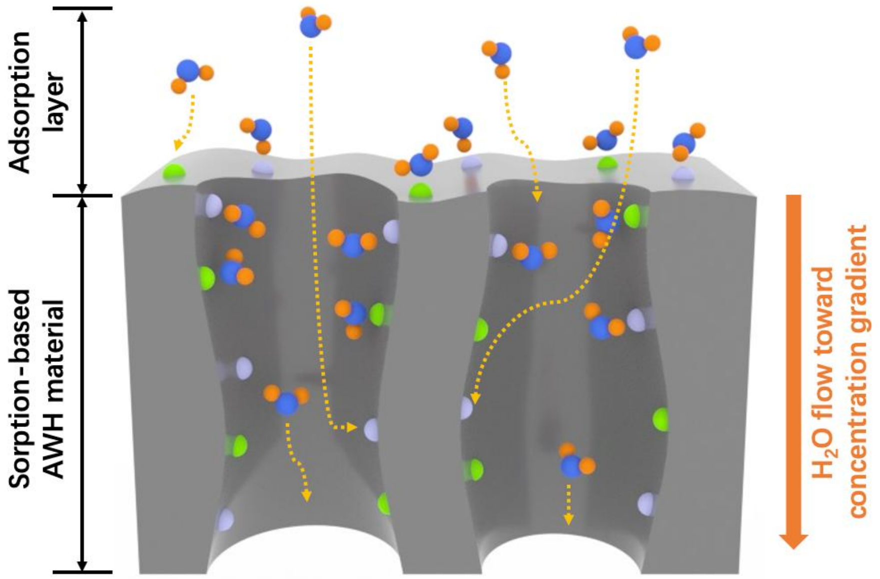

Figure 2.7 Schematic illustration of water adsorption mechanism of AWH hydrogel. (Green and purple dots: adsorption sites composed by hydrophilic functional groups)

A conventional composite hydrogel adsorbs water through the strong affinity between its functional groups and water molecules. Under sunlight, the embedded photothermal converters (fillers) raise the temperature, causing the adsorbed water to evaporate. This material can harvest liquid water only when paired with a passive condensing device (like an inclined glass plate connected to a water collection container above the hydrogel), as the evaporated vapor needs to condense first. Additional additives (e.g., HICs) can enhance the hydrogel's ability to attract and liquefy water.

Wang et al. constructed an AWH composite hydrogel with sodium alginate as a carrier, functionalized multiwalled carbon nanotubes (FCNTs) as a photothermal converter, and HICs ($CaCl_2$ and LiCl) to enhance adsorption capacity (**Figure 2.8A-D**) [90]. This hydrogel achieved a maximum water adsorption of 5.6 g g^{-1} at 90% RH using both $CaCl_2$ and LiCl, though with slightly reduced sunlight absorption due to lower FCNT density [91]. The hydrogel with both salts reached approximately 75 °C for water release, slightly lower than the $CaCl_2$-only hydrogel but higher than the LiCl-only version. Separately, Ni's group developed a semi-interpenetrating gel by adding poly-pyrrole-dopamine (P-Py-DA) to a poly(sodium methacrylate-co-acrylamide) (P(SMA-co-AM)) copolymer network. Replacing water with glycerine formed a hygroscopic photothermal organogel (POG) with a 0.6 g g^{-1} maximum moisture adsorption capacity [92]. The water molecules formed stronger hydrogen bonds with polymer chains, displacing glycerol and activating adsorption sites for further water adsorption. Hydrogels significantly improved AWH material stability compared to MOF-based powders. However, water release from these hydrogels relies on sunlight and high temperatures from embedded photothermal converters to evaporate adsorbed water, which is then condensed by a cooling system. Similar hydrogel designs using photothermal converters and HICs are reported elsewhere [93-98].

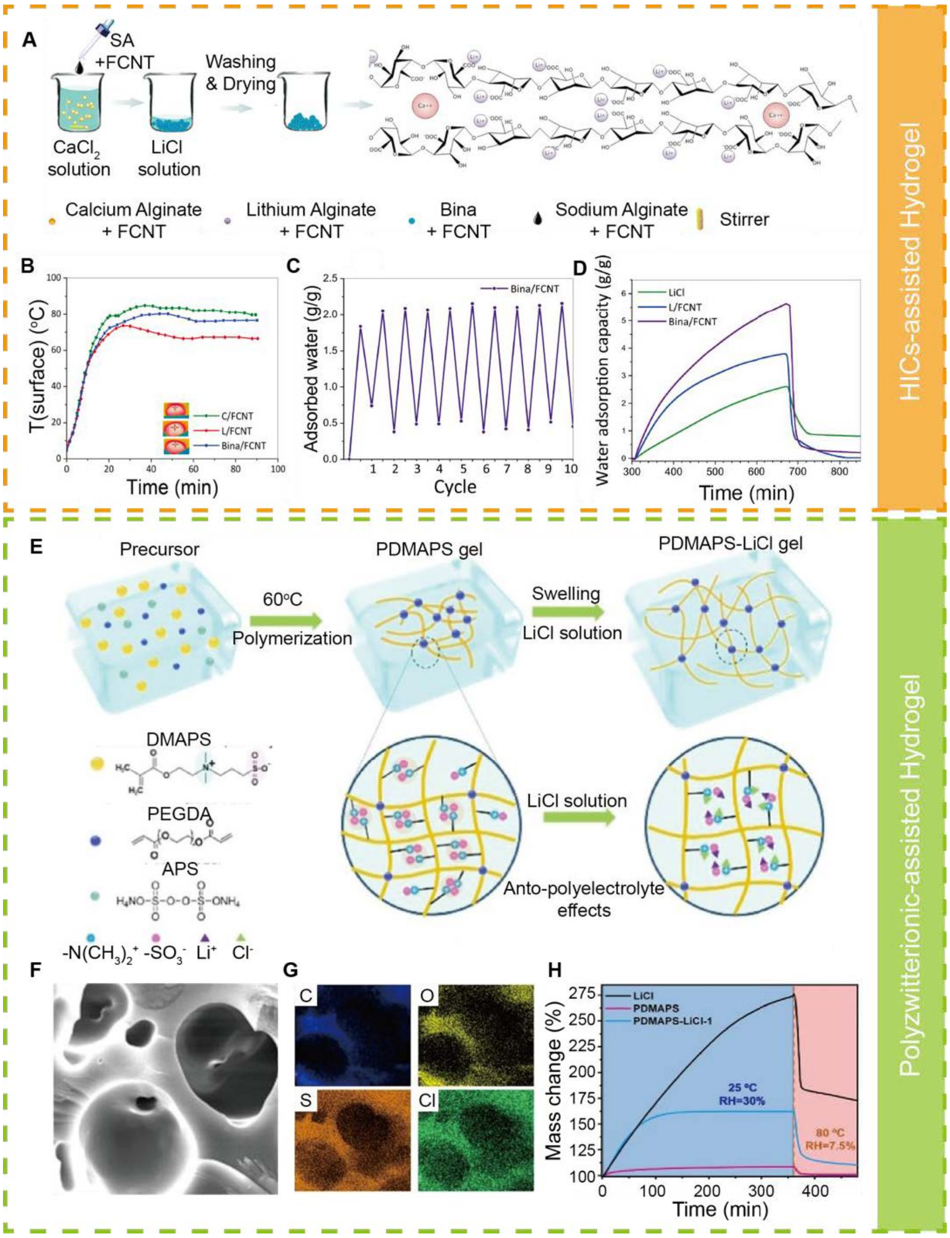

Figure 2.8 (A) Manufacture process of a Ca/Li-CNT hydrogel. (B) Water release temperature versus time for Ca-CNT, Li-CNT and Ca/Li-CNT hydrogels. (C) Water adsorption-release cycle test. (D) Plots of moisture adsorption capacity variations within 800 min for LiCl, Li-CNT hydrogel, and Ca/Li-CNT hydrogel. (E) Illustration of the PDMAPS-LiCl hydrogel and its water adsorption mechanism. (F-G) SEM image and EDS mapping of PDMAPS-LiCl-1 hydrogel, respectively. (H) Sorption–desorption curves of pure LiCl (black), bare PDMAPS hydrogel (pink), and PDMAPS/LiCl hybrid system (blue). (A) to (D) are adapted with

permission from ref [90] . Copyright 2020 American Chemical Society. (E) to (H) are adapted with permission from ref [99] . Copyright 2020 John Wiley & Sons.

More recently, Yu et al. prepared a polyzwitterionic (PDMAPS) hydrogel with immobilized hygroscopic salt (LiCl) via solvent replacement (**Figure 2.8E-H**)[99]. The inclusion of highly polar LiCl attracts and liquefies water molecules, forming a thin LiCl solution layer on the surface, aiding water transport and storage. Compared to bare PDMAPS hydrogel, the hybrid gel showed a swelling ratio three times larger and an unsaturated water harvesting capacity four times higher (0.62 g g^{-1}). This is the highest reported water adsorption capacity at low RH (30% RH). Additionally, approximately 80% of captured water (0.5 g g^{-1}) evaporated at 80 °C within 0.5 h. This study highlights the design flexibility of polymer networks, enabling HICs to enhance water adsorption in hydrogel-based AWH systems. Similar advancements using zwitterionic polymer networks as AWH sorbents are reported elsewhere [100].

Poly(*N*-isopropylacrylamide) (PNIPAM), a widely used stimuli-response hydrogel, has a lower critical solution temperature (LCST) of 37 °C, triggering a hydrophilic-hydrophobic transition[101-102] [103]. Below 37°C, the amide group (-CONH-) of NIPAM forms strong hydrogen bonds with water, making the hydrogel water-soluble. Above 37 °C, the weak bond energy (8-200 kJ mol^{-1}) compared to a common intramolecular bond (200-1000 kJ mol^{-1}), breaks easily [104-105]. The hydrophobic effect of the isopropyl group surpasses the hydrophilicity due to the weak hydrogen bond between the amide group and water. Thus, PNIPAM-based hydrogel adsorbs water below LCST and releases it above LCST, making it a key material for spontaneous water release in AWH applications.

Photothermal converters have been added to PNIPAM-based hydrogels to raise the gel temperature, inducing contraction and water release [87]. In 2019, Yu et al. showed that high water adsorption and self-contracting release are achievable by incorporating polypyrrole chloride (PPy-Cl) into PNIPAM hydrogel (**Figure 2.9**)[106]. PPy-Cl, with its pyrrole rings, absorbs broad visible light and converts it to heat. The NH+/Cl- charge pairs increase the hydrogel's water adsorption due to their strong polarity. The composite material's water adsorption under RH 30%, 60%, and 90% reaches 0.7 g g^{-1}, 3.3 g g^{-1}, and 6.6 g g^{-1}, respectively. In 30 min, 50% of the water is released quickly, followed by 60 min for the remaining 50%. Similarly, Yilmaz’s group created a PNIPAM-based composite hydrogel with Au nanoparticle-loaded MIL-101(Cr) as a photothermal converter, achieving 3.0 g g^{-1} water adsorption within 12 h at 90% RH. With Au nanoparticles, the hydrogel reached 60°C under 1.0 sun solar irradiation in 30 min, showing an average water release efficiency of 93% under sunlight. Hydrogels have raised the water adsorption capacity of AWH materials from under 1 g g^{-1} to 6-7 g g^{-1}, making them the best for AWH. The photothermal converter allows the hydrogel to quickly convert sunlight to heat but reduces water adsorption capacity. The water adsorption kinetics of AWH hydrogels are still being studied due to differences in functional groups and polymeric structures, which affects their performance under low humidity or short time periods. Similar water harvesting designs are reported elsewhere [107]. Detailed comparisons of AWH materials are in **Table 2.2**.

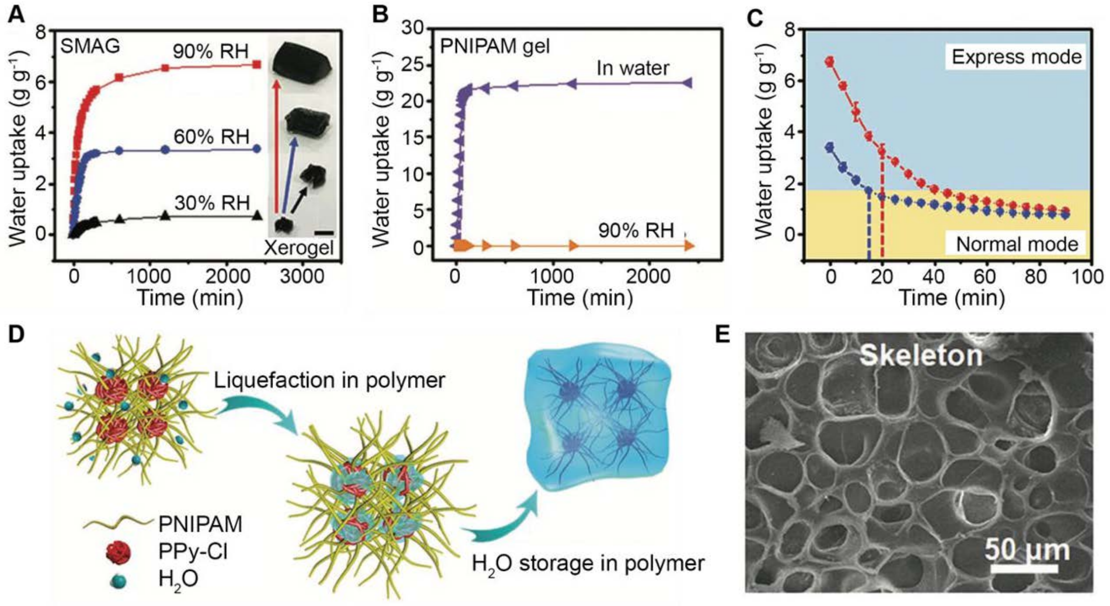

Figure 2.9 (A) Water uptake of PPy-Cl containing hydrogel versus time under different relative humidity (30 %, 60 %, 90 %). (B) Comparison of water uptake of PPy-Cl containing hydrogel versus time in a liquid water and moist environment. (C) Water release versus time of a PPy-Cl containing hydrogel. (D) Mechanism of water storage in a PPy-Cl containing hydrogel. (E) SEM image of a PPy-Cl containing hydrogel. (A) to (E) are adapted with permission from ref [106] . Copyright 2019 John Wiley & Sons.

Table 2.2 List of the sorption based unsaturated AWH materials and their adsorption and desorption performance

Type	Material	Ads. capacity[a] (g g^{-1})	Des. capacity[b] (g g^{-1})	Driving force	Year	Ref.
MOF	MIL-160	0.39 (90%RH)	-	Hydrogen bond MOF cavity	2015	[60]
	Ni$_2$Cl$_2$BTDD	1.1 (95%RH)	0.1 (30 ºC*)	Hydrogen bond MOF cavity	2019	[108]
	MOF-801	3.3 (40%RH)	2.3 (65 ºC)	Hydrogen bond MOF cavity	2018	[109]
	Cr-soc-MOF-1	1.9 (90%RH)	0.1 (25 ºC*)	Hydrogen bond MOF cavity	2018	[59]
	MOF-801	2.8 (20%RH)	0.02 (35 ºC*)	Hydrogen bond MOF cavity	2017	[62]
	Zr-fum-MOF	2.75 (90%RH)	-	Hydrogen bond MOF cavity	2011	[65]
	DUT-67	2.7 (90%RH)	1.1 (25 ºC*)	Hydrogen bond MOF cavity	2013	[66]
	Fe-Fc-HCPs, CaCl$_2$	4.54 (80%RH)	4.3 (55-63 ºC)	Electromagnetic attraction Hydrogen bond MOF cavity	2021	[110]
	HCS, LiCl	3.5 (80%RH)	2.5 (73 ºC)	Electromagnetic attraction	2020	[73]
	MIL-100(Fe), silica gel	0.7 (90%RH)	0.53 (-)	Hydrogen bond MOF cavity	2021	[111]
	UiO-66, T$_3$C$_2$, SA	0.7 (80%RH)	0.17	Hydrogen bond	2021	[112]

			(70 °C)	MOF cavity		
	MIL-101(Cr), SA	1.3 (90%RH)	0.6 (95 °C)	Hydrogen bond MOF cavity	2021	[113]
HICs & diravatives	MnO_2	1.8 (80%RH)	0.26 (49 °C)	Electromagnetic attraction Conc. gradient	2020	[72]
	$CaCl_2$, GO	5.4 (98%RH)	3.89 (60 °C)	Electromagnetic attraction Conc. gradient	2019	[114]
	LiCl, ACFF	3.6 (90%RH)	2.1 (80 °C)	Electromagnetic attraction Conc. gradient	2021	[115]
IL*	[EMIM][Ac]	1.2	0.1 (70-90 °C)	Electromagnetic attraction Conc. gradient	2019	[81]
	SiO_2, TFSI, $Si\text{-}P_8$	0.25	-	Electromagnetic attraction Conc. gradient	2019	[116]
Function customized hydrogel	NIPAM, CNT, $CaCl_2$	1.75 (80%RH)	1.51 (75 °C)	Conc. gradient Electromagnetic attraction Photothermal	2018	[97]
	Zn Acetate, ethanolamine	3.7 (90%RH)	3.45 (55 °C)	Conc. gradient Photothermal	2019	[117]
	NIPAM, MIL-101Cr	3.5 (90%RH)	3.2 (61 °C)	Conc. gradient MOF cavity Photothermal	2020	[118]
	NIPAM, PPy-Cl	6.2 (90%RH)	5.9 (63 °C)	Conc. gradient Photothermal	2019	[106]
	Alginate, $CaCl_2$, LiCl	5.6 (70%RH)	5.3 (72-75 °C)	Electromagnetic attraction Conc. gradient External energy	2020	[91]

	Alginate, $CaCl_2$	0.8 (25%RH)	0.72 (100 °C)	Electromagnetic attraction Conc. gradient External energy	2018	[93]
	B5AMA	0.51(-)	0.44 (37 °C)	Conc. gradient External energy	2018	[95]
	AEtMA, Acetate	1 (85%RH)	0.9 (70 °C)	Conc. gradient Photothermal	2021	[96]
	AAm, PPy, dopamine	1.54 (90%RH)	1.33 (58 °C)	Conc. gradient Photothermal	2020	[92]
	PDMAP, LiCl	0.6 (30%RH)	0.5 (80 °C)	Conc. gradient Zwitterionic attraction	2022	[99]

[a] The reported relevant humidity is attached in brackets. [b] The desorption temperature is attached in brackets.

: The value of desorption temperature with "" mark is obtained from adsorption-desorption isotherm, it is the experimental condition, and may not the temperature that practical water releasing is triggered.

Both saturated water collection and unsaturated AWH are still in the exploratory phase, particularly regarding material costs and the design and scaling of corresponding AWH devices. Conducting cost analysis will be crucial for advancing future research on AWH materials. Additionally, most AWH materials are currently paired with small-scale devices, typically with an average volume of approximately 8–20 liters. Scaling up production is a critical step toward achieving the eventual commercialization of AWH technologies.

Hydrogel-based AWH materials are highly promising due to their customizable functions and varied additives for efficient water harvesting. These materials offer an excellent balance between physical strength and AWH properties, yet there is room for improvement. No sorption-based AWH material has achieved an adsorption capacity of 1 g g^{-1} at <30% RH, which is the main development bottleneck. Additionally, at low humidity, storing liquefied water is challenging because of the dynamic balance between the liquefaction rate of water molecules on the material's surface and the evaporation rate of liquid water.

2.4 Conclusions and perspectives

Water production using synthetic AWH materials (e.g., structured surfaces, HICs, MOFs, and hydrogels) offers an alternative to conventional methods for addressing freshwater shortages due to their small size, high water harvesting capacity, energy independence, and easy installation. Despite existing challenges, Google Earth Engine simulation data suggests that optimizing equipment design and adsorption materials could feasibly provide the global population with 5 L of drinking water daily using AWH materials within thermodynamic limits [119]. Future research should explore combining different AWH materials and utilizing diverse diffusion mechanisms to enhance water adsorption and desorption efficiencies.

Hydrogel-based AWH materials are promising technologies for capturing water from the air, especially in arid regions. However, they face a number of key challenges that must be addressed to improve their efficiency, scalability and utility: First, in extremely arid environments with minimal atmospheric moisture content, hydrogels are significantly less effective. Secondly, AWH hydrogels typically necessitate energy input to release the adsorbed water, making the process energy-intensive and less environmentally sustainable. Thirdly, AWH hydrogels, exposed to air during water capture, foster bacterial growth and accumulate dust, necessitating well-designed antibacterial features and filtration systems. Fourthly, scaling up the production of hydrogel-based materials to meet the needs of large-scale water harvesting systems can be a challenging and costly endeavor. Lastly, comprehensive cost analysis is also required for AWH hydrogel synthesis, device manufacturing, and installation.

Chapter 3 Comprehensive Study on Structure-Property Relationships of Hydrogel AWH Materials.

Related publication:

Feng, A., Shi, Y., Onggowarsito, C., Zhang, X. S., Mao, S., Johir, M. A., ... & Nghiem, L. D. (2024). Structure-Property Relationships of Hydrogel-based Atmospheric Water Harvesting Systems. *ChemSusChem*, e202301905.

This chapter explores the relationship between structural characteristics and performance in hydrogel-based systems for atmospheric water harvesting (AWH). It emphasizes the significance of factors such as polymer composition, cross-linking density, and porosity in optimizing water adsorption and release. This study effectively highlights material innovations and their potential applications, while also identifying the practical challenges associated with large-scale implementation and environmental sustainability. This study establishes a strong foundation for future research aimed at addressing these issues and contributing to solutions for the global water scarcity problem.

3.1 Introduction

Although 70% of the earth's surface is covered by water, humans are currently facing an unprecedented water crisis since 21 century[120-123]. Only about 1.3% of the water covering the earth's surface is surface freshwater, of which 0.2% is stored in the air, about 2 × 10^{10} cubic meters[124-125]. This water in the air is ubiquitous in the form of saturated water (fog) and unsaturated water (water vapor), but is difficult to collect [126]. Capturing water from moist air is known as AWH [63, 127-128]. With the advantages of high ambient humidity and no need for liquefaction, fresh water can be obtained from metal spike arrays or large hydrophobic woven meshes during cold nights [129-130]. However, in most areas it is difficult to saturate the relative air humidity [131]. On the other hand, liquefaction and collection of unsaturated water vapor from air is even more difficult because liquefaction of water vapor and storage of fresh water are two independent processes that are difficult to reconcile when selecting and designing AWH materials [132-134].

In recent years, crystalline porous materials such as metal-organic frameworks (MOFs)[62, 109-110, 135] and covalent organic frameworks (COFs)[136-139] have been widely reported for AWH applications. These materials have well-defined chemical and crystalline structures, so it is easy to study their structure-property relationships. However, powdered MOFs and COFs material do not have macroscopically stabilized shapes and need to be ‘flattened’ on the substrate to increase the contact area with air. Compared to other AWH materials, polymeric hydrogels and/or their composites are widely used for not only freshwater production, but also sensing and direct air electrolysis for hydrogen production, due to their ease of preparation, low cost, and excellent compatibility [140-144]. There is a wide variety of hydrophilic monomer and/or polymer raw materials that have been used to prepare AWH materials, including monomers such as isopropylacrylamide (NAPAM), acrylamide (AM), and

2-(acryloyloxyethyl) trimethylammonium chloride (AEtMA), as well as polymer precursors such as poly(vinyl alcohol) (PVA), chitosan, and others[1, 3, 90, 145-146]. In addition, hygroscopic salts (e.g. calcium chloride, lithium chloride) and photothermal materials (e.g. graphene oxide, carbon nanotubes) have been incorporated into hydrogel to boost the water productivity[147-148]. However, the relationship between the chemical structure of the raw materials and the water sorption/desorption properties of the resulting hydrogels has been overlooked, resulting in a lack of fair comparisons between state-of-the-art AWH systems to guide researchers in rationally designing AWH hydrogel materials, which may reduce the efficiency of the research and increase the experimental cost[98, 149-151].

In this study, we prepared a series of hydrogel AWH materials using various monomer raw materials and investigated the relationship between chemical structure and physiochemical properties of the resulting hydrogels, such as hydrogel swelling ratio, hydrogel pore size, vapor adsorption kinetics and electrostatic potential etc. We found that the AWH hydrogel prepared by cross-linking ionic monomers (e.g. AEtMA, APtMA, and AMPS) exhibited high swelling ratio, dense pore structure, fast vapor adsorption and hence better AWH performance. Furthermore, we incorporated three photothermal materials (PTMs) into the PAMPS hydrogel, evaluated their water adsorption capacity and desorption efficiency and revealed the importance of the photothermal conversion performance of PTMs in AWH hydrogels. We thus expect that this study will provide guidance for the design and fabrication of high-performance AWH hydrogels in the future.

3.2 Experimental section

3.2.1 Material and chemical synthesis procedure

All chemicals were of purchased from Merck (Sigma-Aldrich). [2-(Acryloyloxy)ethyl]trimethylammonium chloride solution (AEtMA, 80 wt% in H_2O), 2-acrylamido-2-methyl-1-propanesulfonic acid (AMPS, 99%), acrylamide (AM >99%), N-isopropylacrylamide (NIPAM, 97%), 2-hydroxyethyl acrylate (HEA, 96%), (3-acrylamidopropyl)trimethylammonium chloride solution (APtMA, 75 wt% in H_2O), diacetone acrylamide (DAA, 99%), N,N′-methylenebis(acrylamide) (BIS, 99%), N,N,N′,N′-tetramethylethylenediamine (TEMED, 99%), ammonium persulfate (APS, 98%), and L-ascorbic acid (reagent grade) were used as received without further purification, unless otherwise stated. Deionized water (DI water) was obtained by Milli-Q water purification system (18.2MW.cm @25°C).

For a typical synthesis of the PAMPS hydrogel, 0.4 g AMPS (monomer, 1.93 mmol), 0.033 g BIS (crosslinker, 0.21 mmol), and 0.01 g L-ascorbic acid (catalyst) were mixed and dissolved in 1.9 mL DI water under sonication (solution A, [M]:[XL] = 9). 0.016 g APS (initiator) was dissolved in 0.1 mL DI water under sonication (solution B). To start the gelation, solution B was added into solution A to induce polymerization. The polymerization of hydrogel was carried out for 2.5 h. The as-prepared hydrogel was soaked in DI water for 1 h before dried 1.5 h under simulated sunlight irradiation to remove unreacted residue, then freeze-dried for 12 h before vapor adsorption tests.

For a typical synthesis of the PAMPS/CNT hydrogel composite, 0.4 g AMPS (monomer, 1.93 mmol), 0.033 g BIS (crosslinker, 0.21 mmol), 0.01 g CNT (photothermal material, PTM), and 0.01 g L-ascorbic acid (catalyst) were mixed and dissolved in 1.9 mL DI water under sonication (solution A). 0.016 g APS (initiator) was dissolved in 0.1 mL DI water under sonication (solution B). To start the gelation, solution B was added into solution A to induce polymerization. The polymerization of hydrogel was carried out for 2.5 h at room temperature. The as-prepared hydrogel was soaked in DI water for 1 hours before dried 1.5 h under simulated sunlight irradiation to remove unreacted residue, then freeze-dried for 12 h before vapor adsorption tests.

For a typical synthesis of the poly(AMPS-co-AEtMA) hybrid gel, 0.2 g AMPS (monomer, 0.965 mmol), 0.234 mL AEtMA solution (0.965 mmol), 0.033 g BIS (crosslinker), 0.01 g CNT (photothermal material, PTM), and 0.01 g L-Ascorbic acid (catalyst) were mixed and dissolved in 1.7 mL DI water under sonication (solution A). Then, 0.016 g APS (initiator) was dissolved in 0.1 mL DI water under sonication (solution B). To start the gelation, solution B was added into solution A to induce polymerization. The polymerization of hydrogel was carried out for 3 h. The as-prepared hydrogel was soaked in DI water for 1 hours before dried 1.5 h under simulated sunlight irradiation to remove unreacted residue, then freeze-dried for 12 h before vapor adsorption tests.

3.2.2 Characterizations

UV-VIS-NIR spectra of these AWH hydrogels were recorded on a SHIMADZU

UV-1700 UV-Visible spectrophotometer.

Fourier-transform infrared spectroscopy (FT-IR) spectra was obtained using a SHIMADZU MIRacle 10 single reflection ATR accessory.

Scanning electron microscope (SEM) images of hydrogels were obtained by Zeiss EVO LS15 SEM system.

Infrared thermometer images of hydrogels under sunlight irradiation were captured using FLUKE PTi120 thermal imager.

Inductivity coupled plasma mass spectrometry (ICP-MS) was used to analyse for ions concentration comparison of condensed water from AWH hydrogels. An Agilent Technologies 7900 ICP-MS system with SPS-4 Autosampler was used in this study.

Sunlight simulation light source was purchased from Beijing NBeT HSX-F300 xenon light source.

3.2.3 Moisture adsorption experiments

The moisture adsorption tests were conducted under static moist environment at fixed relative humidity with temperature monitoring (**Figure 3.1**). Before moisture adsorption experiment, a 1,000 mL beaker was filled with 80% volume of DI water, and a plastic thick bubble foam was cut as a plate before floating on the water surface inside the beaker for hygrometer support. The top of the beaker was 100% covered via parafilm, in order to prevent any water vapor leakage and relative humidity monitoring error. At fixed temperature, the relative humidity inside the 20% volume of beaker was adjusted via the ratio between the horizontal intersection water surface area and the area of the plastic thick bubble foam, which is monitored via the floating hygrometer. The moisture adsorption experiment was carried out for 12 h, with the mass of hydrogel recorded every 1 h.

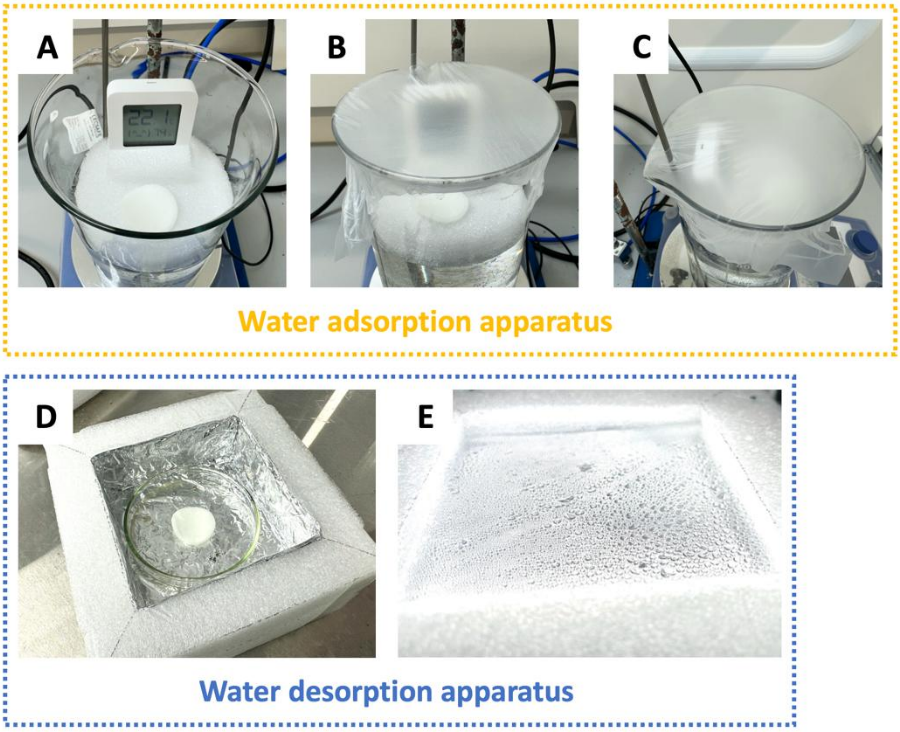

Figure 3.1 (A) Experiment apparatus (inside clear view) for in-door water adsorption experiment. (B) Experiment apparatus (actual experiential view) for in-door water adsorption experiment. (C) Experiment apparatus (parafilm fully covered view) for in-door water adsorption experiment. (D) Experiment apparatus (actual experiential view) for out-door practical water adsorption test. (E) Experiment apparatus (actual experiential view, under sunlight irradiation) for out-door practical water adsorption test.

3.2.4 Sunlight-assisted autonomous water release

The in-door sunlight-assistant evaporation was conducted using a XE300WUV Xenon light source (Beijing NBeT Technology Ltd) to simulate sunlight. The irradiation intensity was stabilized at 1,000 W m^{-2} (1.0 sun equivalent). The mass of hydrogel was monitored using an analytical balance with internal calibration (OHAUS Pioneer analytical balance) every 30 min. The surface temperature of the hydrogel was determined by IR camera (FLUKE PTi120 thermal imager).

3.2.5 Durability test

The durability of the hydrogel material was determined at 60% R.H. for 10 cycles (for each cycle, we performed water adsorption for 8 h, followed by 4 h indoor sunlight irradiation). At the end of each cycle, the hydrogel was further irradiated for 1 h to remove any potential water residue.

3.3 Results and discussion

3.3.1 Hydrogel structure and morphology

Current reports on AWH hydrogels usually overlook the effect of the structure-property-application relationships. Moreover, it is difficult to make an objective and fair comparison of the reported AWH performance since different test devices and/or methods are used in different laboratories. This thus leaves a knowledge gap in the field, hindering the development of high-performance AWH materials for practical applications. In this study, we prepared a series of AWH hydrogels by cross-linking different hydrophilic monomers, including NIPAM, AEtMA, APtMA, AM, AMPS, HEA and PDAA (**Scheme 3.1**). N,N′-methylene bis(acrylamide) (BIS) and ammonium persulfate (APS) were used as a crosslinker and radical initiator, respectively. We then synthesized the hydrogels via free radical polymerization of monomers and cross-linker. The hydrogel products were washed with DI water and freeze-dried for characterization as well as adsorption/desorption tests. This strategy ensures that the backbone structure of polymer chain is consistent/similar in all hydrogels, with the pendant moieties differing, thus minimizing the effect of the backbone and allowing for a more targeted study of the influence of different hydrophilic groups on the hydrogel AWH properties.

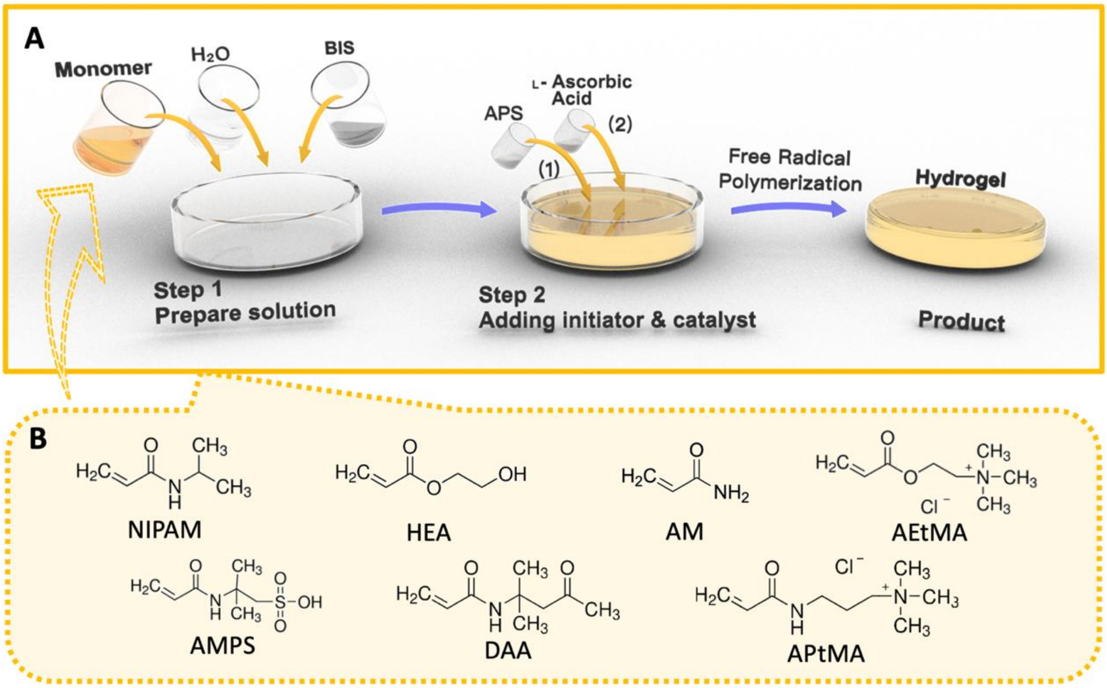

Scheme 3.1 Illustration of the synthesis of AWH hydrogels. (A) Step-by-step procedure for hydrogel synthesis. (B) Chemical structures of different monomers.

After freeze-drying, we characterized the resulting AWH hydrogels by FTIR spectrometer to confirm their characteristic chemical structures. As shown in **Figure 3.2A**, the amide groups (C(=O)-NH) of PNIPAM, PDAA, PAPtMA, and PAMPS chains were confirmed at 3,270 cm^{-1} (N-H stretch) and 1,650 cm^{-1} (C=O stretch), respectively. We also observed the characteristic peaks at 930 cm^{-1}, 1,490 cm^{-1}, and 2,930 cm^{-1}, which can be attributed to the N^{+}-C and C-H stretching vibrations of the quaternary ammonium groups of PAEtMA, respectively. The strong peaks at 1,250 cm^{-1} and 1,725 cm^{-1} can be assigned to the ester groups (C(=O)-O) of PAEtMA and PHEA. The dried hydrogels have a diameter of 30 mm and a thickness of 3.5 mm, with an aspect ratio of 8.6 (**Figure 3.2B**).

A high porosity surface increases the air-solid contact area and facilitates the water. adsorption at the interior interface of the hydrogel. We characterized the microporous structure of the hydrogels by scanning electron microscopy (SEM). We found that PAPtMA-, PAMPS-, PAEtMA-, PNIPAM-, PAM-, and PDAA-based hydrogels exhibit porous structures with relatively uniform pore sizes within each individual sample. Among these porous samples, the pore sizes follow the order from largest to smallest: PAEtMA > PAMPS > PDAA > PAM > PNIPAM > PAPtMA. (**Figure 3.2C i-v&vii**). In contrast, the SEM images of PHEA hydrogels reveal a closed-pore structure, differing significantly from the open porous structures observed in the other hydrogels (**Figure 3.2C vi**).

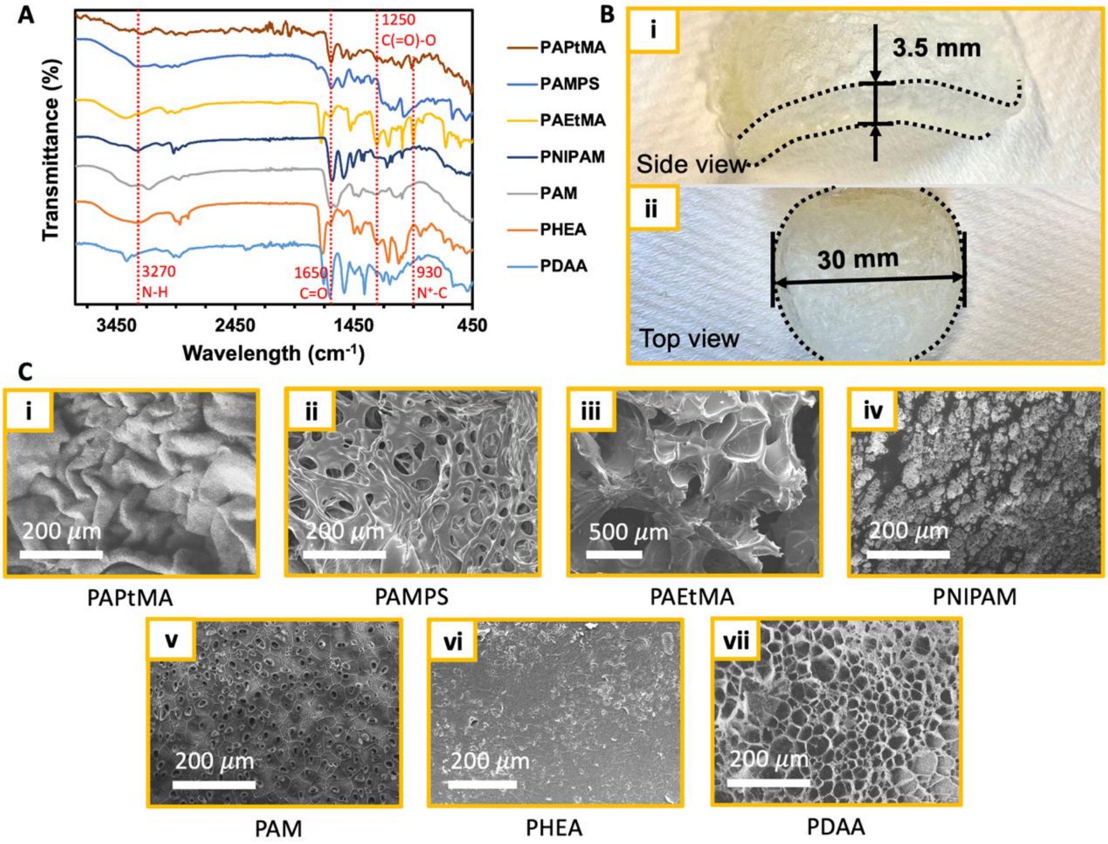

Figure 3.2 (A) FT-IR spectra pf PAMPS, PHEA, PAM, PAEtMA, PNIPAM, PDAA, PDMA, and PAPtMA hydrogels. (B) Optic image of PAMPS hydrogel for size and aspect ratio illustration. (C) SEM images of (i) PAPtMA, (ii) PAMPS, (iii) PAEtMA, (iv) PNIPAM, (v) PAM, (vi) PHEA, and (vii) PDAA hydrogel surface.

3.3.2 Electrostatic potential simulation

In this study, Avogadro software was used to build molecular electrostatic potential maps of the repeating units of hydrogels. The Merck Molecular Force Field (MMFF94) was used to simply simulate the electrostatic potentials using the steepest descent method. Water molecules are then introduced to random locations in the molecular model, and the total energy differences (ΔE) before and after the addition of water molecules were calculated (**Figure 3.3**). The energy difference is negative, which means that energy is released during the formation of hydrogen bonds between the polymer chains and the water molecules, and the enthalpy of the system decreases. That is, under conditions of random distribution of water molecules, the difference in the total energy of the system can be correlated with the driving force of water molecules on the polymer chains. As shown in **Table 3.1**, the PAPtMA hydrogel has the highest absolute value |ΔE|, while PHEA and PDAA hydrogels have lower absolute values, which suggests that these two hydrogels have relatively low driven force when adsorbing water molecules.

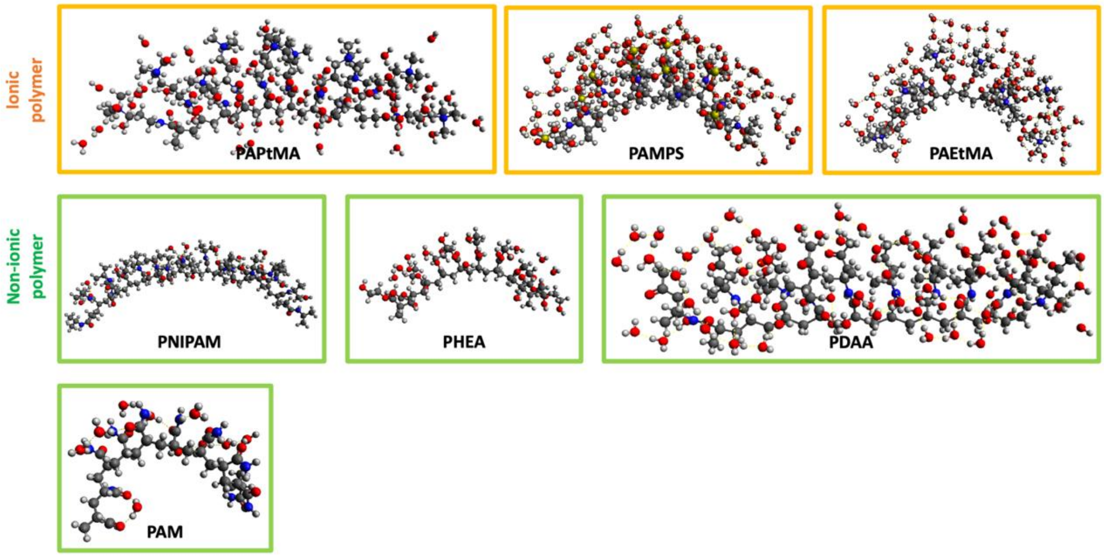

Figure 3.3 Molecular simulation images of PAM, PAMPS, PAEtMA, PAPtMA, PNIPAM, PHEA and PDAA with water molecules randomly distributed.

In this study, we defined the hydrogel swelling ratio (SR) as the mass ratio of saturated hydrogel to the dry gel. Due to their stronger water affinity, the anionric PAMPS and cationic PAEtMA and PAPtMA hydrogels exhibited a higher SR of >25 compared to other AWH hydrogels (**Table 3.1**). This result is attributed to their high polarity of pendant groups and their strong interactionr with water molecules. For the neutral hydrogels, the PNIPAm has a relatively higher SR of 9.9 and the PDAA shows the lowest SR of 4.6. The SR values of the prepared AWH hydrogels are in the order of PAPtMA > PAMPS > PAEtMA > PNIPAM > PAM> PHEA > PDAA.

Finally, we plotted the SR versus |ΔE| of AWH hydrogels. As seen in **Figure 3.4**, the |ΔE| values of AWH hydrogels is near-linearly related to their SR with a R^2 of 0.9919. This result implies that the driving force for water absorption of hydrogels also correlates to the ultimate water storage capacity of the hydrogel to some extent.

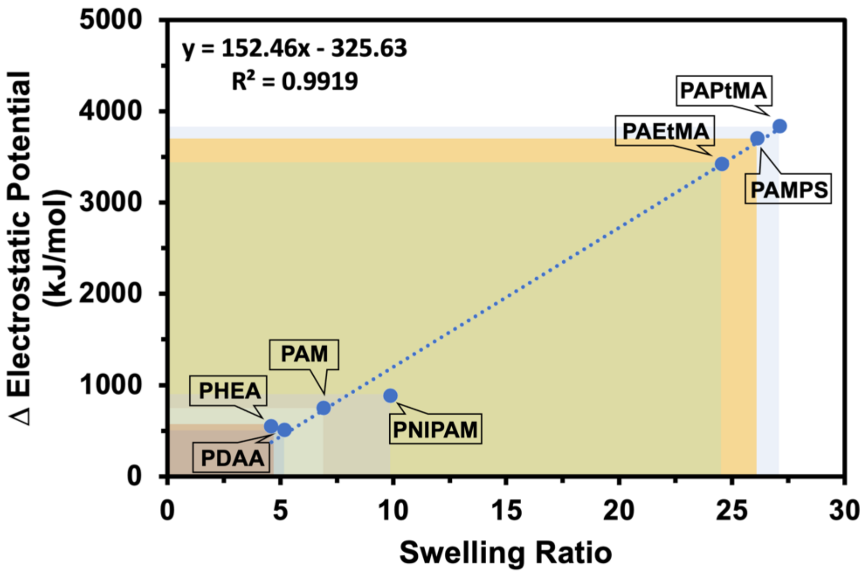

Figure 3.4 Near linear fitting of the swelling ratio and electrostatic potential difference.

Table 3.1 Summary of AWH hydrogels with their chemical structure, electrostatic potential mapping, absolute value of electrostatic potential difference, and swelling ratio.

Monomer	Structure[a]	Electrostatic Potential Map[b]	|EPD|[c] (kJ/mol)	Swelling Ratio (100%)
APtMA	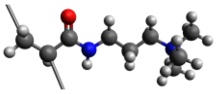	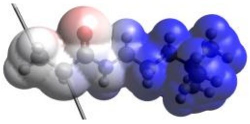	3835	27.1
AMPS	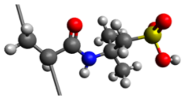	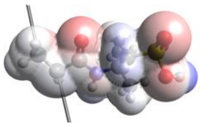	3702	26.1
AEtMA	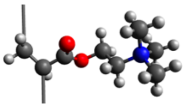	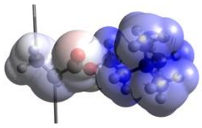	3420	24.6
NIPAM		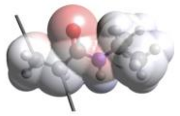	1379	9.9
AM	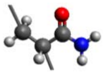	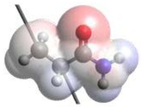	848	6.9
HEA	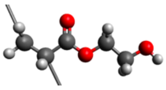		732	5.2
DAA	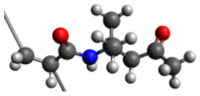	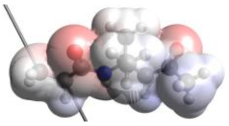	550	4.6

[a] Grey: C; White: H; Red: O Blue: N and Yellow: S. [b] Electrostatic potential mapping: Blue: positive, Red: negative. [c] Absolute value of electro-potential difference.

3.3.3 Water adsorption and desorption performance

The resulting dry hydrogels were then placed on a hydrophobic foam in a beaker containing DI water, and the static water adsorption test was carried out for 12 hours. The beaker is sealed with parafilm to isolate the outside air, and the humidity inside the beaker can be tuned by adjusting the temperature (**Figure 3.5A**). The weight of the hydrogel was recorded at different time intervals. The sorped water was then desorbed under solar irradiation (**Figure 3.5B**). Water evaporation rates and desorption efficiencies of all the AWH hydrogels were derived by measuring the mass change of the hydrogels every 30 min using a precision balance. Of particular note, the water adsorption performance of the AWH hydrogels are obtained by calculating the average of three cycles.

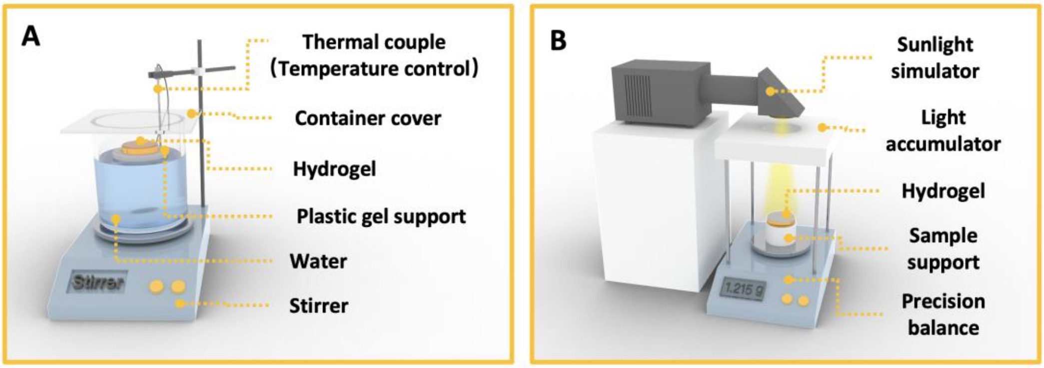

Figure 3.5 Water adsorption (A) and desorption (B) apparatus illustration.

To quantity the water sorption performance of these AWH hydrogels, a 12 h continuous water sorption test under 60% humidity was performed. Each sample was conducted three individual water adsorption/desorption experiment under the same conditions for greater accuracy. The calculation of data variant is based on the following equation, where σ: variant, n: data total amount, X_i: water uptake for each experiment, $\bar{X}$: average water uptake for each sample:

$$\sigma^2 = \frac{\sum_{i=1}^{n}(X_i - \bar{X})^2}{n}$$

The average water uptake and average water desorption efficiency reflects the maximum difference percentage of each group of water adsorption and desorption data, which is calculated via the following equation:

$$Error\ percentage = MAX[\frac{(X_i - \bar{X})}{\bar{X}} \times 100\%]$$

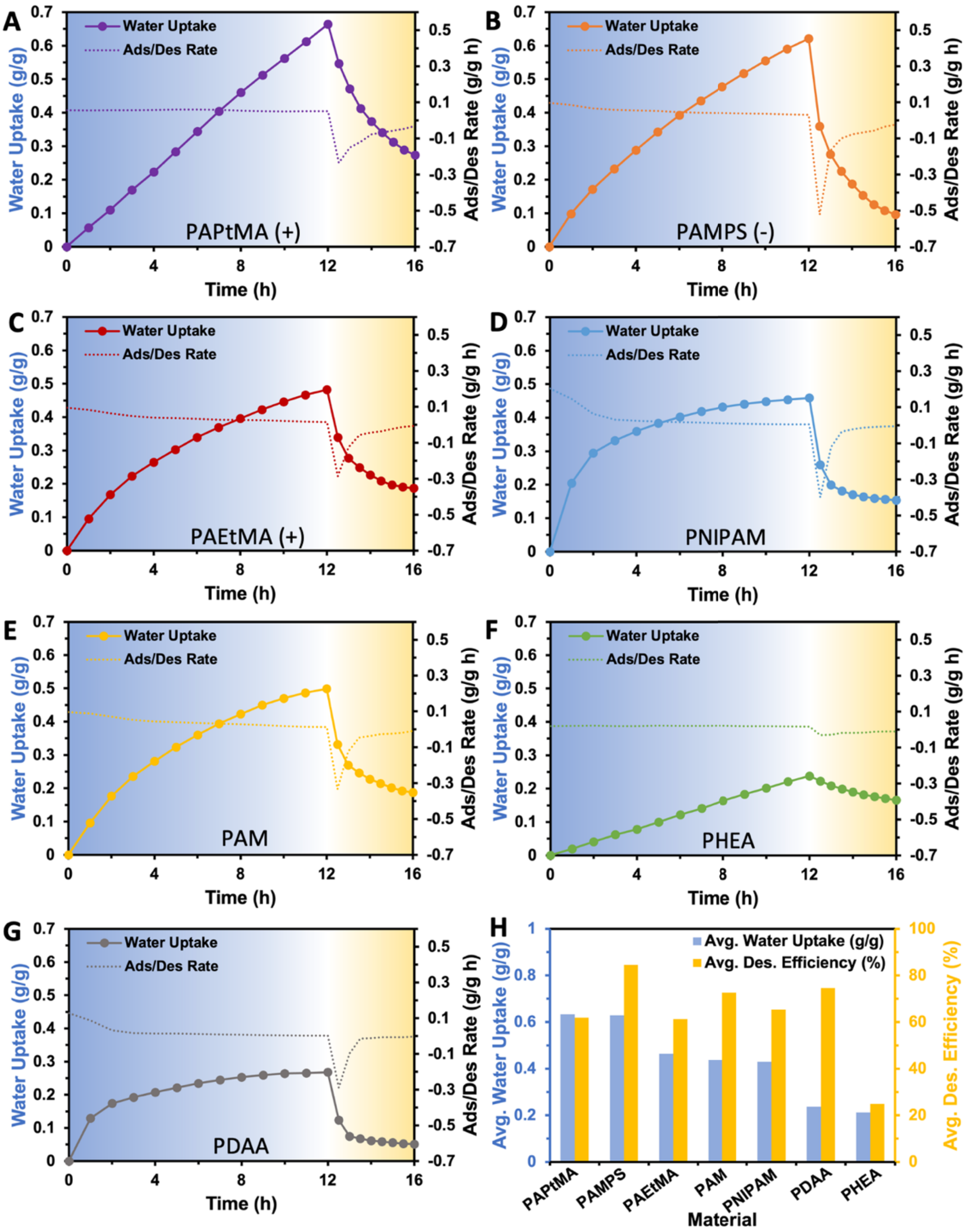

Figure 3.6 (A-G) 12 h water adsorption and 4 h water desorption curves and their adsorption/desorption rates of the AWH hydrogels, each sample were concucted three times for higher accuracy. Water desorption is conducted under 1 kW m^{-2} (1.0 sun equivalent). (H) Comparison of average water adsorption capacity and water desorption efficiency for AWH

hydrogels.

At the molecular level, charged hydrogels (i.e. PAEtMA, PAPtMA, and PAMPS) have a greater affinity for water molecules than uncharged ones, which explains why they have greater water sorption capacities than neutral hydrogels. The water sorption of hydrogels is, however, influenced by the type of ionic functional groups present in the "stationary" phase (polymer chains with fixed position). PAPtMA had the highest water sorption capacity of 0.634 g g^{-1}, followed by PAMPS (0.621 g g^{-1}) and PAEtMA (0.482 g g^{-1}) (**Figure 3.6A-C**). The neutral hydrogels (i.e. PNIPAM, PAM, PHEA and PDAA) have low water uptake capacity of 0.317 g g^{-1}, 0.303 g g^{-1}, 0.239 g g^{-1} and 0.237 g g^{-1}, respectively. We also prepared a controlled hybrid hydrogel poly(AMPS-co-AEtMA) by copolymerizing AMPS and AEtMA monomers. Interestingly, the water adsorption capacity of poly(AMPS-co-AEtMA) hydrogel is 0.5063 g g^{-1}, which is between PAEtMA and PAMPS. At molecular level we also found a relationship between the side-chain length and the water adsorption capacity. In Avogadro's molecular simulations, the flexibility of the polymer backbone decreases with the increase of side chain length, which makes the hydrophilic functional groups on the side chains are completely exposed to the activity space of water molecules. On the other hand, the relative angles between the polymer side chains are not completely fixed. The side chain can point in any direction normal to the plane of the backbone direction (this is especially apparent when the ends of the side chains contain large hydrophilic functional groups, such as PAEtMA), which means that the spatial hinderance of water molecules to enter the space near the main chain is weakened, resulting in an increase in the water-absorbent properties of the hydrogel.

Under sunlight irradiation, all the AWH hydrogels showed a relatively high desorption efficiency of more than 60%, except for PHEA hydrogel. This result may be due to the near closure of the pores on its surface. Notably, during the desorption process the initial water desorption rates are in the order: PAMPS (0.43 g g^{-1} h^{-1}) > PNIPAM (0.39 g g^{-1} h^{-1}) > PAM (0.34 g g^{-1} h^{-1}) > PAEtMA (0.28 g g^{-1} h^{-1}) > PDAA (0.24 g g^{-1} h^{-1}) > PAPtMA (0.23 g g^{-1} h^{-1}) > PHEA (0.02 g g^{-1} h^{-1}) (**Figure 3.6**). Although PAPtMA has the best water adsorption performance, it showed a compromised desorption efficiency of 62%. The desorption efficiency of PAMPS was much higher at 83% while still having good adsorption capacity, which means that PAMPS hydrogel are more advantageous in fast adsorption/desorption cycles compared to PAPtMA.

We then illustrate the structure-property-application relationships of the AWH hydrogels. We directly compared the water sorption driving forces determined by molecular simulations, experimentally obtained SRs and the water sorption capacities of the hydrogels. As seen from **Figure 3.7**, the PAPtMA hydrogel exhibited the highest SR value and the largest $|\Delta E|$, and therefore the highest water adsorption capacity, similar as PAMPS and PAEtMA. As expected, the SR and $|\Delta E|$ of the neutral hydrogels PNIPAM, PAM, PHEA and PDAA graduately decreased, as did their water adsorption capacity. In **Figure 3.4**, the monochromatic region visually represents the product of SR and $|\Delta E|$ for AWH hydrogels. The area of this region is ranked in the following order of size: PAPtMA > PAMPS > PAEtMA > PDMA > PNIPAM > PAM > PHEA > PDAA.

Interestingly, this order is consistent with the trend of high to low AWH performance of the AWH materials. In all, this result indicates that the water sorption capacity of hydrogel is affected by both volumetric water swelling capacity and chemical structure.

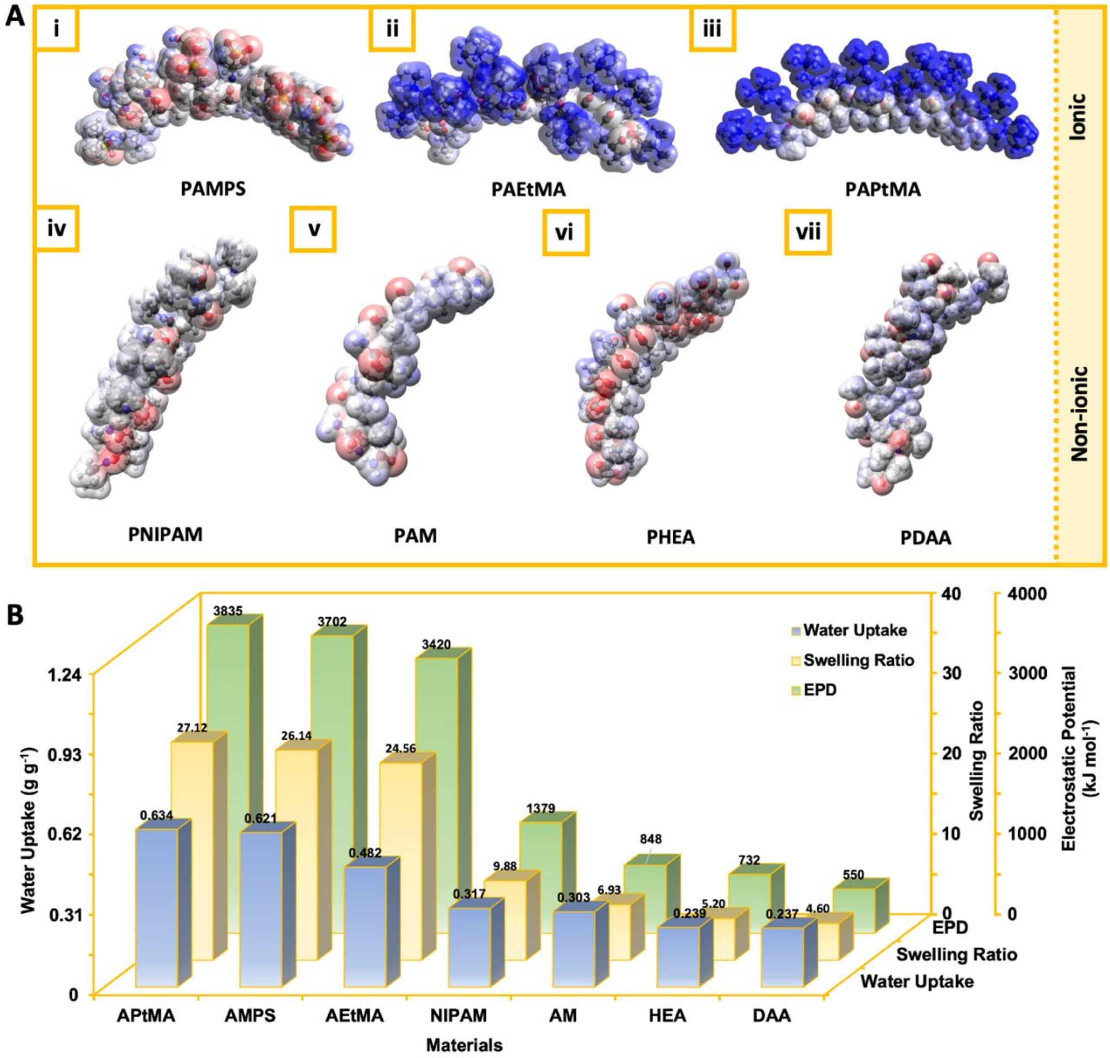

Figure 3.7 (A) Electrostatic potential difference of PAPtMA, PAMPS, PAEtMA, PNIPAM, PAM, PHEA and PDAA polymer chains (each polymer chain is presented with ten monomers for better trend illustration). Dark gray dots: carbon, light gray dots: hydrogen, blue dots: nitrogen, red dots: oxygen, yellow dots: sulfur. (B) Positive correlation of water adsorption capacity with the absolute value of electro-potential difference and swelling ratio of the hydrogels.

It is particularly noteworthy that to develop high-performance AWH materials for practical applications, we need them to have balanced water adsorption capacity and desorption efficiency. After comprehensive consideration, PAMPS in this study is considered as the most promising AWH material. We next tested the water adsorption-desorption performance of the PAMPS hydrogels under different relative humidity conditions, and demonstrated the excellent all-weather water adsorption capacity of PAMPS hydrogels under 30-90% R.H. conditions (**Figure 3.8**).

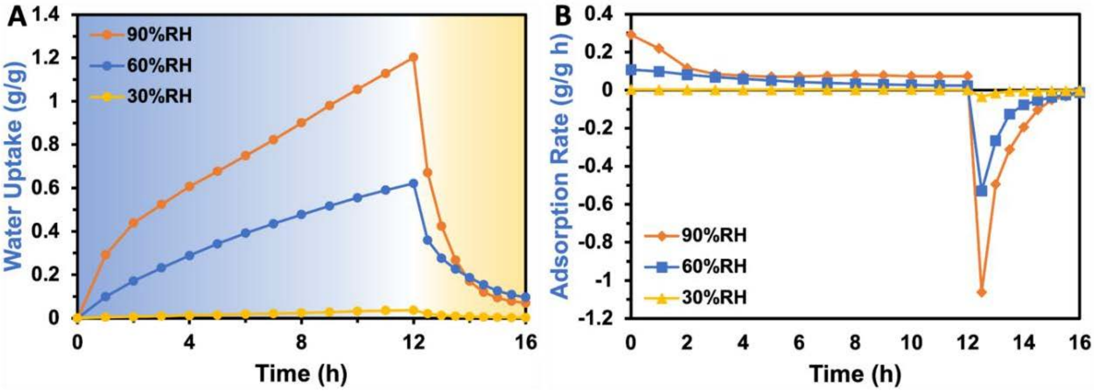

Figure 3.8 (A) Water adsorption and desorption performance of PAMPS hydrogel at 30%, 60%, and 90% RH environment. Water desorption is tested under 1.0 sun irradiation. (B) Water adsorption and desorption rate of PAMPS hydrogel at 30%, 60%, and 90% RH environment. Water desorption is tested under 1.0 sun irradiation.

To further improve the desorption efficiency, we incorporated three PTMs into PAMPS hydrogel, including manganese-polydopamine nanoparticles (PDA(Mn)NPs) and carbon-based PTMs such as carbon nanotubes (CNTs) and graphene oxides (GOs). We found that the PAMPS+PTM composite hydrogels displayed a reduced water adsorption capacity. Among them, the water sorption capacity of PAMPS+GO hydrogel was reduced by 7% compared to the pristine PAMPS, followed by PAMPS+CNT (-9.5%) and PAMPS+PDA(Mn)NPs (-15%) (**Figure 3.9A**), since the PTMs display a lower adsorption capacity (< 0.1 g g^{-1}) compared to PAMPS hydrogel, the resulting composite gels had a reduced water absorption capacity. The water adsorption rate of these composite hydrogels are shown in **Figure 3.10**. All composite hydrogels exhibited excellent solar-to–heat conversion. Specifically, after 4 hours of continuous light exposure, the temperature of PAMPS+GO hydrogel reached an astonishing 75.9 °C, followed by PAMPS+CNT hydrogel (73.7 °C), PAMPS+PDA(Mn)NPs hydrogel (61.2 °C) and pristine PAMPS hydrogel (40.3 °C) (**Figure 3.9B**). The infrared images also recorded the temperature changes of the composite hydrogels (**Figure 3.9C**). In the wavelength range of 300-1900 nm, the light absorption of GO is significantly stronger than that of CNT. However, in the 1900-2400 nm range CNT can absorb more electromagnetic wave energy. As a result, the photothermal conversion performance of CNTs was the most pronounced during the desorption of water, and the water desorption rate of the PAMPS+CNT is 0.75 g g^{-1} h^{-1}. Although the incorporation of GOs also increased the temperature of the hydrogel to 75.9 °C, the desorption rate of PAMPS+GO was 0.61 g g^{-1} h^{-1}. We hypothesized that the large number of oxygen-containing functional groups in GO (e.g. epoxy, hydroxyl and carbonyl groups) formed additional H-bonding with water molecules, leading to reduced evaporation rate.

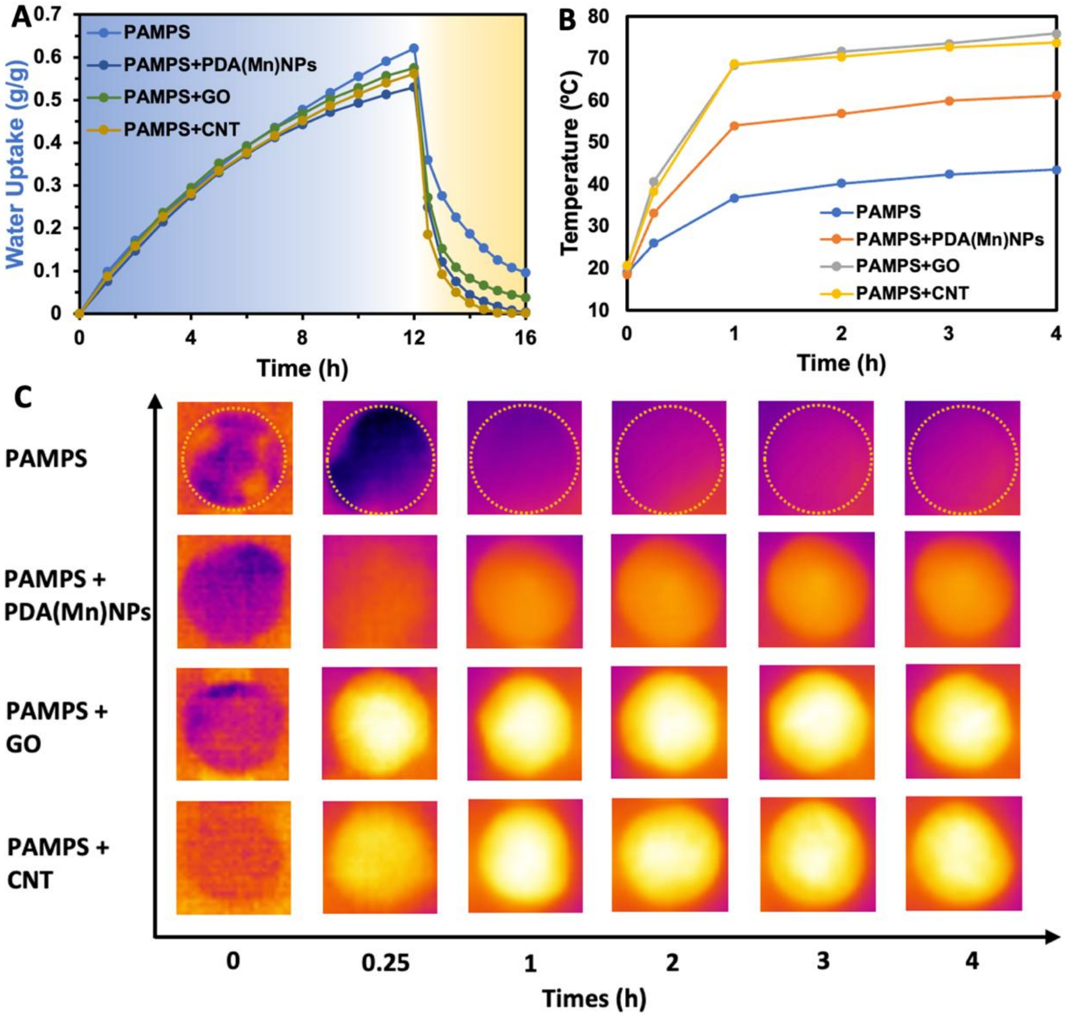

Figure 3.9 (A) Water adsorption and desorption process of PAMPS hydrogel with PDA(Mn)NPs, GO, and CNT as photothermal converter. (B) Temperature changing with sunlight irradiation time of PAMPS hydrogel with PDA(Mn)NPs, GO, and CNT as photothermal converter. (C) Infrared images of PAMPS hydrogel with PDA(Mn)NPs, GO, and CNT as photothermal converter at 0 h, 0.25 h, 1 h, 2 h, 3 h, and 4 h of sunlight irradiation. The simulated solar irradiation intensity during the experiment was maintained at 1.0 sun.

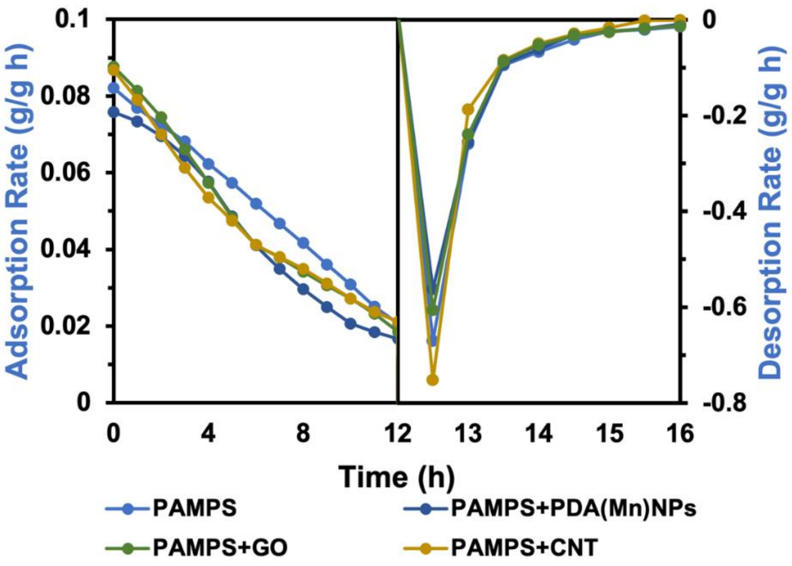

Figure 3.10 Water adsorption and desorption rate of PAMPS (Light blue trace), PAMPS+GO (Green trace), PAMPS+CNT (Yellow trace), and PAMPS+PDA(Mn)NPs (Dark blue trace) hydrogels. Water desorption is under sunlight irradiation with 1.0 sun equivalent energy.

In addition, the thermal stability of the two composite hydrogels (PAMPS+GO and PAMPS+CNT) was tested by three 24 h sun exposure tests (1.0 solar equivalent). As shown in **Figure 3.11**, the surface temperatures of both samples exceeded 70 oC after 24 h of irradiation (1.0 sun equivalent). Furthermore, both composite hydrogels retained their structural integrity after three cycles of irradiation, demonstrating their excellent thermal stability.

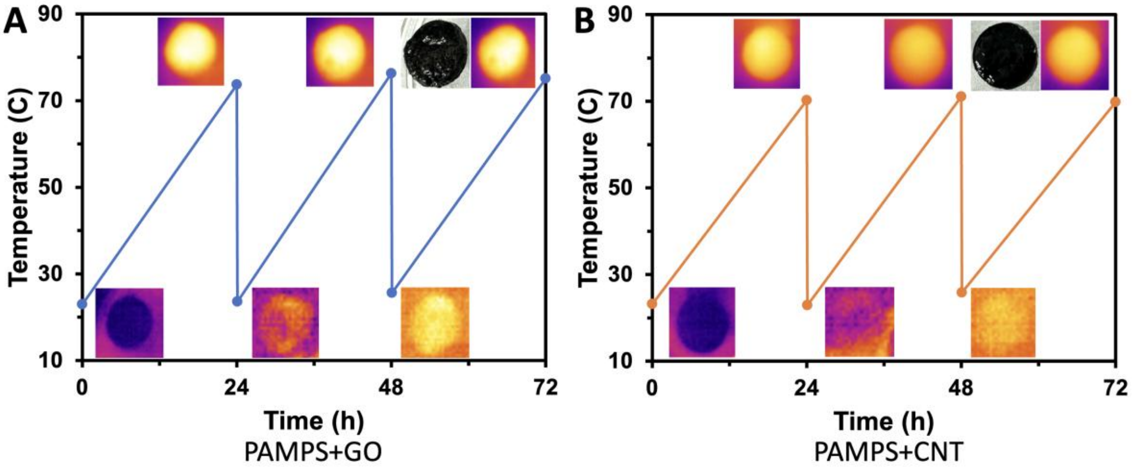

Figure 3.11 Three 24-hour sunlight exposures tests for (A) PAMPS+GO and (B) PAMPS+CNT hydrogels. The inserted are their IR images.

3.3.4 Practical outdoor performance and durability

Finally, the outdoor water production test of PAMPS hydrogel was conducted in June 28-29, 2023, Ultimo, NSW, Australia, from 16:00 on June 28, 2023 to 6:00 on June 29, 2023. During the practical test, the temperature was basically maintained at about 11 °C, the wind speed gradually increased from 3.6 m s^{-1} to about 7.7 m s^{-1}, the R.H. gradually decreased to 67%, and the dew point changed with the change of relative humidity (**Figure 3.12A**). The water production device used in practical experiment is shown in **Figure 3.12B**, with actual digital image showed in **Figure 3.1**. A PAMPS hydrogel achieved a water sorption capacity of 0.42 g g^{-1} in 8 h and then released 85% of captured water under sunlight irradiation. We then tested the performance stability of PAMPS hydrogel in cycling tests and found that the PAMPS hydrogel is mechanically robust enough to support long-term (i.e. over 120 h) continuous water sorption/desorption cycles without performance degradation. Its water adsorption capacity maintained at 0.42 g g^{-1} after 10 water adsorption/desorption cycles (**Figure 3.12C**). Moreover, we analyzed the ions concentrations of the collected water. The concentrations of sodium, magnesium, potassium, and calcium ions in the collected water are significantly lower than DI water and Sydney Tap water (**Figure 3.12D**), and fully met the drinking water standards stipulated by the World Health Organization (WHO). This result demonstrates that PAMPS hydrogels have great potential in the field of AWH application.

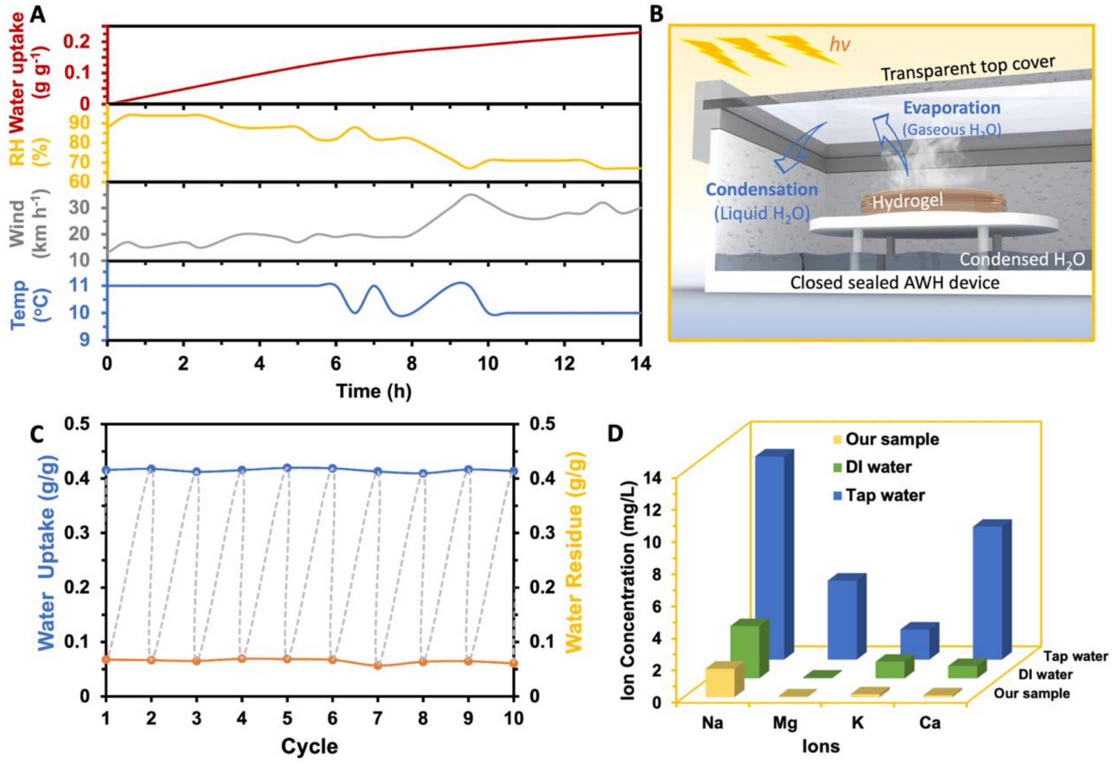

Figure 3.12 (A) Actual change of temperature, wind speed, relative humidity, and water adsorption data of PAMPS hydrogel at 28th June 2023, location at Ultimo of New South Wales, Australia. Original weather data is obtained from The Bureau of Meteorology of Australian Government, presented by Apple Weather application (iOS version: 16.6). (B) Water desorption

device used in pretical experiment. (C) AWH performance of PAMPS hydrogel in 10-times cycling tests. (D) ICP-MS ions concentration analysis graph for commonly water-soluble ions.

3.3.5 Conclusion

In conclusion, we evaluated a series of hydrogels for AWH and systematically investigated their water sorption mechanisms and desorption kinetics. Based on scanning electron microscopy analysis, electrostatic potential mapping, and water sorption/desorption curves, we determined the impact of the chemical structure on AWH performance of hydrogels. The electrostatic potential difference provides the driving force for water sorption in hydrogels, and the swelling ratio also has a significant impact on the water sorption capacity of AWH hydrogels. We also studied the effect of the PTMs on the desorption efficiency of hydrogels. This study thus provides new insights to elucidate the current research gap in structure-property-application relationships and provide research directions for the design and synthesis of hydrogel-based AWH materials.

Chapter 4 Thermodynamic Study of Water Desorption Process in Hydrogel AWH Materials.

This chapter investigates the performance of polyacrylamide (PAM)-based hydrogels for atmospheric water harvesting (AWH) under varying humidity conditions. It establishes a link between the enthalpy of evaporation and initial water desorption rates, shedding light on the energy dynamics involved. Raman spectroscopy is used to differentiate free and intermediate water, with the results showing that hydrogels with superior adsorption capacities contain higher levels of intermediate water. Among the materials tested, PAM hydrogels integrated with Fe-ethanolamine coordination networks demonstrate optimal adsorption (1.03 g g^{-1} at 90% humidity) and efficient desorption performance, attributed to enhanced binding sites. The chapter highlights the critical importance of understanding thermodynamic principles in the design of sustainable, high-performing AWH materials for addressing global water scarcity. Chapters 3 and 4 focus on different aspects of hydrogels in the AWH process. Together, these chapters provide a foundation for the more advanced discussions in Chapters 5 and 6.

4.1 Introduction

The technology for obtaining fresh water through desalination technology is gradually falling into a bottleneck due to its large investment and high energy consumption[152-154]. As a result, attention has turned to new and more cost-effective water production technologies, such as harvesting fresh water from the air, to alleviate the issue of uneven distribution of fresh water resources. Surface freshwater resources on Earth account for 1.3% of the total freshwater resources, with 0.3% stored in the air that humans rely on for survival, amounting to approximately 2×10^{10} cubic meters (in terms of liquid water)[155-157]. Although the technology for collecting dew through porous networks and hydrophobic spiked arrays (atmospheric fog collection) in sufficiently humid air (saturated water vapor, i.e., fog) has gradually matured[158-161], there are still many challenges in harvesting, storing, and releasing liquid water under conventional climatic conditions (unsaturated water vapor)[48]. This is referred to as AWH technology.

In recent years, AWH materials based on metal-organic frameworks (MOFs)[162-164], inorganic hygroscopic salts[165-167], and ionic liquids[81, 168] have been continuously explored, demonstrating the potential for AWH under complex climatic conditions. However, these materials have not been able to achieve the design goals of miniaturization, low cost, and low energy consumption of AWH devices due to their low durability, difficulty in removing residual water, and ion leaching[169-171]. Hydrogels, with their advantages of simple and fast synthesis, customizable functionality, and high swelling ratio, have gradually replaced hygroscopic salts and other standalone AWH materials. Hydrogels applied in AWH applications often incorporate a variety of additives, such as the addition of inorganic hygroscopic salts to enhance the liquefaction to surface water, the introduction of ionic monomer to increase the structural hydrophilicity, or the use of photothermal materials (e.g. GO, CNT, PPy-Cl) to endow the hydrogel with photothermal conversion capacity[130]. Indeed, most of the current research focuses on improving the water adsorption properties of hydrogels, but the study of the desorption process of hydrogels has been neglected. The desorption process, in turn, is very important because it is the key to improve the daily water yield of hydrogel-based AWH materials[172-173].

Herein, we synthesized PAM-based AWH materials. We also compared the energy consumption of PAM hydrogels with different amounts of water in the desorption process by measuring the enthalpy of evaporation of adsorbed water. In addition, we determined the intermediate and free water contents of the adsorbed water using Raman spectroscopy. We found that the proportion of intermediate water was higher in PAM hydrogels with higher water adsorption content (under 95% R.H.) compared to hydrogels with lower water content (under 60% R.H.). This indicates that water adsorbed into the hydrogel undergoes a binding process. During desorption process, the AWH hydrogels with a higher proportion of intermediate water exhibited lower initial desorption rates.

4.2 Experimental section

4.2.1 Materials and synthesis procedure

All chemicals were purchased from Merck (Sigma-Aldrich). Acrylamide (AM >99%), Iron(III) chloride hexahydrate ($FeCl_3{\cdot}6H_2O$, 97%), graphene oxide (GO, 15-20 sheets, 4-10% edge-oxidized, average number of layers: 15-20), ethanol (EtOH, >99.5%), ethanolamine (EtAmine, >99%), N,N′-methylenebis(acrylamide) (BIS, 99%), N,N,N′,N′-tetramethylethylenediamine (TEMED, 99%), and ammonium persulfate (APS, 98%) were used as received without further purification, unless otherwise stated. Deionized water (DI water) was obtained by Milli-Q water purification system (18.2MW.cm @25 °C).

For a typical synthesis of the PAMGO hydrogel, 0.143 g AM (monomer, 2 mmol), 0.02 g BIS (crosslinker, 0.12 mmol), 0.002 g GO (photothermal converter, 1.2 wt%), and 0.01 ml TEMED (catalyst) were mixed and dissolved in 1.9 mL DI water under sonication (solution A, [M]:[XL] = 16). 0.016 g APS (initiator) was dissolved in 0.1 mL DI water under sonication (solution B). To trigger the gelation, solution B was added into solution A to induce polymerization. The polymerization of hydrogel was carried out for 1 h at room temperature. The as-prepared hydrogel was soaked in DI water for 1 h before dried 1.5 h under simulated sunlight irradiation to remove unreacted residue, then freeze-dried for 12 h before vapor adsorption tests.

For a typical synthesis of the PAMGOSalt hydrogel, 0.143 g AM (monomer, 2 mmol), 0.02 g BIS (crosslinker, 0.12 mmol), 0.002 g GO (photothermal converter, 1.2 wt%), and 0.01 ml TEMED (catalyst) were mixed and dissolved in 1.9 mL DI water under sonication (solution A, [M]:[XL] = 16). 0.016 g APS (initiator) was dissolved in 0.1 mL DI water under sonication (solution B). 10.81 g iron(III) chloride hexahydrate ($FeCl_3 \cdot 6H_2O$, 0.04 mol) was dissolved in 100 ml EtOH for 30 mins under sonication, then 0.105 ml ethanolamine was added into the $FeCl_3$ solution. After that, same volume of DI water was added (solution C). To start the gelation, solution B was added into solution A to induce polymerization. The polymerization of hydrogel was carried out for 1 h at room temperature. The as-prepared hydrogel was soaked in DI water for 1 h before dried 1.5 h under simulated sunlight irradiation to remove unreacted residue, then freeze-dried for 12 h. The prepared dry hydrogel was then immersed in solution C until fully moisturized, followed by 12 h of vacuum oven drying.

4.2.2 Characterizations

UV-VIS-NIR spectra of these AWH hydrogels were recorded on a SHIMADZU UV-1700 UV-Visible spectrophotometer.

Fourier-transform infrared spectroscopy (FT-IR) spectra was obtained using a SHIMADZU MIRacle 10 single reflection ATR accessory.

Scanning electron microscope (SEM) images of hydrogels were obtained by Zeiss EVO LS15 SEM system.

Infrared thermometer images of hydrogels under sunlight irradiation were captured using FLUKE PTi120 thermal imager.

Raman spectrum for bound water & free water content measurement were obtained using RENISHAW® inVia Raman Microscope with 532 nm laser source.

Differential Scanning Calorimetry (DSC) analysis for evaporation enthalpy measurement were obtained using NETZSCH DSC300 Supreme calorimeter.

Inductivity coupled plasma mass spectrometry (ICP-MS) was used to analyse for ions concentration comparison of condensed water from AWH hydrogels. An Agilent Technologies 7900 ICP-MS system with SPS-4 Autosampler was used in this study.

Sunlight simulation light source was purchased from Beijing NBeT HSX-F300 xenon light source.

4.2.3 Moisture adsorption experiments

The moisture adsorption tests were conducted in a static moist environment at a fixed relative humidity with temperature monitoring (**Figure 4.1**). Prior to the moisture adsorption experiment, 3/4 volume of DI water was placed in a 1,000 mL beaker. A thick polystyrene bubble foam was cut into a plate and floated on the water surface inside the beaker to support the hydrogel and a hygrometer. The top of the beaker was completely sealed with parafilm to prevent water vapor leakage and to ensure accurate relative humidity monitoring. The PS form's area, which is slightly smaller than the water surface area, serves as a source of water molecules, adjusting the density of water molecules in the air (i.e., absolute humidity). By heating the water, more water molecules are released into the air, thereby influencing the absolute humidity. Since air temperature and pressure are assumed to remain constant, a direct relationship can be established between absolute humidity and relative humidity. The moisture adsorption experiment was conducted over 12 h, with the mass of the hydrogel recorded every 60 mins.

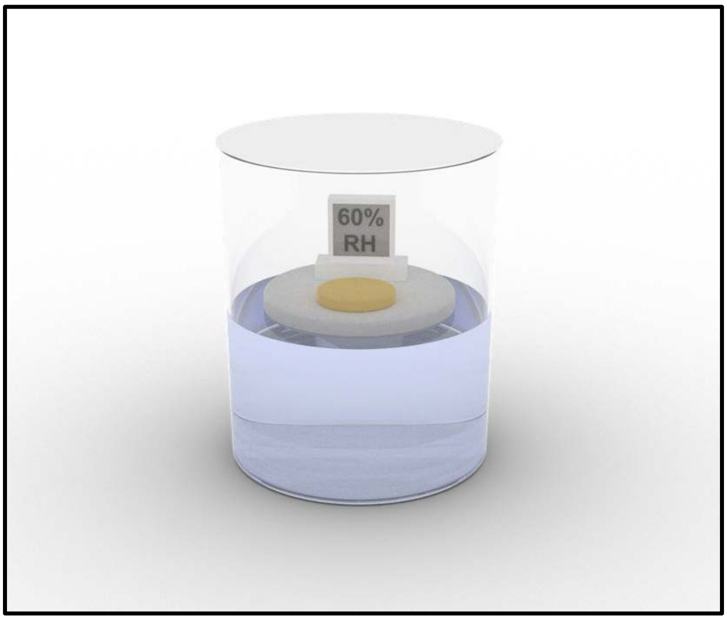

Figure 4.1 Experiment apparatus illustration (inside clear view) for in-door water adsorption experiment. Yellow: hydrogel, grey: polystyrene floating support, blue: DI water.

4.2.4 Sunlight-assisted autonomous water release

The indoor sunlight-assisted evaporation experiment was conducted using a XE300WUV Xenon light source (Beijing NBeT Technology Ltd) to simulate sunlight. The irradiation intensity was maintained at 1,000 W m^{-2} (equivalent to 1.0 sun). The mass of the hydrogel was monitored every 30 mins using an analytical balance with internal calibration (OHAUS Pioneer analytical balance). The surface temperature of the hydrogel was measured with an IR camera (FLUKE PTi120 thermal imager).

4.2.5 Durability test

The durability of the hydrogel material was assessed at 60% relative humidity over 10 cycles. Each cycle consisted of an 8-hour water adsorption phase followed by 4 h of indoor sunlight irradiation. At the conclusion of each cycle, the hydrogel underwent an additional 1 h irradiation to eliminate any remaining water residue.

4.3 Results and discussion

4.3.1 The synthesis of AWH hydrogels

Current research on AWH hydrogels has mainly focuses on the empirical selection of monomers and additives to enhance water adsorption capacity, thereby neglecting the essential prerequisite of quantitatively analyzing the thermodynamic parameters of water desorption. This knowledge gap hinders the design and fabrication of high-performance hydrogel-based AWH materials. In this study, we synthesized AWH hydrogels by radical polymerization method as show in **Figure 4.2A**. N,N'-methylenebis(acrylamide) (BIS) and ammonium persulfate (APS) were used as the crosslinker and free radical initiator, respectively. We synthesized PAM and PAMGO hydrogels through free radical polymerization of monomers and crosslinkers, with one of the PAMGO hydrogels further soaked in metal salt solutions that crosslinked by coordination reaction and subjected to high-temperature vacuum drying to incorporate metal ions with stronger water affinity. All hydrogel samples, including PAM, PAMGO and PAMGOsalt, underwent the same washing and freeze-drying processes to ensure the comparability of their microporous structures. Adhering to a standard post-treatment protocol also allowed us to more specifically study the impact of evaporation enthalpy and the content of free and intermediate water on the thermodynamics of hydrogel desorption.

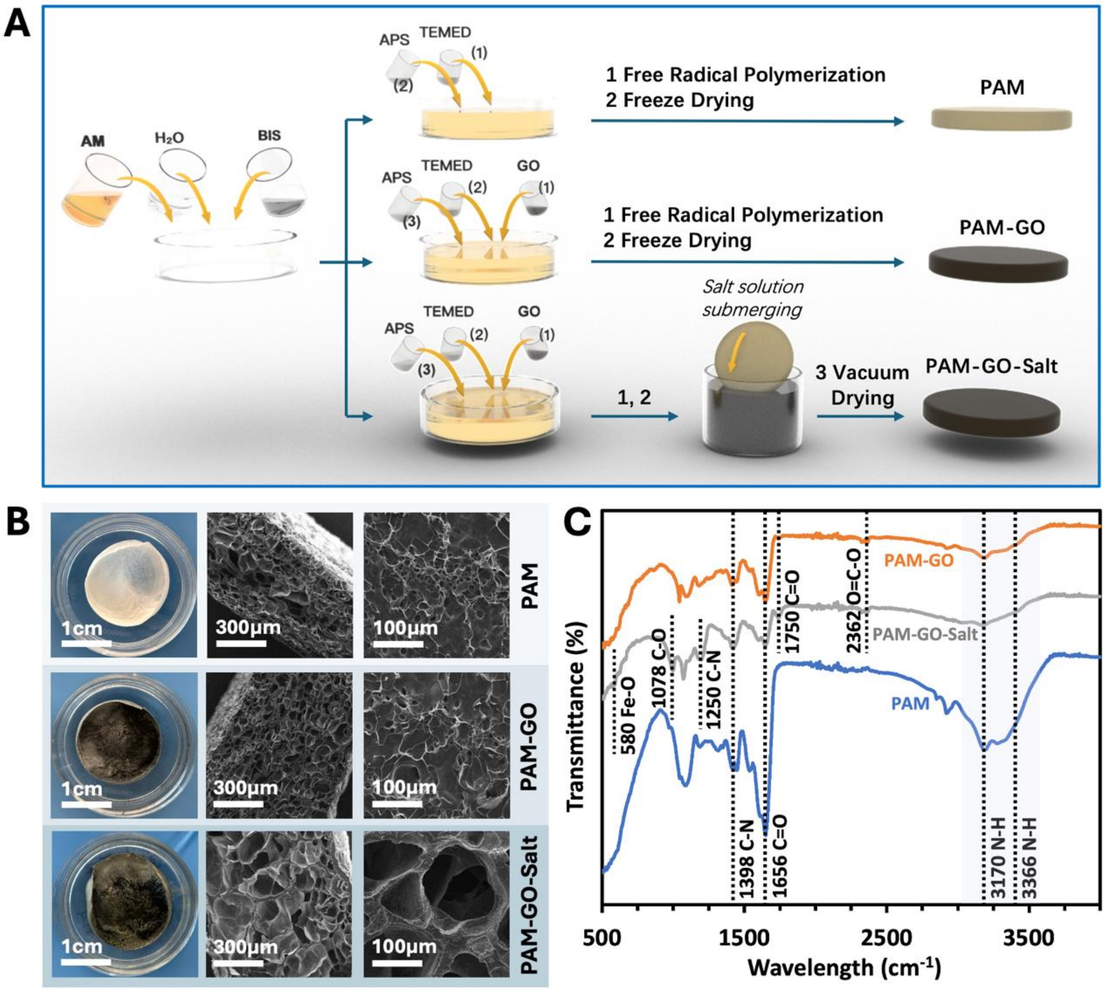

Figure 4.2 (A) Illustration of the synthesis procedure of PAM, PAMGO, and PAMGOSalt AWH hydrogels. (B) Optic and SEM images of PAM, PAMGO, and PAMGOSalt hydrogels. SEM images presented in two scales (50× and 150×). (C) FT-IR spectrum of PAM, PAM-GO, and PAM-GO-Salt hydrogels.

After freeze-drying, the hydrogel samples were subjected to SEM scanning to determine their surface morphology and FT-IR analysis to ascertain their chemical structure. **Figure 4.2B** shows the surface morphology of PAM, PAMGO, and PAMGOSalt hydrogels. It can be seen that the incorporation of GO does not significantly affect the hydrogel pore size and pore wall thickness, with the average pore size for both PAM and PAM-GO samples being 20 μm. The hydrogel samples treated with salt solution possess an irregular porous structure, with pore sizes ranging from approximately 50 to 130 μm. Noting that the dense macropores have potential advantages in the transport of liquefied water during water adsorption.

As shown in **Figure 4.2C**, we observed absorption peaks representing C-N stretching (located at 1398 cm^{-1}) and C=O stretching (located at 1656 cm^{-1}) for all the three samples. Additionally, absorption peaks at 3170 cm^{-1} and 3366 cm^{-1} were identified, representing N-H stretching in primary amides. After introducing GO into the PAM hydrogel, new absorption peaks at 1750 cm^{-1} and 2362 cm^{-1} were observed, which can be attributed to the C=O and O=C-O stretching of GO nanosheets. In the case of PAM-GO-Salt, the formation of Fe-coordination network was confirmed by the observation of 580 cm^{-1}, 1078 $cm^{-1}$and 1250 cm^{-1} peaks, which are attributed to the Fe-O, C-O and C-N stretching of coordination Fe-ethanolamine network. This result indicates the successful preparation of the PAM, PAMGO and PAMGOSalt hydrogels.

4.3.2 Water adsorption and desorption performance

The static water adsorption tests for hydrogel samples were conducted in a sealed container containing humid air. As shown in **Figure 4.1**, the sealed container was filled with DI water. A foam board floated on the water surface to support the hydrogel and the hygrometer. The humidity in the sealed air was controlled by the area of the foam board and the water temperature. Since the foam board area was slightly smaller than the water surface area, water vapor could reach the upper space from the water surface. The sealed container was placed on an electric heating plate, and as the water temperature increased, the vapor pressure on the water surface decreased, allowing more water molecules to enter the air, thereby adjusting the humidity.

We found that under low humidity (30% R.H.), medium humidity (60% R.H.), and high humidity (90% R.H.) conditions, the water adsorption capacity of the PAM-GO-Salt hydrogel was the highest, with 0.2 g g^{-1}, 0.54 g g^{-1}, and 1.03 g g^{-1}, respectively (**Figures 4.3A-C**). The introduction of the coordination network enhanced the water adsorption capacity of the hydrogel by 72.41% (30% R.H.), 16.63% (60% R.H.), and 24.49% (90% R.H.). This is because the open metal sites in the coordination network has a strong affinity to the water molecules in air, enhancing the water adsorption capacity of PAM hydrogel under a low RH% environment. With the increase of ambient humidity increases, the iron coordination network quickly reaches saturation, and then the water adsorption process of PAM replaces the coordination network to play a dominant role. The addition of GO to the PAM hydrogel only showed a 13.29% increase in water adsorption capacity at 60%R.H., while no significant effect was observed at 30%R.H. and 90%R.H. (**Figure 4.3F)**. As a control AWH material, calcium chloride showed a 4%

increase, a 26.8% decrease, and a 17.34% decrease in water adsorption capacity compared to the PAMGOSalt hydrogel at low humidity (30%R.H.), medium humidity (60%R.H.), and high humidity (90%R.H.), respectively (**Figure 4.3D**). The water adsorption rate of $CaCl_2$ is stable, and water molecules quickly form hydrates with Ca^{2+} and Cl^- ions. In all, the water adsorption rate of PAMGOSalt at 30% R.H. was better than that of $CaCl_2$, and PAMGOSalt also has a higher initial adsorption rate and water adsorption capacity at medium and high humidity environments.

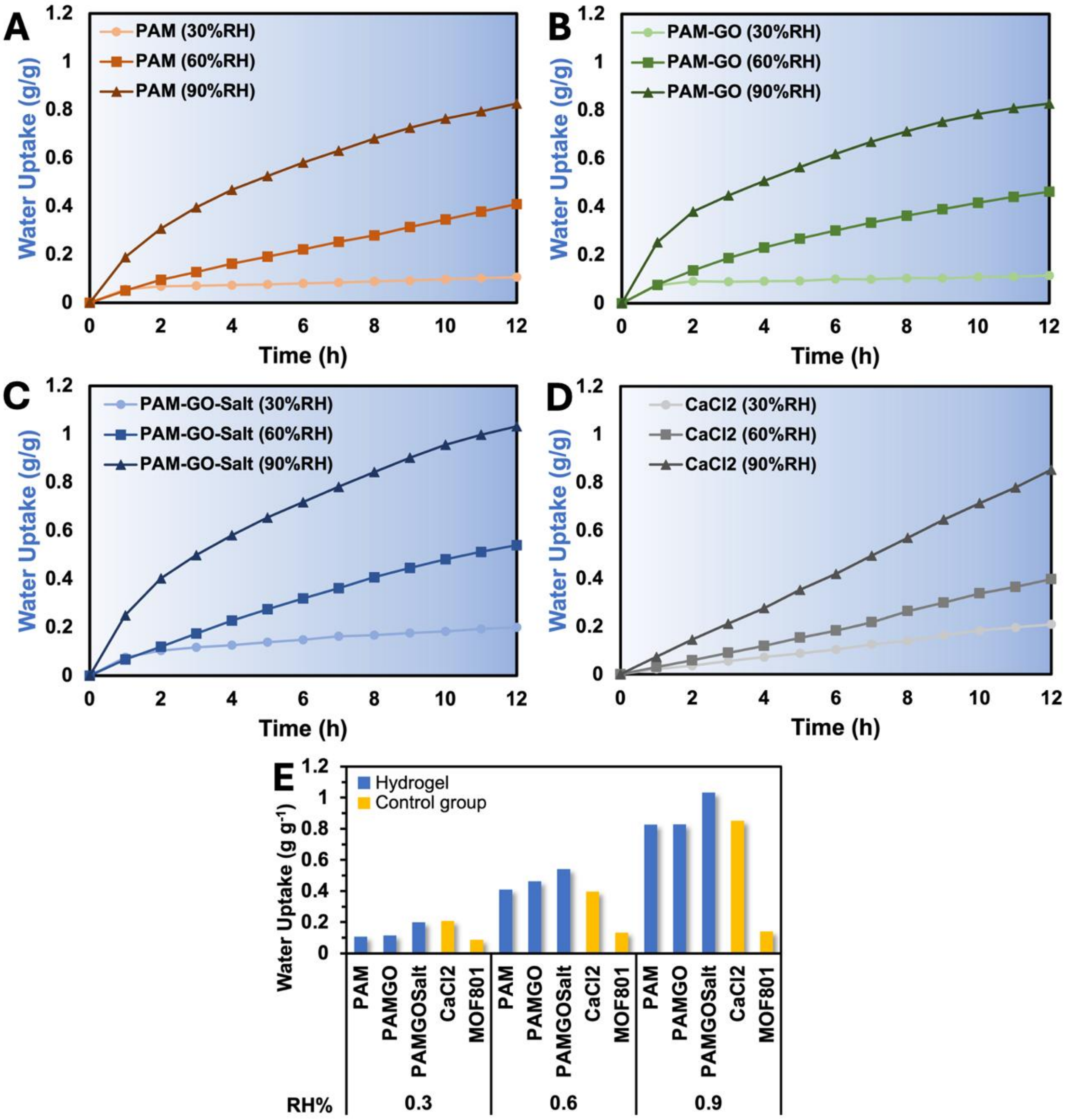

Figure 4.3 (A-D) In-door static water adsorption capacity plot at 30, 60, and 90%RH

environment using PAM, PAMGO, PAMGOSalt, and $CaCl_2$. (E) Water adsorption capacity comparison.

During the desorption process, hydrogel and $CaCl_2$ samples that had stored water internally were placed steadily on a precision balance, with a solar simulator positioned closely on one side of the balance. The intensity of the solar light source was consistently maintained at 1 kW m^{-2} (equivalent to 1.0 sun) by adjusting the vertical distance between the light source and the sample.

Under 4 h of irradiation, the PAM, PAMGO, and PAMGOSalt samples achieved 40 °C, 76 °C, 81 °C respectively, released 88%, 98%, and 91% of their capture water, respectively (**Figure 4.4A-C**). This indicates that all PAM, PAMGO, and PAMGOSalt hydrogels have stable thermal responsibility that not affected by water adsorption process. The time to release 50% of the water ($t_{0.5}$) was 25, 10, and 12 minutes, respectively (**Figure 4.5A**). Their water desorption efficiencies are shown in **Figure 4.5B**, with the initial desorption rate (absolute value) from high to low being PAMGO, PAMGOSalt, PAM, and $CaCl_2$. Among the samples that adsorbed water under 60% RH environment, PAMGO and PAMGOSalt had the highest initial desorption rates, approximately 0.01 g min^{-1}, while the $CaCl_2$ sample hardly released water (**Figures 4.5C, D**). Under the 30% RH environment, the PAMGOSalt hydrogel achieved a 98% desorption efficiency and the highest initial desorption rate (0.01 g min^{-1}) (**Figure 4.5 E, F**).

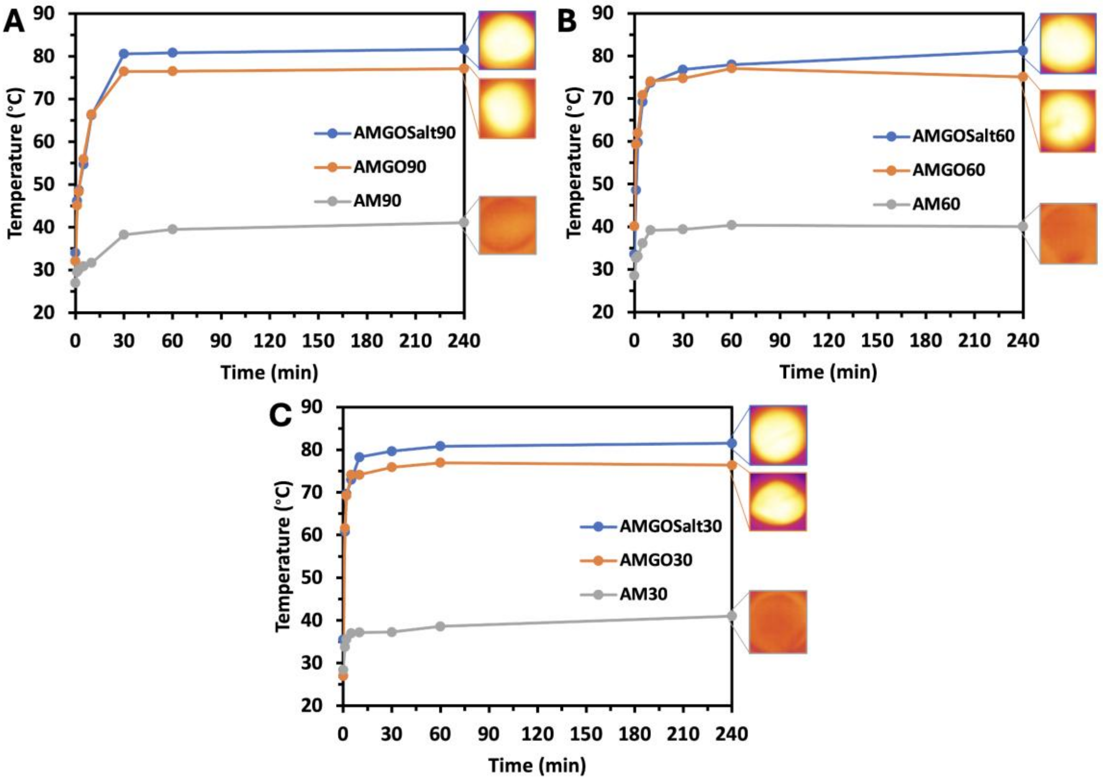

Figure 4.4 Temperature changes of PAM, PAMGO, and PAMGOSalt hydrogels after water adsorption under sunlight irradiation: (A) 90%RH, (B) 60%RH, and (C) 30%RH.

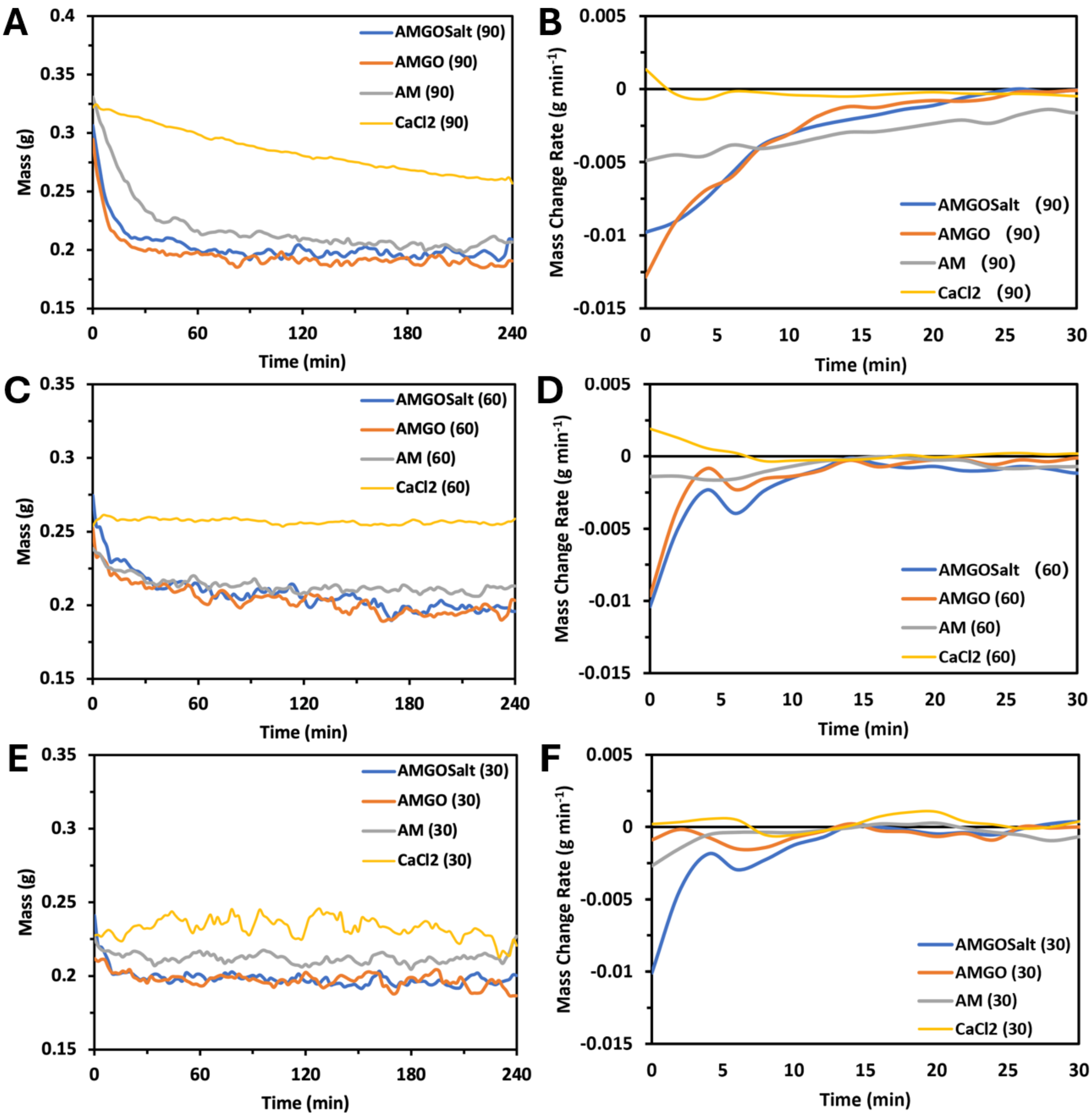

Figure 4.5 (A, C, E) In-door sunlight-assisted water desorption mass change using PAM, PAMGO, PAMGOSalt, and $CaCl_2$ with water adsorbed at 90, 60, and 30%RH environment. (B, D, F) In-door sunlight-assisted water desorption rate of PAM, PAMGO, PAMGOSalt, and $CaCl_2$ after water adsorption at 90, 60, and 30%RH environment.

To explain the differences in initial desorption rates among the samples, we measured the enthalpy of evaporation for the samples (after completing 12 h of water adsorption at 90% R.H.) using Differential Scanning Calorimetry (DSC). The enthalpy of evaporation represents the energy required to evaporate 1kg of water from hydrogel samples, thus revealing the different amounts of heat required for desorption. The water in hydrogels consists of free water, intermediate water, and bound water[174]. The interaction between free water and polymer chains is negligible, while intermediate water molecules are connected to the polymer chains via Van der Waals force, dipole-dipole force, and hydrogen bond[175]. Bound water forms stable crystalline structures with the material. Intermediate water evaporates below 100°C, whereas bound water requires higher energy.

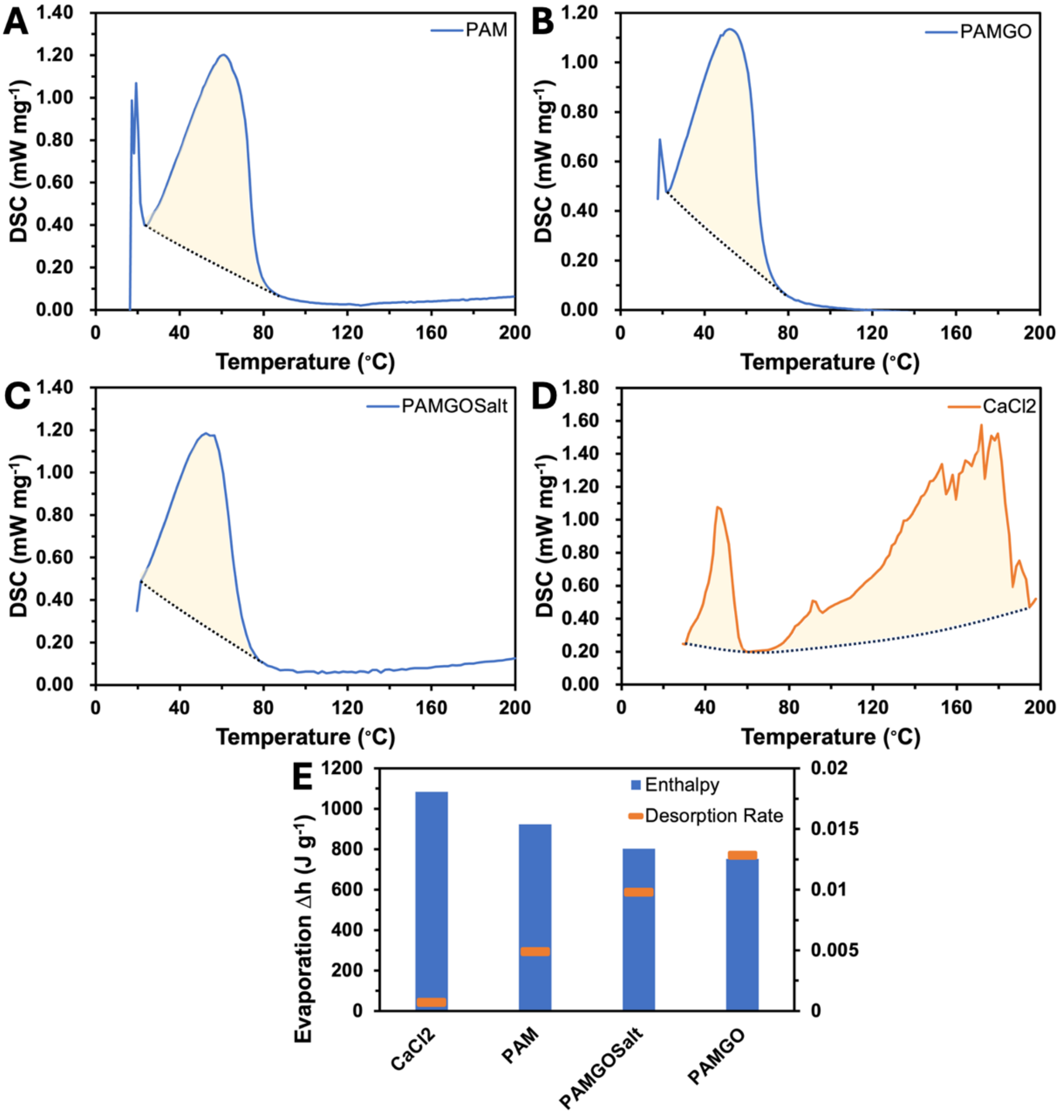

Figure 4.6 (A-C) DSC plot of PAM, PAMGO, PAMGOSalt hydrogels from 25 °C to 200 °C,

respectively. (D) DSC plot of $CaCl_2$ sample from 25 °C to 200 °C, respectively. (E) Evaporation enthalpy and desorption rate comparison.

As shown in **Figures 4.6A-B**, the enthalpy of evaporation curves for PAM and PAMGO approach zero at 100°C. PAMGOSalt continued to absorb heat above 100°C, suggesting that some water molecules formed stable bound water (**Figure 4.6C**). The enthalpy of evaporation curve of $CaCl_2$ shows that there is a continuous evaporation of water of crystallization at temperature above 100 °C. The amount of water of crystallization is over seven times that of free water (**Figure 4.6D**).

Interestingly, when comparing the data of the three PAM-based AWH samples, we found a clear positive correlation between the enthalpy of evaporation and the initial desorption rate. The sample requiring the least amount of energy to evaporate free and intermediate water (PAMGO) had the highest initial evaporation rate (0.013 g min^{-1}). Conversely, the initial evaporation rate of PAM with the highest evaporation enthalpy was only 0.005 g min^{-1}. This suggests that the relative value of enthalpy of evaporation can be used as a qualitative indicator of the initial evaporation rate of AWH hydrogels (**Figure 4.6E**).

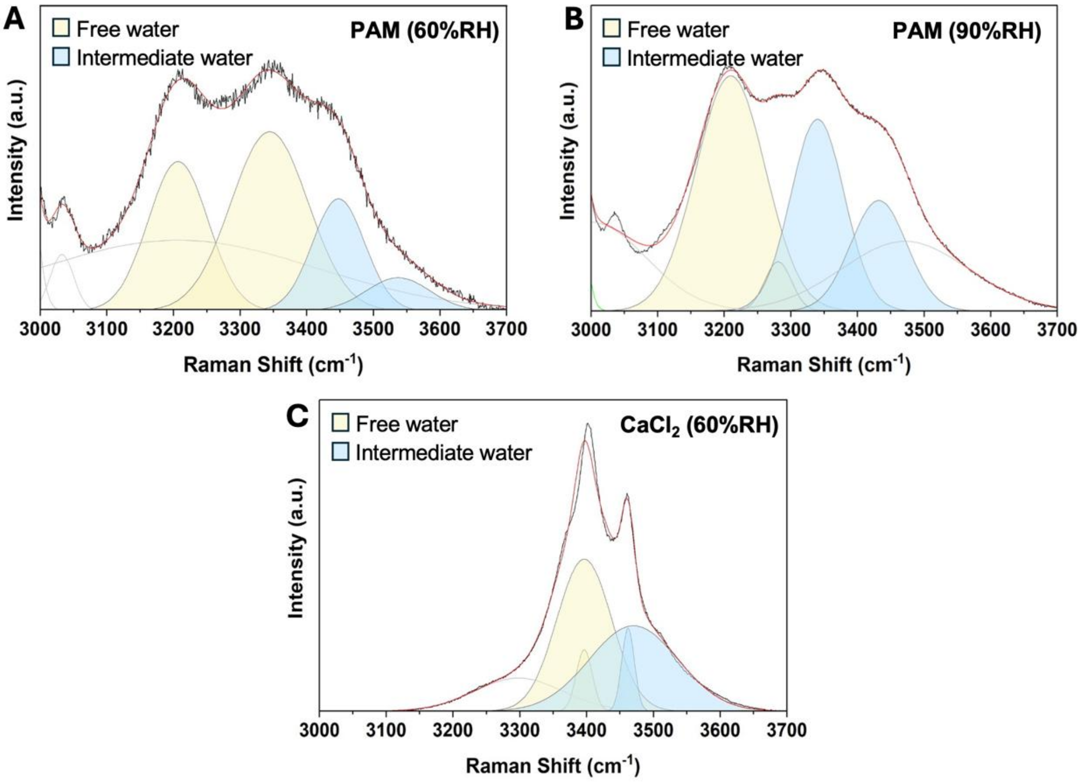

Figure 4.7 (A) Water peak fitting for PAM hydrogel that completed static water adsorption under 60%R.H. environment. (B) Water peak fitting for PAM hydrogel that completed static water adsorption under 90%R.H. environment. (C) Water peak fitting for $CaCl_2$ that completed static water adsorption under 60%R.H. environment.

Using Raman spectroscopy, we conducted a more detailed differentiation of free water and intermediate water in all the AWH samples that do not contain photothermal materials (PTMs). Free water presents two peaks in the Raman spectra, typically appearing at 3233 cm^{-1} and 3401 cm^{-1}. Intermediate water, on the other hand, has two characteristic peaks at 3514 cm^{-1} and 3630 cm^{-1}[176-177]. These peak positions may shift depending on the properties of the sample, and in hydrogel samples, they often appear as a quadruple peak. Therefore, multiple-peak fitting techniques are required to separate them.

In **Figure 4.7**, we represent the integral area of free water with light yellow and intermediate water with light blue. We found that as the water adsorption capacity increased (from 60%R.H. to 90%R.H.), the ratio of intermediate water to free water ([IW]:[FW]) rose from 35.15% to 93.2% (**Figures 4.7A, B**). Since the water adsorption curve of the hydrogel did not reach a plateau at 12 h under 90%R.H., we have reason to believe that the free water liquefied inside the hydrogel gradually wets the polymer network and forms increasing intermolecular interactions with the functional groups on the polymer chains. These interactions, along with the types of functional groups, determine the enthalpy of evaporation, which in turn affects the initial desorption rate.

For $CaCl_2$, the Raman spectrum didn’t show its its high proportion of water of crystallization, which requires more energy for water desorption, and more residual water cannot be collected at the temperatures achievable with solar irradiation (**Figure 4.7C**).

4.3.3 Conclusion

In this study, we measured the enthalpy of evaporation of AWH materials using DSC and found a positive correlation between the enthalpy of evaporation and their initial desorption rates, indicating that the enthalpy of evaporation can qualitatively predict the relative desorption rates between AWH hydrogels. Additionally, we used Raman spectroscopy to differentiate the proportions of free water and intermediate water in representative AWH materials (PAM hydrogel, and $CaCl_2$) to explain the thermodynamics and kinetics of their desorption processes. This research provides a comprehensive exploration of the water desorption mechanisms of representative AWH materials and offers valuable insights for the develop of future AWH materials.

Chapter 5 Janus Hydrogel: High-Efficiency Water Adsorption Polymer Material Achieved Through a Divide-and-Conquer Approach for Component and Function Independence

Related publication:

Feng, A., Onggowarsito, C., Mao, S., Qiao, G. G., & Fu, Q. (2023). Divide and Conquer: A Novel Dual-Layered Hydrogel for Atmospheric Moisture Harvesting. *ChemSusChem*, 16(14), e202300137.

This chapter presents an innovative dual-layered hydrogel system aimed at improving atmospheric water harvesting (AWH) efficiency. The study highlights the hydrogel's unique structural design, with separate layers for moisture adsorption and captured water release, which significantly improve its performance. This chapter explores the functionality of dual-layered hydrogels, thoroughly examining the potential challenges associated with large-scale applications, including durability and environmental impact.

5.1 Introduction

Freshwater is one of the most essential parts of human life since the origination of human being. On earth, there are 1.46×10^{16} tons of water exist, where less than 0.03% (various surface freshwater) can be currently used by human being.[178] Of the surface freshwater, ca. 3% (1.31×10^{11} tons) is stored in the atmosphere, however there are limited methods to effectively collect this freshwater.[123, 132] Water in the atmosphere exists in two forms: water vapor (unsaturated water in the form of molecules) and fog or cloud (saturated water in the form of small droplets). People have a long history of producing freshwater through proactive dew water harvesting methods that use chemical coolants and/or consume electricity (ca. 0.75 kWh per kilogram of liquid water)[179]. But this energy-intensive method is not suitable for rural areas.

Inspired from desiccant and dehumidifier, scientists have recently developed water harvesting materials,[86, 179] such as hygroscopic chemicals, metal oxides, metal organic frameworks (MOFs), hydrogels, and composite materials composed of two or more of the aforementioned materials. These AWH materials are capable of adsorbing unsaturated atmospheric water at night when the temperature is low and the relative humidity (R.H.) is high and then releasing liquid water during the daytime. For instance, hygroscopic chemicals (e.g., calcium chloride, lithium chloride) are considered potential materials due to their high polarity and the ability to form hydrate with water molecules.[90] However, the released water could be contaminated if the halogen or hydroxide ions are leached.[180-181] As an alternative solution, customized hydrogels have proven to have greater water adsorption capacity, high swelling ratio and easier/faster water release compared with other AWH materials. However, it has been noted that for hydrogel systems, there are often trade-offs between water adsorption capacity and water release efficiency, and/or photothermal conversion efficiency and mechanical properties. For example, introducing metal-organic frameworks (MOFs) into PNIPAM hydrogel leads to an improved capture capacity of 3 g g^{-1} within 12 h compared to the bare counterparts due to the highly porous structure of MOFs for water storage[182]. However, the captured water is trapped in the pores of MOFs, resulting in a high proportion of retention water. Yu et al. reported a PNIPAM hydrogel that incorporated chloride-doped polypyrrole (PPy-Cl) as photo-thermal material (PTM) and auxiliary adsorbent. This hydrogel surprisingly achieved a water adsorption capacity of 6.2 g g^{-1}, and 50% of the captured water in the hydrogel can be self-released within 20 min under sunlight irradiation[183]. However, the delocalization of H^+ and Cl^- leads to response attenuation of PNIPAM hydrogel, resulting in an increasingly slower rate of water release. In another case, lithium chloride and reduced graphene oxide (rGO) were mixed with polyvinyl alcohol (PVA) and the resultant hydrogel showed a water adsorption capacity of 2.25 g g^{-1}. The incorporation of rGO improved the mechanical property of the hydrogel as the expense of water adsorption capacity.[73, 94, 114] We thus saw this as an opportunity to develop a novel dual-layered hydrogel (DLH) system with independent functions, one layer for water adsorption and storage, and the other for efficient, sunlight-assisted water release, to address the trade-offs.

In this work, we adopted a novel design strategy to prepare a DLH consisting of a light-to-heat conversion layer (LHL) and a water adsorption layer (WAL) to achieve stimuli-responsive water release and improved adsorption capacity simultaneously. The LHL was prepared by incorporating novel polydopamine-manganese(II) nanoparticles (PDA-Mn NPs) into PNIPAM matrix, and the WAL was prepared by copolymerizing NIPAM (<25 wt%) and (2-(acryloyloxyethyl) trimethylammonium chloride) (AEtMA, 75 wt%). In humidity environment, the resultant DLH can effectively adsorb the moisture in the air and achieve a high water adsorption capacity of 7.73 g g^{-1}. Of particular note, at low temperature the LHL layer can also absorb and store water in the PNIPAN matrix as well as the pores of PDA-Mn NPs. Under sunlight exposure, 50% of captured water was released within 1 h, and almost 100% adsorbed water can be released within 4 h.

5.2 Experimental section

5.2.1 Material and chemical synthesis procedure

N,N′-Methylenebis(acrylamide) (BIS, 99%, Sigma-Aldrich), *N*-isopropylacrylamide (NIPAM, 97%, Sigma-Aldrich), [2-(acryloyloxy)ethyl]trimethylammonium chloride solution (AEtMA, 80 wt% in H2O, Sigma-Aldrich), *N,N,N′,N′*-tetramethylethylenediamine (TEMED, 99%, Sigma-Aldrich), ammonium persulfate (APS, 98%, Sigma-Aldrich), potassium permanganate ($KMnO_4$, 99%, Sigma-Aldrich), potassium sulphate (K_2SO_4, AR, Ajax Finechem Pty Ltd), dopamine hydrochloride (DA, 98%, Sigma-Aldrich), sodium hydroxide (NaOH, 98%, Sigma-Aldrich), sodium bromide (NaBr, 99%, Sigma-Aldrich), and magnesium chloride ($MgCl_2$, 98%, Sigma-Aldrich) were used as received without further purification. Deionized water (DI water) was obtained by Milli-Q water purification system (18.2MΩ.cm @25°C). Dialysis tube (SnakeSkinTM, MWCO=3500) was purchased from Thermo Scientific.

In a typical synthesis of PDA-Mn/Fe NPs, 0.3064 g dopamine hydrochloride was dissolved in 185 mL DI water. Then, 1M sodium hydroxide was dropwise added into the dopamine solution until the pH of the mixture reached 9 (solution A). This flask was then transferred to ultrasonication for preparation. Dissolving 0.1054 g potassium permanganate (or 0.0973 g iron(III) chloride) in 15 mL DI water (solution B). Once the ultrasonication started, slowly mixed the as-prepared solution B with solution A. The flask was exposed to air for oxygen supply, and the reaction processed for 6 h under sonication at ambient condition (i.e., 1 atm, 22 °C). To purify the obtained NPs, the reaction mixture was dialyzed against DI water using a dialysis Tube (MWCO = 3500 Da) until the color of DI water was clear and transparent. The resultant NPs was then centrifuged and dried at 60 °C in a drying oven for 24 h.

For a typical synthesis of the dual-layered hydrogel (LHL:WAL=1:3 wt/wt), 0.0567 g NIPAM, 0.003 g BIS (crosslinker), and 0.009 g PDA-Mn NPs (photothermal material, PTM) were mixed and dissolved in 1 mL DI water under sonication (solution C). 0.0428 g NIPAM, 0.009 g BIS (crosslinker), and 128 μL AEtMA (80 wt% in water) were mixed and dissolved in 3 mL DI water under sonication (solution D). Then, 3 and 9 μL TEMED were added into solution C and D, respectively. To start the gelation, 50 μL APS solution (0.53 M) was added into solution C to induce polymerization at room temperature. After gelation of LHL, 150 μL APS solution (0.53 M) was added into solution D, and the mixture was poured on the surface of LHL immediately. The polymerization of WAL was carried out for 2 h at room temperature. The as-prepared DLH was soaked in DI water for 3 h to remove unreacted residue and freeze-dried for 12 h before vapor adsorption tests.

5.2.2 Characterizations

UV-VIS-NIR spectra were recorded on a SHIMADZU UV-1700 UV-Visible spectrophotometer.

Fourier-transform infrared spectroscopy (FT-IR) spectra was obtained using a SHIMADZU MIRacle 10 single reflection ATR accessory.

Scanning electron microscope (SEM) images were obtained by Zeiss EVO LS15 SEM system.

Infrared thermometer images were captured using FLUKE PTi120 thermal imager.

Sunlight simulation light source was obtained from Beijing NBeT HSX-F300 xenon light source.

Dynamic light scattering (DLS) data were recorded using a MALVERN Instruments Zetasizer Nano series system.

Inductivity coupled plasma mass spectrometry (ICP-MS) characterization was conducted using an Agilent Technologies 7900 ICP-MS system with SPS-4 Autosampler.

5.2.3 Moisture adsorption experiments

The moisture adsorption tests were conducted under 3 L min^{-1} air flow with different relative humidity (R.H.%). Dried compressed air was blowed to supersaturated salt solution, then the humidified air flows to the surface of WAL of the hydrogel. The R.H. of the air flow were stabilized using potassium sulphate (R.H.= 95%), potassium chloride (R.H. = 90%), sodium bromide (R.H. = 60%) and magnesium chloride (R.H. = 30%)[184]. As shown in **Figure 5.1A**, in a 500 mL flat bottom flask, 25 g potassium sulphate was dissolved in 200 mL DI-water. The pipe that flowed dried compressed air was immersed under the level of the supersaturated potassium sulphate solution. Wet air was blown to a container that held the hydrogel. The relative humidity of the gas flow through the saturated salt solution were recorded by a humidity meter (testo-635). We found that the recorded values are close to the theoretical values. During the water adsorption process, DLH was placed in a cylindrical plastic container with a diameter of 4.5 cm and a height of 5 cm without contacting the bottom and sides of the container (the WAL surface was in contact with the air, while the LHL surface was in contact with the hydrophobic support material).The 3/4 height of the container is placed in an ice-water bath, and humid air is blown from the top of the container and cooled down to 5 °C in the container to simulate the low temperature environment at night. The temperature profile of humid air was provided in **Figure 5.1B**. To prevent the absorption of condensed liquid water, hydrogel in the container was held on a shelf that prevents the hydrogel contacting with the bottom of the container. The mass of the hydrogel was recorded and the condensed liquid water in the container was removed every 30 min.

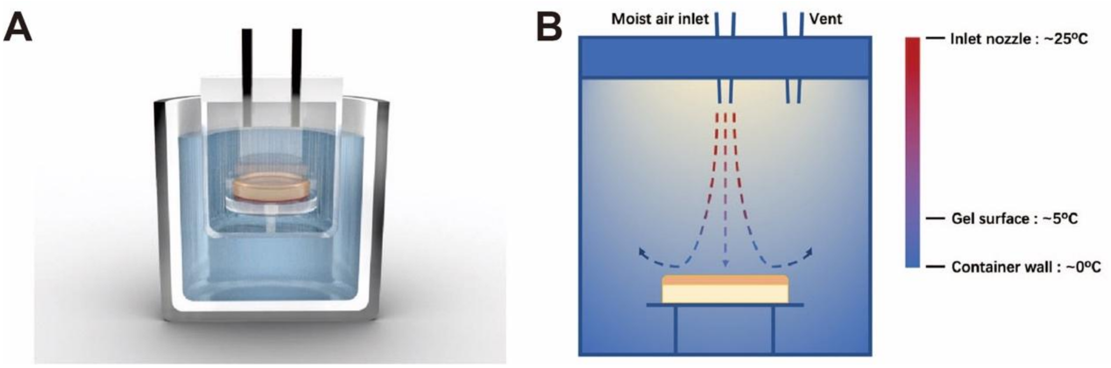

Figure 5.1 (A) The diagram of the water adsorption set-up. (B) Temperature profile of humid airflow inside the water adsorption container (simple CFD illustration).

5.2.4 Sunlight-assisted autonomous water release

The in-door sunlight simulation experiment was conducted using a XE300WUV Xenon light source (Beijing NBeT Technology Ltd) to simulate sunlight. The irradiation intensity was stabilized at 1 kW m^{-2} (1.0 sun equivalent). The mass of hydrogel was monitored using an analytical balance with internal calibration (OHAUS Pioneer® analytical balance) every 15 min. The surface temperature of the hydrogel was recorded by IR camera (FLUKE PTi120 thermal imager).

5.2.5 Durability test

The durability of the dual-layered hydrogel was determined at 95% R.H. for 10 cycles (for each cycle, we performed water adsorption for 8 h, followed by 4 h indoor simulated sunlight irradiation). At the end of each cycle, the hydrogel was further irradiated for 1 h to remove any potential water residue. The hydrogel was placed with WAL upward during water adsorption, and LHL upward during sunlight irradiation.

5.3 Results and discussion

5.3.1 Structure and morphology of hydrogel and PDA-NPs

To improve the water adsorption of hydrogel-based AWH materials while achieving. stimulus release of water, we adopt the ‘divide and conquer’ strategy to prepare a novel functionally independent DLH. We first considered the use of dopamine-iron(III) (PDA-Fe) NP as PTM to construct LHL because it is cheap and easy to synthesize. However, recent study has shown that Mn(VII) ions can accelerate the redox cycle of dopamine by an order of magnitude compared Fe, Cu, Zn, and Co at micromolar concentrations.[185] We were curious whether the high degree of polymerization of polydopamine could lead to different photothermal properties. In this study, we synthesized a novel PDA-Mn NP and compared its photo-thermal conversion performance with that of PDA-Fe NP (**Figure 5.2A**).[186] It is found that the prepared PDA-Mn NPs have a diameter of 150-200 nm (**Figure 5.2B** and **Figure 5.3B**) and can be homogeneously dispersed in aqueous media. While at low pH < 4, the PDA-Mn NPs tend to form aggregations. We further conducted energy dispersive X-ray (EDX) analysis of the PDA-Mn NPs (**Figure 5.2C**). Except C, N and O elements, we observed two characteristic peaks belonging to manganese at 655 and 790 eV. In contrast, the PDA-Fe NPs have a larger diameter of 500 nm (**Figure 5.3A**).

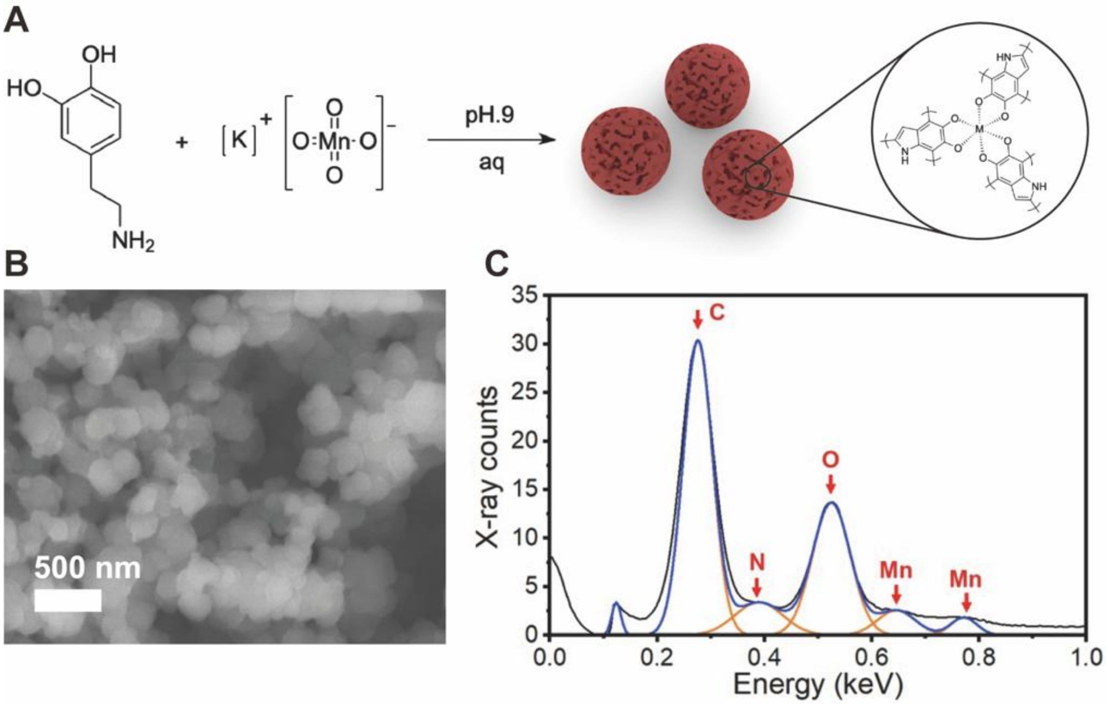

Figure 5.2 (A) The synthesis of polydopamine-(Mn) nanoparticles (PDA-Mn NPs). (B) SEM images of PDA-Mn NPs. (C) Energy dispersive x-ray (EDX) analysis result for element identification using multiple peaks fitting (Black: original EDX data; Blue: accumulative curve from fitted peaks; Orange: carbon, nitrogen, oxygen, and manganese peak).

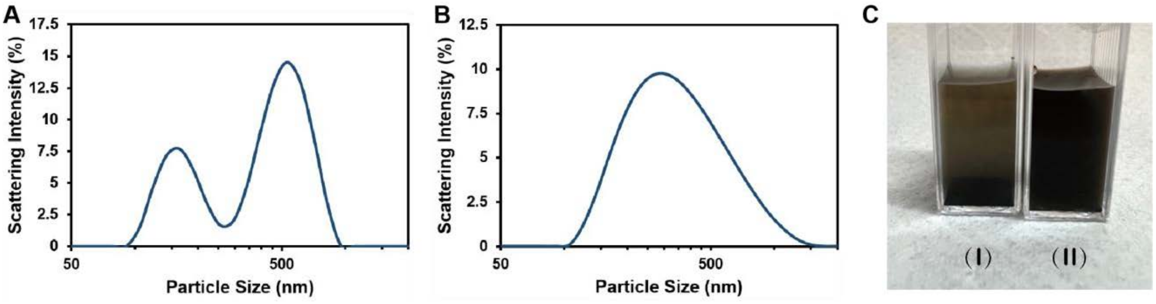

Figure 5.3 Digital Light Scattering (DLS) particle size analysis result measured by intensity. A: PDA-Fe NPs; B: PDA-Mn NPs; C(I): PDA-Fe NPs; C(II): PDA-Mn NPs.

We then prepared a series of LHLs consisting of PNIPAM matrix and PDA-Mn NPs PTM (or PDA-Fe NPs as a control sample) via radical polymerization at room temperature according to previous report[183] (**Scheme 5.1**). As expected, the resultant LHLs containing 5-10 wt% NPs displayed stronger solar absorption ability compared to the bare sample (0 wt%) in all UV-VIS-NIR ranges (250-2000 nm). Of particular note, further increasing the loading of PDA-Mn NPs leads to aggregation of NPs, and the resulting LHL showed incremental photothermal response. We then evaluated their photothermal converting ability. As shown in **Figure 5.4B**, the bare sample without NPs showed a consistent temperature of 25 °C after 1 h of sunlight irradiation (1.0 sun equivalent). The LHL containing PDA-Fe NPs reached ca. 30 °C after 1 h irradiation and maintained this temperature. This may be attributed to the severe aggregation of PDA-(Fe) NPs in PNIPAM matrix, resulting in low conversion efficiency. In contrast, the temperature of the LHL with PDA-Mn NPs increased from room temperature to

33 °C within 1 h and continued to rise to 45.4 °C in the next 3 h. These results indicate that the uniformly dispersed PDA-Mn NPs are more effective to the absorption and conversion of sunlight into heat. The structure of PNIPAM-based LHL was further characterized by FTIR spectroscopy (**Figure 5.4C**). We observed the characteristic peaks at 1,650 and 3,300 cm^{-1}, which can be attributed to the C=O stretching and N-H stretching of PNIPAM, respectively.

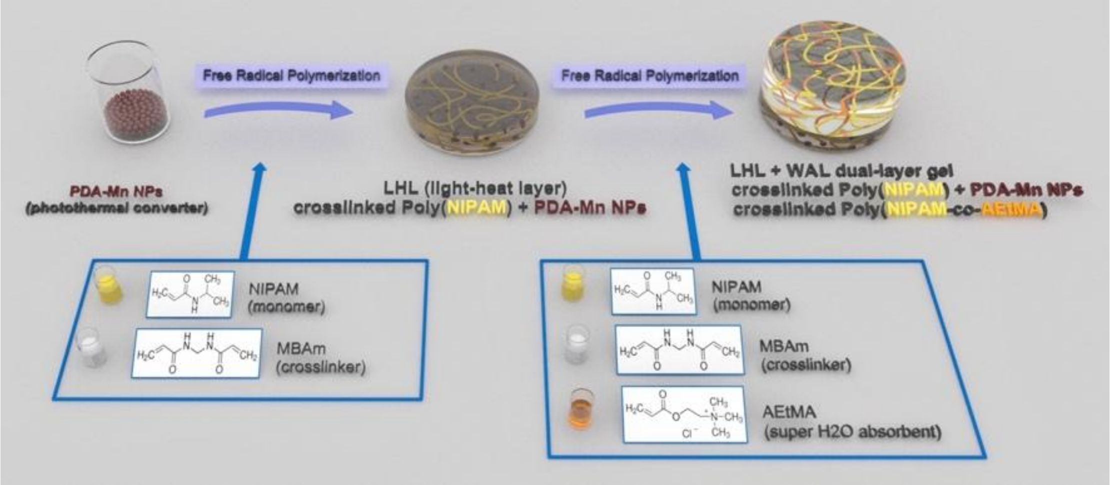

Scheme 5.1 Schematic illustration of the synthesis of dual-layered composite hydrogel.

Previous study have demonstrated that the PNIPAM-based, monolayer hydrogel system usually has an insufficient moisture adsorption capacity at unsaturated environment.[183] To address this issue, we further synthesized a polyelectrolyte-based WAL to enhance water capture and storage. Polyelectrolytes are polymers possessing ionizable groups[96] and have been widely used in the treatments of wastewater, ceramic slurries, and concrete mixtures[187-191]. Due to their super-hydrophilic ionizable groups, polyelectrolyte-based hydrogels show an unusual high swelling ratio of >100 g g^{-1}.[192] In this study, an aqueous mixture containing monomers ([NIPAM]/[AEtMA] = 1/3) and crosslinker was poured on the prepared LHL, and the WAL was prepared via radical copolymerization (**Scheme 5.1**). The resulting DLHs were then frozen at -20 °C and thawed in DI water to remove unreacted residue, followed by frozen-drying. The WAL is composed of 75 wt% PAEtMA, leading to an exceptional affinity for water molecules due to the strong polarity of quaternary ammonium-chloride groups of AEtMA. While the remaining ca. 25 wt% PNIPAM component can enhance the compatibility between WAL and LHL. To demonstrate the high water affinity of the WAL, we prepared a control sample with the same composition (i.e. AEtMA:NIPAM = 3:1 wt/wt) and tested its water uptake capacity. As expected, this sample had a maximum water uptake capacity of 131.75 g of water per gram of dry gel (**Figure 5.5**). This result is much higher than that of the PNIPAM-based hydrogels[183].

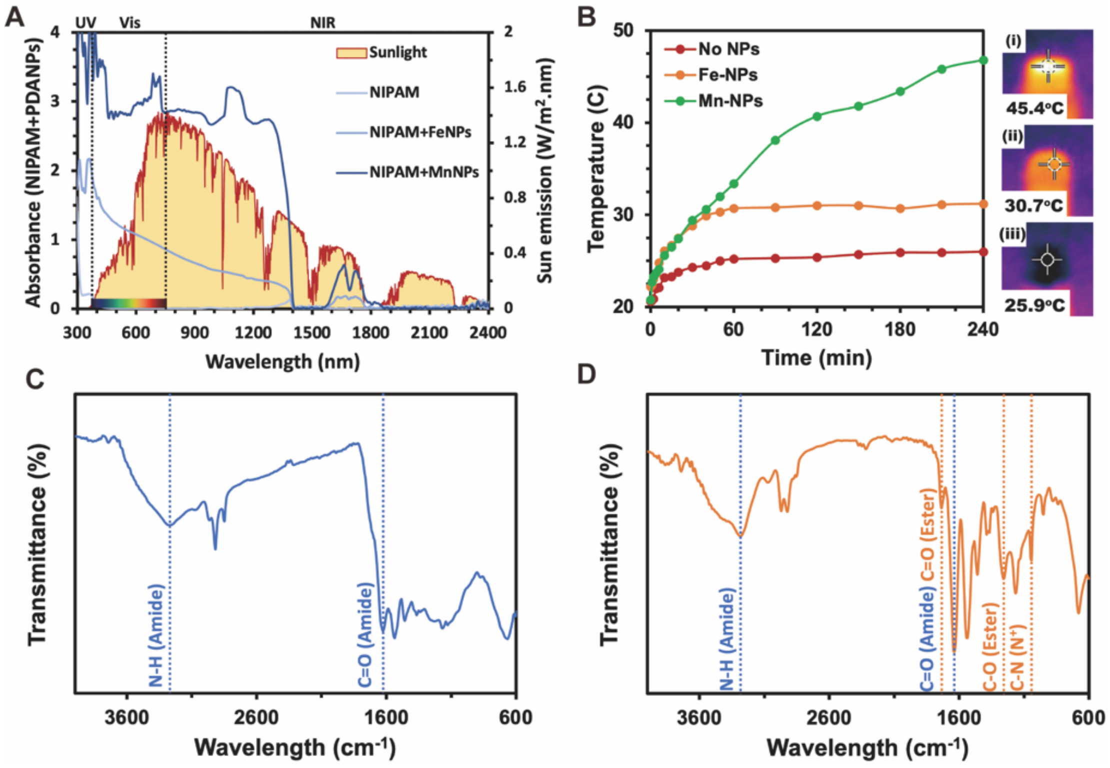

Figure 5.4 (A) Absorption spectra of LHLs vs. sunlight emission spectrum. (B) Temperature profiles of the prepared LHLs (1 cm × 1 cm × 1 cm) with or without NPs under 1.0 sun

irradiation for 4 h: (a) without NPs, (b) with PDA-Fe NPs and (c) with PDA-Mn NPs. (C) FT-IR spectrum of LHL. (D) FT-IR spectrum of WAL.

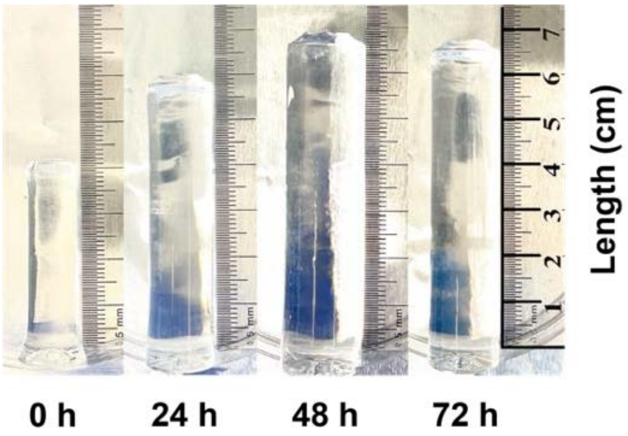

Figure 5.5 Size-time plots of poly(AEtMA-co-NIPAM) gel submerged in DI water in 3 days.

The surface (both the LHL and the WAL surfaces) and the cross-sectional morphologies the DLH were measured by SEM images (**Figure 5.6A-F**). The SEM images (**Figure 5.6A&5.6B**, and **5.6D&5.6E**) confirm that both layers have a highly porous structure and hence high surface area. In addition, the PNIPAM/PAEtMA-based WAL has a 'thicker wall' and larger pore size in comparison with the PNIPAM/NPs-based LHL. This result may be attributed to the lower glass transition temperature ($T_g < 20$ °C) of PAEtMA, resulting in a 'slower' solidification process in the freezing dry.[193] We also observed a clear boundary between the two layers (**Figure 5.6C**) and the connection is stable without sign of detachment. This result proves the successful preparation of the DLH, a rarely reported AWH material. When we zoomed in to the SEM image of LHL, we clearly observed the PDA-Mn NPs embedded into the PNIPAM 'wall' (**Figure 5.6F**). This is in good agreement with the EDX mapping result (**Figure 5.7A&B**). The vertical pores on hydrogel surface provides adequate adsorption area for water molecules as well as transport channels for liquid water. Moreover, the highly porous structure of LHL will also facilitate the fast water release via evaporation. The structure of PNIPAM/PAEtMA-based WAL is also characterized by FTIR spectroscopy (**Figure 5.4D**). Two new peaks at 1,250 and 1,700 cm^{-1} were observed, which can be attributed to the vibration of C-O and C=O of PAEtMA, respectively. The apparent peak at 1,000 cm^{-1} indicates the presence of quaternary ammonium groups,[194] that have strong electrostatic forces with water molecules in the atmosphere.

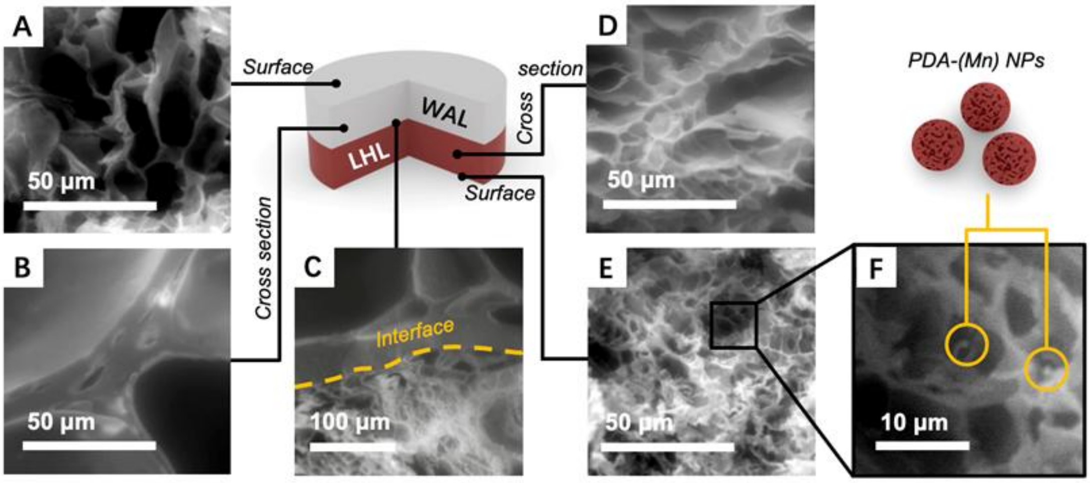

Figure 5.6 SEM images of the dry dual-layered hydrogel.

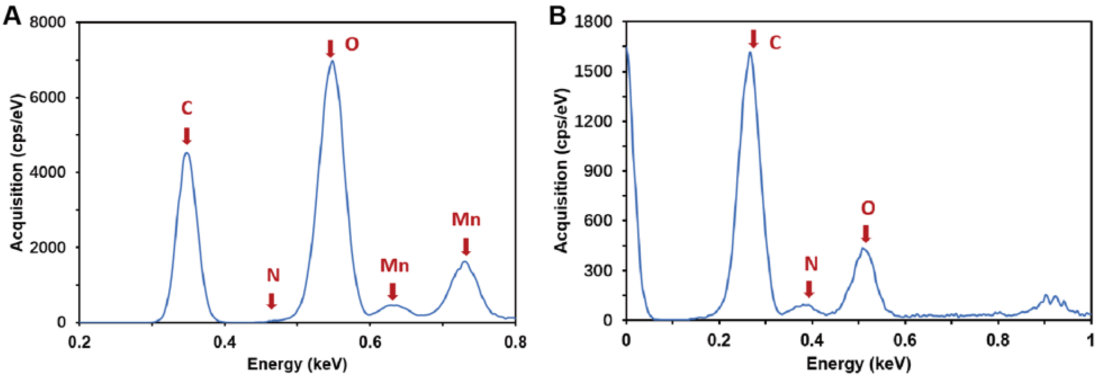

Figure 5.7 (A) Energy Dispersive X-ray Analysis (EDX) result of element identification for

LHL layer hydrogel. (B) Energy Dispersive X-ray Analysis (EDX) result of element identification for WAL layer hydrogel.

5.3.2 Water adsorption and desorption performance

To validate the concept of ‘divide and conquer’ strategy, we first compared the water capture and release performance of the DLHs with a monolayer counterpart which contains the same compositions. The control sample was prepared by simply mixing the same amount of NIPAM, AEtMA, crosslinker and PDA-Mn NPs, followed by copolymerization and freeze-thaw under the same conditions. Both the DLH and the control sample were placed in a sealed plastic container to prevent condensed water contact. The container was cooled down and a moisture airflow with constant R.H. was supplied by passing compressed dry air through saturated salt solutions[183]. The DLH adsorbed water up to ca. 2.5 g g^{-1} at >90 % R.H., which is ca. 60% higher than that of the control sample (**Figure 5.8**). This result can be attributed to the formation of random copolymer networks of NIPAM and AEtMA in the monolayer gel, disrupting the long-range continuity of more hydrophilic PAEtMA segments. Once the WAL was saturated, the water adsorbed can be transferred to the LHL by capillary force. In the LHL, the porous PDA-Mn NPs with a large number of phenolic hydroxyl groups offer high water affinity and additional storage space. The water adsorbed into the DLH can be released under sunlight irradiation by evaporation. Specifically, PDA-Mn NPs in LHL can convert electromagnetic waves into thermal energy to heat the hydrogel. In this study, the LHL can reach more than 45 °C under simulated sunlight exposure within 4 h, promoting rapid evaporation of water molecules stored in the DLH. In the following evaporation tests, we found that the evaporation rate of the control sample is 0.125 g g^{-1} min^{-1}, which is slightly higher than that of DLH (0.1 g g^{-1} min^{-1}). This result can be attributed to the higher heat conductivity of the monolayer gel. In short, these results indicate that besides the chemical composition, the hydrogel architecture also plays an important role in the water adsorption and release performance. In the plastic container, the surface of the hydrogel is close to 5 °C and the temperature of the inner wall is close to 0 °C. As shown in **Figure 5.1B**, the temperature of the vapor in the container drops sharply on the surface of the hydrogel, thus crossing the dew point and condensing into water. The water vapor in the remaining space remains in the gas phase.

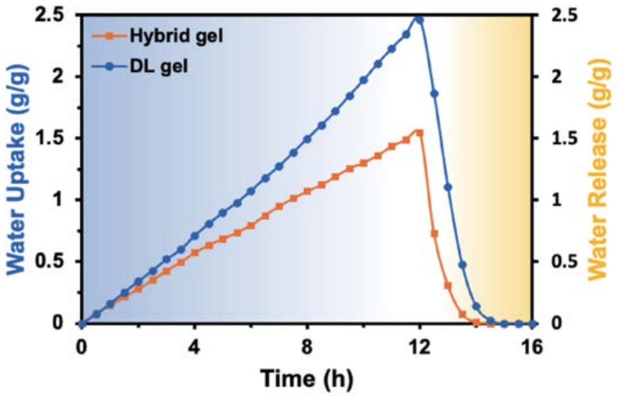

Figure 5.8 In-door moisture capture simulation between hybrid and dual-layered hydrogel at 95% RH. LHL:WAL=1:1 for dual-layered hydrogel.

In the DLH, the WAL has a higher water adsorption capacity than the LHL, leading to a huge shear force at the interface, which may trigger layer detachment and even tear the WAL. We thus optimized the composition of DLH by tuning the mass loading of

PDA-Mn NPs, the composition of WAL and the weight ratio of LHL and WAL. **Figure 5.9A** illustrates the moisture adsorption and water release performance of a series of DLHs containing 0, 5, 10, and 15 wt% PDA-Mn NPs in the LHL. Increasing mass loadings of PDA-Mn NPs brings an improved moisture capture capacity by ca. 80 % during a continuous 12 h experiment. In the subsequent simulated evaporation/release process, the DLHs can release 50% of captured water within 1 h ($t_{0.5}$ = 1 h) under sunlight irradiation (1.0 sun equivalent). It is also found that 10 wt% of PDA-Mn NPs load is the optimal amount for LHL. Because further increasing PDA-Mn NPs loading to 15 wt% led to aggregation of NPs, and thus has a negligible effect on water evaporation rate.

During the moisture adsorption process, water molecules first collide with the WAL surface, and the density of the quaternary ammonium salt determines its water affinity. Therefore, we optimized the moisture adsorption capacity of the DLH by judicious adjusting the composition of the WAL. We fixed the volume ratio of LHL/WAL = 1/1 and the PDA-Mn NPs content of 10 wt% in the LHL, and then prepared a series of DLHs with different NIPAM/AEtMA weight ratio of 4:0, 3:1, 2:2 and 1:3. Of particular note, further increasing AEtMA content to 100 wt% led to a poor compatibility towards PNIPAM-based LHL. **Figure 5.9B** illustrates the moisture capture and water release performance of these DLHs. Due to the strong water affinity of quaternary ammonium cations, the low moisture density close to the surface creates a humidity gradient that becomes the main driving force for moisture capture. Thus, with the increase of AEtMA content from 0 to 75 wt% (1:3), the moisture capture capacity of the resulting DLHs increased by 110%. Again, this result indicates that PAEtMA has a significantly larger moisture-adsorbing ability compared with PNIPAM. Interestingly, all the prepared DLHs can release 50 wt% captured water within 1 h under sunlight exposure, suggesting efficient water transport from WAL to LHL. This is also proved in the stable gradient region detailed in **Figure 5.10**.

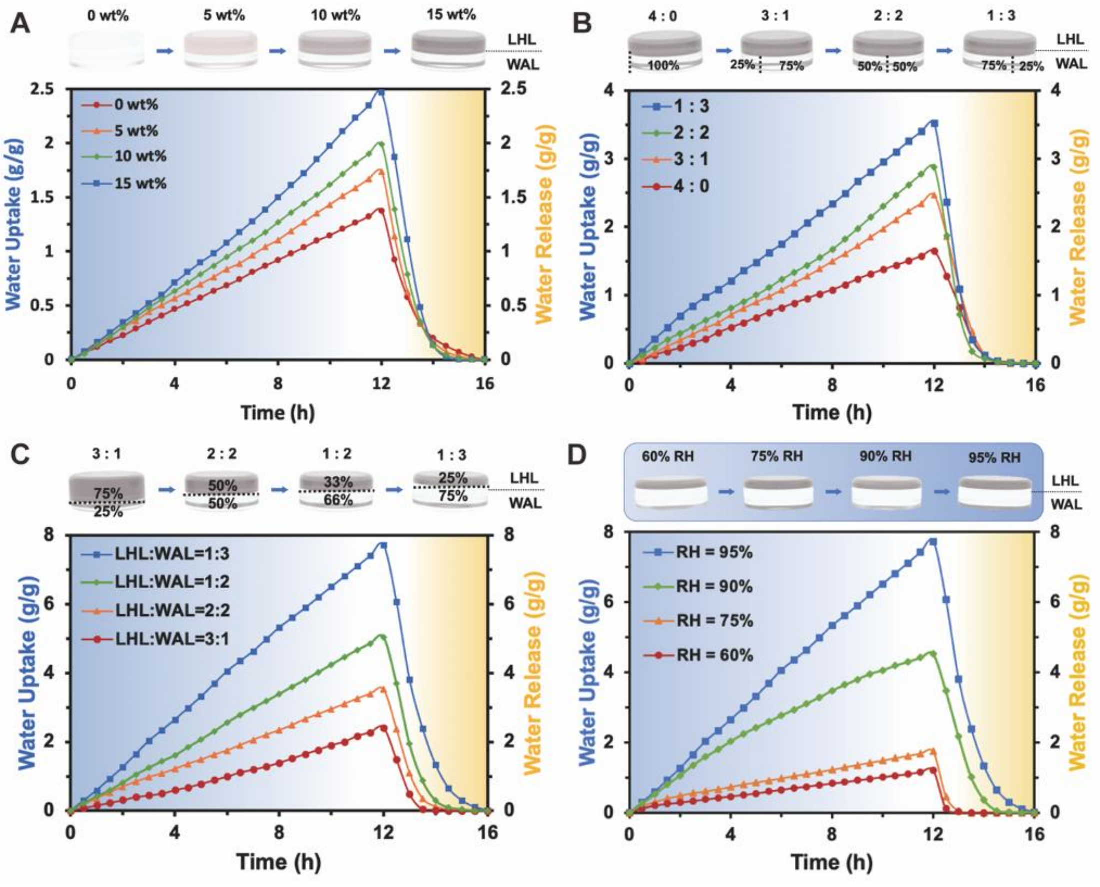

Figure 5.9 (A) In-door moisture capture simulation using dual-layered hydrogel with 0, 5, 10, and 15 wt% PDA-MN NPs under 1.0 sun irradiation (LHL:WAL=1:1). (B) In-door moisture capture simulation using dual-layered hydrogel with 4:0, 3:1, 2:2, and 1:3 mass ratio between NIPAM and AEtMA at 95% RH and 5 °C. (C) In-door moisture capture simulation using dual-layered hydrogel with 1:3, 1:2, 2:2, and 3:1 v/v between LHL and WAL at 95% RH and

5 °C. (D) In-door moisture capture simulation using dual-layered hydrogel with 1:3 v/v between LHL and WAL at 60%, 75%, 90%, and 95% RH at 5 °C.

Despite the high moisture capture capacity of the WAL with 75 wt% of AEtMA, we further optimized the volume ratio of WAL to LHL to boost the overall water adsorption capacity, while maintained the ability to rapidly release water. Four DLHs with different volume ratios of LHL to WAL (LHL/WAL = 3/1, 2/2, 1/2, and 1/3, v/v) were prepared. In the water capture experiment, we found that the moisture capture capacity increased from 2.41 to 7.73 g g^{-1} when gradually increasing the WAL volume ratio (**Figure 5.9C**). Under sunlight exposure, all the DLHs showed a $t_{0.5}$ = 1 h and can release >98% of captured water in 4 h. Meanwhile, the top surface temperature of the LHL achieved 50 °C during water desorption, and the average of the DLH reached 42.5 °C (**Figure 5.11**). Under extreme conditions, such as when DLH is in direct contact with water, the LHL/WAL = 3/1 (v/v) DLH has a maximum water uptake of 18.51 g g^{-1}. While this value increases to 22.15 g g^{-1} in the case of LHL/WAL = 1/3 (v/v).

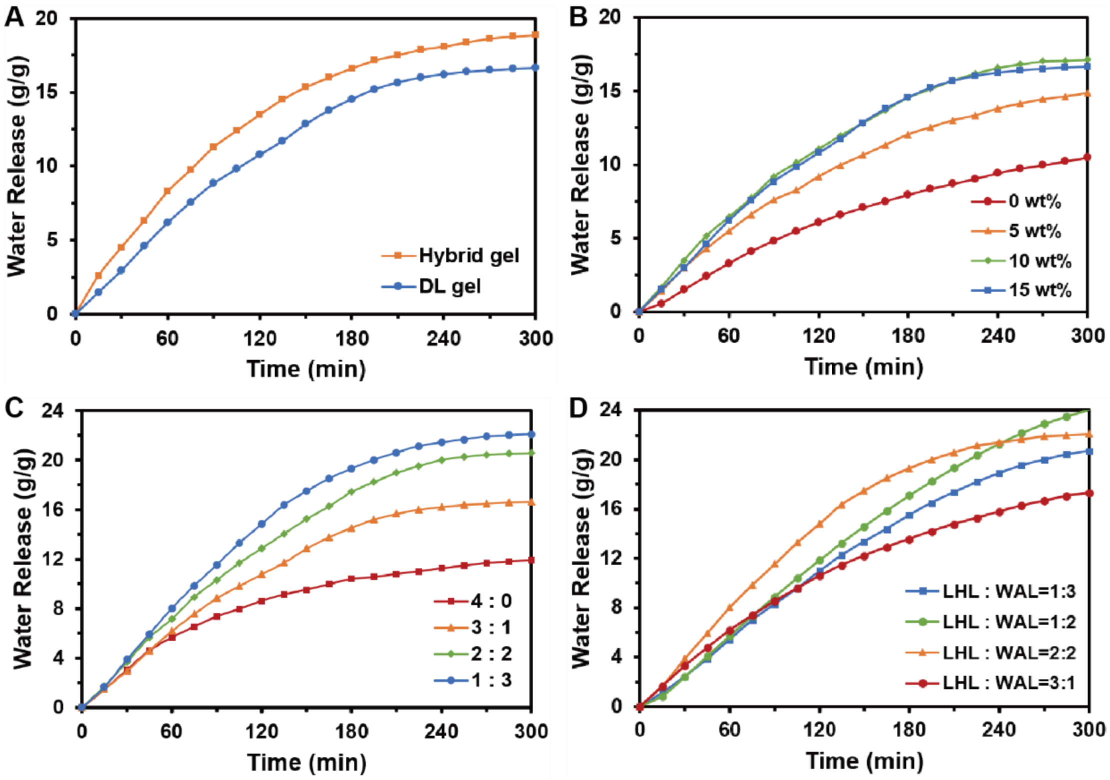

Figure 5.10 Water evaporation trends of dual-layered AWH hydrogels. (A) Hybrid gel that mixing the water adsorbent (PolyAEtMA), polyNIPAM, and PDA-(Mn) NPs together, and dual-layered hydrogel. (B) Dual-layered hydrogel with 0, 5, 10, and 15 wt% PDA-MN NPs under 1.0 sun irradiation (LHL:WAL=1:1). (C) Dual-layered hydrogel with 4:0, 3:1, 2:2, and 1:3 mass ratio between NIPAM and AEtMA at 95% RH. (D) Dual-layered hydrogel with 1:3, 1:2, 2:2, and 3:1 v/v between LHL and WAL at 95% RH.

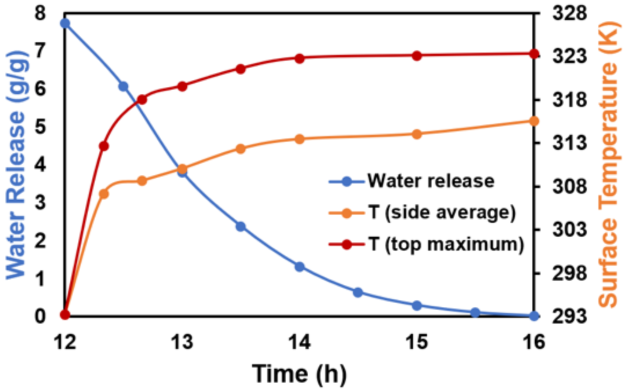

Figure 5.11 Well-Temperature-time and water desorption-time composite plot for water desorption performance evaluation.

At 5 °C, The water adsorption performance of DLH are also different under different relative humidity environments. The prepared DLH exhibited an excellent water adsorption capacity of 4.55 g g^{-1} and 7.73 g g^{-1} in 12 h under 90% and 95% R.H., respectively. While, under moderate (75% R.H.) or low (<60% R.H.) humidity conditions, the water adsorption capacity of DLH were 1.75 g g^{-1} and 1.21 g g^{-1}, respectively (**Figure 5.9D**). The water adsorption capacity of the DLH increased by 341.7% from 60% to 95% R.H. This result can be attributed to the difference in water vapor density under moderate (0.0033 g water vapor per gram of dry air) and high humidity (0.0052 g g^{-1}), resulting in insufficient water molecules to achieve passive dewing under moderate or low humidity conditions. We found that upon continuing to increase the humidity to >100% R.H. (i.e. fog), the water absorption capacity of DLH was ca. 18.1 g g^{-1} within 12 h and showed a tendency to reach equilibrium (**Figure 5.12A**). However, this value is still lower than the maximum swelling ratio of the DLH.

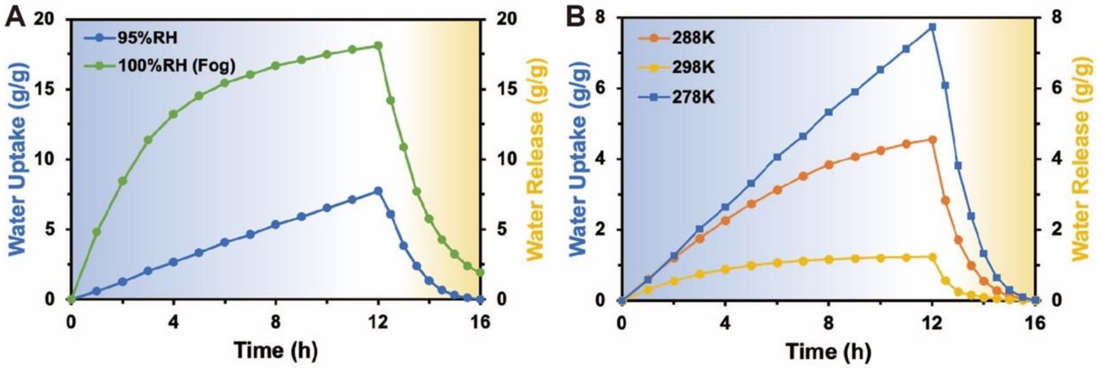

Figure 5.12 (A) In-door moisture capture simulation using DLH at 95% R.H. and >100% R.H. (fog) at 5 °C. (B) In-door AWH performance of DLH at different temperatures: 5 °C, 15 °C, and 25 °C at 95% R.H.

While when the temperature gradually increased from 5 °C to 25 °C, the water adsorption capacity of DLH decreased from 7.73 g g^{-1} to 1.24 g g^{-1} (**Figure 5.12B**). As the temperature increases, the time required for vapor to liquefy on the surface of the DLH increases. The change in adsorption mechanism was reflected in the fact that the water adsorption curve tended to approach the plateau stage, that is, gradually reached equilibrium at higher temperatures.

We further tested the static water adsorption capacity of DLH at 25 °C, 15 °C and 5 °C respectively, and compared the results with the dynamic water adsorption capacity under the same conditions. As shown in **Figure 5.13A**, at 25 °C the difference between the dynamic and static water adsorption capacity of DLH was the smallest, only 14.6%. The largest difference in water adsorption capacity (>97 %) was observed as the temperature decreased to 5 °C (**Figure 5.13C**). This is because as the temperature decreases, the absolute humidity of water vapor decreases rapidly in air with the same relative humidity. This leads to a sharp decrease in the density difference of water molecules (or vapor concentration difference) near the surface of the DLH, with a corresponding decrease in the driving force for liquefaction.

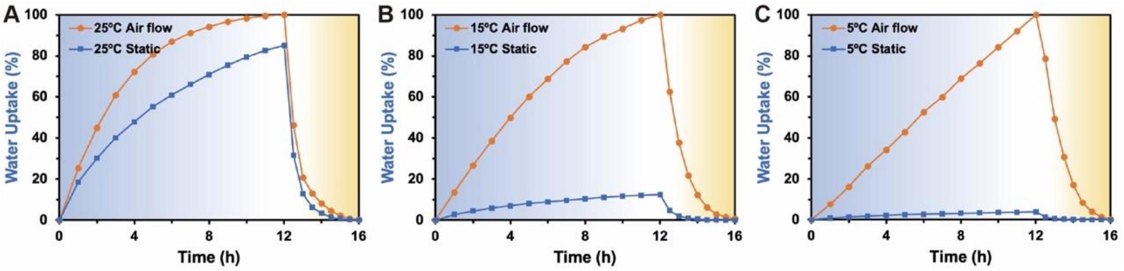

Figure 5.13 Static and dynamic water vapor adsorption of DLH at (A) 25 °C, (B) at 15 °C and (C) at 5 °C, respectively.

Due to its highly porous structure and numerous open metal sites, metal-organic frameworks (MOFs) have been incorporated into hydrogel-based AWH materials to improve water storage capacity.[63, 65, 110, 195-198] However, such hydrogels usually displayed a relatively low water release efficiency because water molecules stored in the porous MOF NPs lack the driving force to efflux.[66, 199] In contrast, we found that the water release efficiency of the DLH containing porous PDA-Mn NPs reached 98.4%, which is much higher than MOF-based AWH materials. In this study, the PDA-Mn NPs can generate heat in situ and the electrostatic attraction between the open metal sites and water molecules was then suppressed at elevated temperature, thus giving the water molecules greater kinetic energy and weakening the hydrogen bonding with PDA-Mn NPs[200-203]. In addition, the water adsorption capacity can also positively affect the evaporation rate. As shown in **Figure 5.10**, corresponding to the LHL/WAL = 3/1, 1/1, 1/2, and 1/3 (v/v) DLHs, the water evaporation rates were 0.09, 0.12, 0.1, and 0.09 g g^{-1} min^{-1}, respectively. Nevertheless, the advantage of thickening WAL is still extremely outweighing the disadvantage of thinning the LHL.

We then compared the moisture capture capacity and water releasing efficiency of the present DLH with the state-of-the-art AWH materials. As shown in **Figure 5.14**, the vast majority of AWH materials are hydrogel- and MOF-based systems. For hydrogel materials, under the optimized adsorption conditions (i.e. 80-95% R.H.), they typically exhibit high water release efficiencies (>85%), but have diverse water adsorption capacities. In the case of MOFs, they work under relatively low humidity conditions (<80% R.H.) and exhibit lower adsorption capacity and lower release efficiency. Compared with these AWH materials, the present DLH exhibits the highest water adsorption capacity of 7.73 g g^{-1} at 95% R.H. and a very high-water release efficiency of 96.7% with a moderate water release rate of $t_{0.5}$ = 59 min under sunlight exposure. Under the condition of 75-90% R.H., the comprehensive performance of the present DLH is still in the top tier. At ≤60% R.H., the DLH still shows competitive water capture capacity and higher release efficiency compared to MOF-based AWH systems. This performance is also higher than all hydrogel-based AWH materials. Notably, the DLH exhibits a 60% increase in water adsorption capacity compared to the monolayer hybrid hydrogel with the same composition (the control sample) (**Figure 5.8**). These results suggest that the current mainstream hybrid AWH hydrogels have great potential to further improve the water adsorption efficiency after functional separation using this “divide and conquer” strategy.

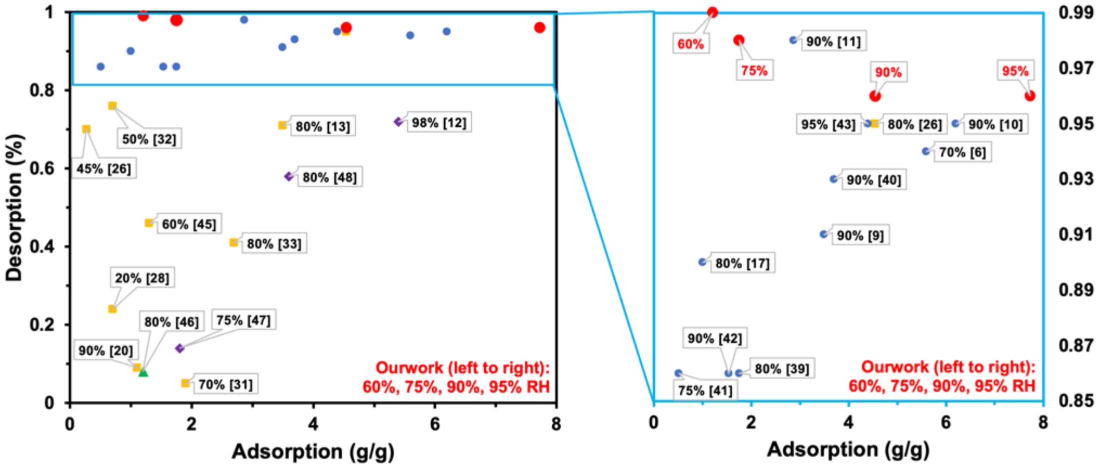

Figure 5.14 Recent publications of sorption based AWH materials and their unsaturated water adsorption and release efficiency. Comments of each dot refers to the value of experimental relative humidity and reference. (Blue dots: hydrogel[1, 90, 92, 95-96, 107, 182-183, 204]; Yellow rectangle: MOF[66, 73, 110, 113, 196-199, 205]; Green triangle: ionic liquid[81]; Purple diamond: hygroscopic inorganic compounds[114-115, 206]; Red dots from left to right: our work at 75%, 90%, and 95% RH conditions).

5.3.3 Practical outdoor performance and durability

To ensure that the DLH can withstand multiple water adsorption and release cycles, we then performed a cyclic durability test (**Figure 5.15A**). Each cycle includes 8 h water adsorption under 95% R.H. and 4 h water release under sunlight irradiation. After each releasing process, the hydrogels were exposed to sunlight for an additional 1 h to remove any residual water. After 10 cycles, the DLH (LHL/WAL = 1/3 (v/v)) displayed an average water adsorption capacity of 5.31 g g^{-1}, with an error of < 5%. After 4 h of sunlight exposure, the average water release efficiency was ca. 97%. Under sunlight exposure, the LHL can convert electromagnetic waves into heat and undergo axial shrinkage due to the thermal response of PNIPAM. This deform provides the WAL with a horizontal shear force towards the axis, which physically promotes the rapid evaporation of liquid water inside the WAL (**Figure 5.15B**). Thereafter, we again performed SEM characterization of the DLH sample to investigate its interface morphologies. As shown in **Figure 5.16**, no layer detachment was observed after 10 cycles. This result thus demonstrates that the introduction of NIPAM (25 wt%) component into the WAL can enhance its compatibility with LHL.

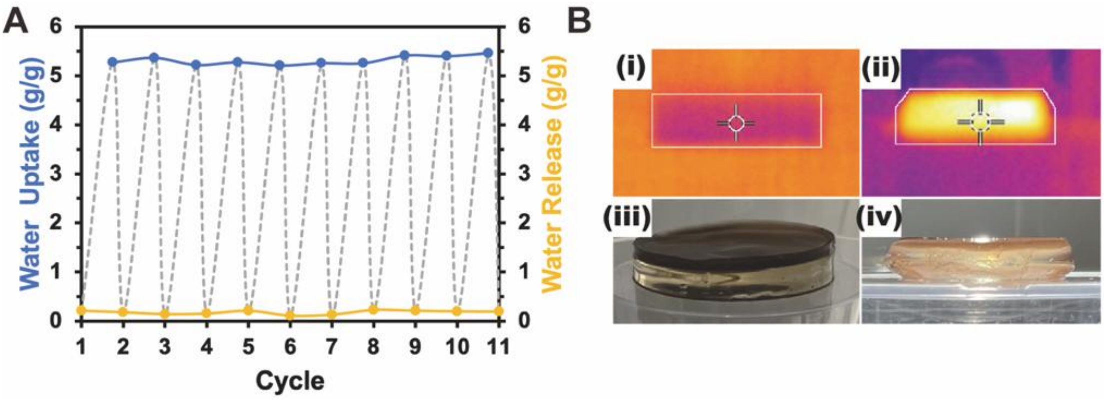

Figure 5.15 (A) Durability performance of dual-layered hydrogel with LHL:WAL=1:3 (volume ratio). (B) Temperature measurement and the appearance of dual-layered hydrogel under simulated sunlight irradiation (1.0 sun equivalent) for 30 min.

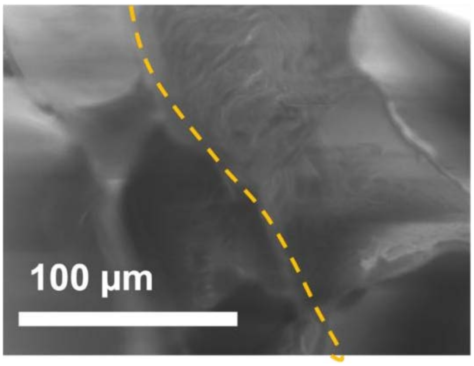

Figure 5.16 Well-connection illustration of DLH between LHL and WAL hydrogel after 10 times of durability tests

To further investigate the practical water adsorption and desorption performance, a laboratory-made water harvesting device was built as shown in **Figure 5.17A**. This device consists of a rectangular container and a rectangular cap with sloping top cover. Both container and rectangular cap are made of polystyrene. The inner shell of the container is covered by aluminum foil for enhanced heat accumulation during water desorption. The sloping top cover of the container is made from polyvinylidene chloride (PVC) film (cling wrap) for strong light transmission, while the hydrophobic PVC film is also great for water droplets movement. An enlarged DLH were prepared for the practical test. The water adsorption experiment was carried out during February 2022 at Sydney suburb, Australia, where the average temperature before sunrise was 19 °C, wind speed was 4 km h^{-1}, atmospheric pressure was 102.5 kPa, and relative humidity was ca. 80% R.H (the dew point was approximate 17.5 °C). After a continuous 8 h of water adsorption, the DLH sample showed an adsorption capacity of 1.94 g g^{-1}, with no sign of layer detachment or structural damage. The water release was then achieved by exploring the device under sunlight for 5 h. We observed that 50% of adsorbed water was released within 2 h with a consistent water releasing rate, and almost 100% of captured water was collected after 4 h irradiation (**Figure 5.17B**). We also noted that the water vapour condensed on the inner wall of the PVC film at the top cover of the container and then formed small droplets, which can refract and reflect sunlight, reducing the intensity of sunlight. The use of transparent super-hydrophobic cover may alleviate these effects. The quality of the produced water, environmental dew water, and deionized water were then measured by ICP-MS. As shown in **Figure 5.17C**, the concentrations of $\mathrm{Na^+}$ ($C_{\mathrm{Na+}}$) and $\mathrm{K^+}$ ($C_{\mathrm{K+}}$) of the condensed water were 0.077 mmol $\mathrm{L^{-1}}$ and 0.018 mmol $\mathrm{L^{-1}}$ respectively, which were much lower than the $C_{\mathrm{Na+}}$ and $C_{\mathrm{K+}}$ of DI water and dew water. This result implies that the liquid water produced by the DLH far exceeds the drinking water quality standards set by the World Health Organization.[207-208]

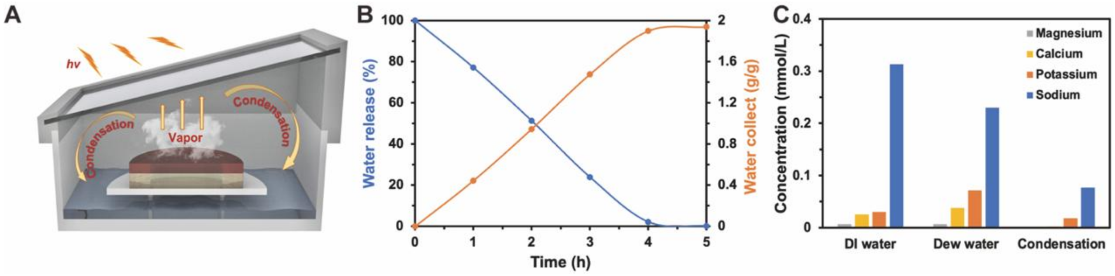

Figure 5.17 (A) Self-designed AWH equipment for water releasing experiment. (B) Practical test of atmospheric water adsorption and sunlight-assisted water releasing of AWH hydrogel. (C) ICP-MS of DI water, dew water, and the condensed water from the dual-layered hydrogel for ions concentration measurement.

This DLH hydrogel exhibits outstanding water harvesting performance in both laboratory and practical experiments, suggesting its application potential in a real natural environment. Here, we reasonably provide the following potential application according to the environmental temperature and relative humidity record from Australian government Bureau of Meteorology. In Sydney, Australia, which is dominated by a humid subtropical climate, the average temperature in the early morning from November to April (summer season) is about 25 °C and the relative humidity is 74%. At night, the lowest temperature is between 15-18 °C, which means that night-time air humidity in Sydney can often reach or exceed 90% R.H. Similar climatic environments also appear in Zimbabwe, Zambia, Botswana in Africa, Uruguay in South America, southern Brazil, north-eastern Argentina, Alabama, Georgia, Florida in the south-eastern United States, as well as Fujian Province, Guangdong and other southern-coastal areas in China. In a desert climate with a harsher environment, take the Ayers Rock region in the subtropical desert climate in the Northern Territory of Australia as an example. The average summer temperature in the Ayers Rock region is 35 °C during the daytime (average humidity = 20%), and below 20 °C at night. Despite the high temperature during the daytime, the warmer air has potential containing more water vapor, so that the relative humidity in this area at night can reach more than 80% R.H.. The climatic conditions in these regions allow the DLH to perform optimally for efficient AWH, which is significant for reducing carbon emissions and providing a low-cost, stable supply of drinking water worldwide.

5.3.4 Conclusion

In this study, we reported a promising design strategy, "divide and conquer", to construct composite DLH materials for AWH applications that separated the water adsorption and autonomous sunlight-assisted water releasing via two layers. This strategy minimized the functional inhibition caused by poor interfacial compatibility and maintained stable interlayer connections. The WAL achieved an efficient water adsorption, and the LHL is able to heat up the DLH above 50 °C under sunlight, thereby promoting efficient water release. The prepared DLH exhibits excellent water adsorption and release performance under high to moderate humidity conditions. More importantly, the water adsorption performance of this DLH was improved by 60% compared to the conventional hybrid hydrogel counterpart. We thus believe that the new strategy of dual-layered AWH hydrogels represents a promising design for the preparation of next-generation, high performance AWH materials.

Chapter 6: Biomimetic Hydrogels: Reducing Axial Stress in Swelling Polymer Materials for Atmospheric Water Harvesting

Related publication:

Feng, A., Mao, S., Onggowarsito, C., Naidu, G., Li, W., & Fu, Q. (2023). Tillandsia-inspired composite materials for atmospheric water harvesting. *ACS sustainable chemistry & engineering*, 11(15), 5819-5825.

This chapter investigates innovative materials inspired by the unique water-absorbing properties of Tillandsia plants. These bio-inspired composite materials demonstrate promising improvements in capturing atmospheric moisture, offering potential solutions for addressing water scarcity. Future research focused on overcoming barriers to long-term durability and environmental sustainability will be crucial for the successful application of Lutulan-based atmospheric water harvesting systems.

6.1 Introduction

The earth has inexhaustible water resources, yet only 2.5% of the earth's total water resources are freshwater. Among them, 0.3% of surface freshwater is distributed in the atmosphere in the form of water vapor, accounting for 2×10^{10} m^3, which is a considerable freshwater resource that has attracted increasing attention in recent years[209-211]. Capturing water from the air is known as AWH process[212-213]. Water harvesting strategies can be divided into active condensation and passive condensation.

Active condensation is arguably more efficient in water collection, however this strategy typically consumes secondary energy and/or chemical refrigerants. Passive condensation is considered to be an ideal energy-saving alternative.[70, 214]

Nature is the best designer. Tillandsia, an air plant that grows in arid regions, has evolved a special physiological structure to adapt to the arid climate.[215-216] In detail, the "leaves" of the air plant are fleshy stems tightly surrounded on the surface by stomata and spike-like structures growing around the stomata (**Figure 6.1**). At night, the tip of the spike array can liquefy the water vapor in the air, and the liquefied water droplets can gather around the stomata driven by the Laplace gradient and be absorbed by the fleshy stem, making it survive in harsh environments.[217] Unfortunately, most of the artificial AWH materials based on hydrogels or metal-organic frameworks (MOFs) are arguably to have insufficient vapour liquefaction ability.[63, 133] Although researchers have incorporated hygroscopic salts into these materials to enhance their water adsorption capacity under ambient conditions, the strong affinity of hygroscopic salts for water molecules in turn leads to reduced water release/production efficiency.[78, 218] For example, Li et al. reported a PAM-based hydrogel containing calcium chloride and carbon nanotubes, with a maximum water adsorption capacity of 2.05 g g^{-1} and a low desorption efficiency of 55%.[1] The trade-off between water uptake (under low-mediate humidity) and water release efficiency under ambient conditions limit the practical applications of artificial AWH materials. We thus saw this as an opportunity to engineer a Tillandsia-inspired AWH material to improve the water production in low to moderate humidity conditions.

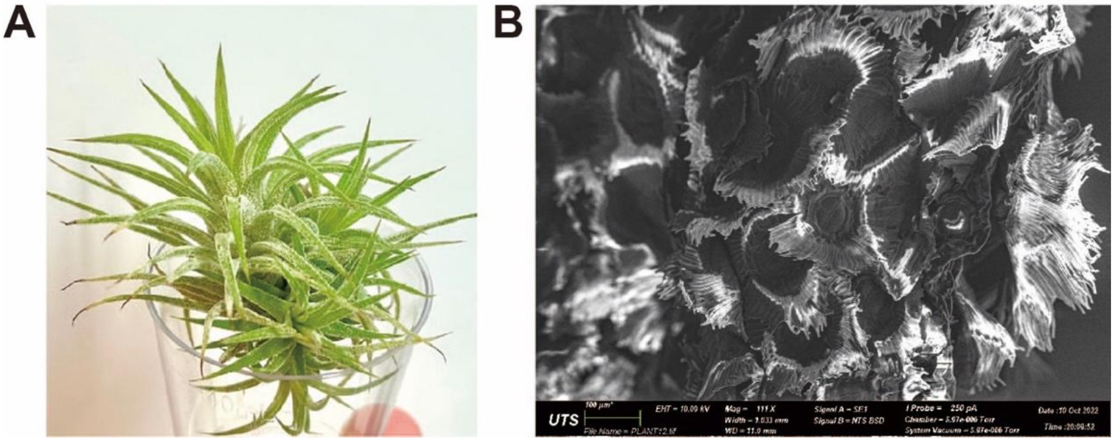

Figure 6.1 (A) Optic image of Tillandsia air plant. (B) SEM image of the surface of Tillandsia air plant.

The surface of the Tillandsia leaves liquefies water vapor at night, and the liquefied water is quickly transferred to the underlying storage layer for Tillandsia's survival needs. Inspired by the asymmetric structure of Tillandsia ‘leaves’, we developed a novel bioinspired composite (BiC) consisting of a hygroscopic salt-containing nonwoven layer and a hydrogel network for efficient AWH application. The resulting BiC material can utilize diurnal temperature difference to condense water vapour at night and then produce liquid water through evaporation-condensation during the hot day. Under a low-moderate humidity environment, the BiC composite exhibits an outstanding water adsorption capacity and a high-water release ratio without the use of conventional photothermal materials (PTMs). The study thus reports a new avenue to develop biomimetic materials for practical AWH applications.

6.2 Experimental section

6.2.1 Material and chemical synthesis procedure

N,N′-Methylenebis(acrylamide) (BIS, 99%, Sigma-Aldrich), [2-(acryloyloxy)ethyl]trimethylammonium chloride solution (AEtMA, 80 wt% in H_2O, Sigma-Aldrich), *N,N,N′,N′*-tetramethylethylenediamine (TEMED, 99%, Sigma-Aldrich), ammonium persulfate (APS, 98%, Sigma-Aldrich), calcium chloride ($CaCl_2$, 97%, Sigma-Aldrich) sodium chloride (NaCl, 99%, Sigma-Aldrich), lithium chloride (LiCl, 99%, Sigma-Aldrich), and magnesium chloride ($MgCl_2$, 98%, Sigma-Aldrich) were used as received without further purification. Deionized water (DI water) was obtained by Milli-Q water purification system (18.2MΩ.cm @25 °C). The disposable medical masks were purchased from supermarket.

Preparation of the nonwoven water adsorption layer: we obtained the nonwoven sheet by cutting off the face mask, and then immersed it in 1M $CaCl_2$ solution under sonication. The sheet was then removed, spread out on flat glass and oven dried until ready to use.

For a typical synthesis of the asymmetric BiC, 0.025 g BIS (crosslinker) and 0.442 mL AEtMA solution (80 wt% in water) were mixed and dissolved in 1.458 mL DI water under sonication. Then, 10 μL TEMED was added into the prepared solution and followed by sonication. To start the gelation, 100 μL APS solution (0.53 M) was added into the prepared solution to induce polymerization. Once the gelation start, gently cover the surface of solution with a prepared non-woven material. The polymerization was carried out for 2 h at room temperature. The as-prepared BiC was freeze dried overnight. The mass proportion of each component of BiC-1 are also shown in **Table 6.1**:

Table 6.1 The mass proportion of each component of BiC-1.

Layer	Component in BiC-1	Mass (g)	Mass proportion (%)
Adsorption layer	$CaCl_2$	0.0317	6.41
	Nonwoven fiber	0.0378	7.64
Storage layer	PAEtMA	0.425	85.95

6.2.2 Characterizations

UV-Vis spectra were recorded on a SHIMADZU UV-1700 UV-Visible spectrophotometer.

Fourier-transform infrared spectroscopy (FT-IR) spectra were obtained using a SHIMADZU MIRacle 10 single reflection ATR accessory.

Scanning electron microscope (SEM) images were obtained by Zeiss EVO LS15 SEM system.

Infrared thermometer (IR) images were captured using FLUKE PTi120 thermal imager.

Sunlight simulation light source was obtained from Beijing NBeT HSX-F300 xenon light source. Inductivity coupled plasma mass spectrometry (ICP-MS) characterization was conducted using an Agilent Technologies 7900 ICP-MS system with SPS-4 Autosampler.

6.2.3 Moisture adsorption experiments

The moisture adsorption tests were conducted under 0.6 L min^{-1} air flow with different relative humidity (R.H.%). Dried compressed air was blow to supersaturated salt solution, then the humidified air flows to the surface of WAL of the hydrogel. The R.H. of the air flow were stabilized using potassium sulphate (R.H. = 90%), sodium bromide (R.H. = 60%) and magnesium chloride (R.H. = 30%). For instance, in a 500 mL flat bottom flask, 25 g potassium sulphate was dissolved in 200 mL DI-water. The pipe that flowed dried compressed air was immersed under the level of the supersaturated potassium sulphate solution. Moist air blow to a container that held the BiC. The bottom of the container was immersed in an ice water bath, which created a vertical temperature changing profile. To prevent the absorption of condensed liquid water, BiC sample in the container was held on a shelf that prevents the BiC contacting with the 'inner wall' of the container. The mass of the BiC was recorded and the condensed liquid water in the container was removed every 30 min.

6.2.4 Sunlight-assisted autonomous water release

The in-door sunlight-assistant evaporation was conducted using a XE300WUV Xenon light source (Beijing NBeT Technology Ltd) to simulate sunlight. The irradiation intensity was stabilized at 1,000 W m^{-2} (1.0 sun equivalent). The mass of BiC was monitored using an analytical balance with internal calibration (OHAUS Pioneer® analytical balance) every 15 min. The surface temperature of the hydrogel side of BiC was determined by IR camera (FLUKE PTi120 thermal imager).

6.2.5 Durability test

The durability of the BiC material was determined at 60% R.H. for 10 cycles (for each cycle, we performed water adsorption for 8 h, followed by 4 h indoor sunlight irradiation). The BiC was placed with nonwoven side upward during water adsorption, and hydrogel side upward during sunlight irradiation. At the end of each cycle, the BiC material was further irradiated for 1 h to remove any potential water residue.

6.3 Results and discussion

6.3.1 Hydrogel structure and morphology

With the advent of the post-COVID era, the nonwoven materials in used masks are discarded, landfilled or incinerated along with the masks as medical waste, and the negative impact on the environment is inevitable. The nonwoven sheet has porosity, softness and certain mechanical strength, making it an ideal container for hygroscopic salts. Therefore, we innovatively employed nonwoven mask to immobilize hygroscopic salts.

In this work, we prepared a series of BiC materials for AWH application and recycling of disposable masks. As shown in **Scheme 6.1**, polyethylene terephthalate (PET) nonwoven sheets with hydrophilic surface obtained from commercially available masks, were first immersed in hygroscopic salt solution (e.g. $CaCl_2$) and dried in oven. Then, a poly[2-(acryloyloxy)ethyl]trimethylammonium chloride (PAEtMA)-based hydrogel network contained 20 wt% content were synthesized via free radical polymerization[183] and the nonwoven sheets were gently placed on the surface of the hydrogel during the gelation process (Step 2) to afford the BiC materials.

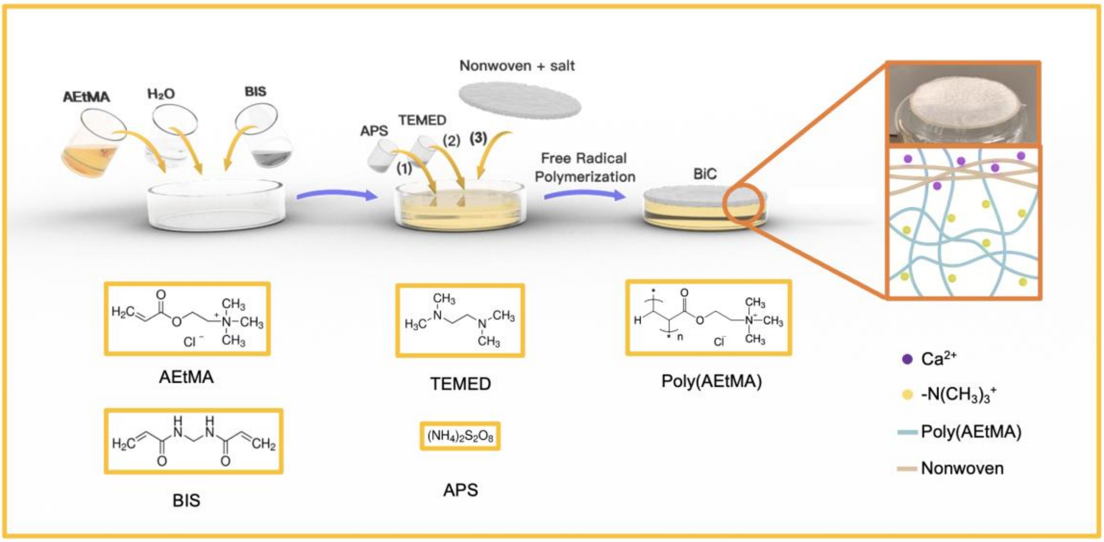

Scheme 6.1 Schematic illustration of the synthesis of composite AWH material.

We employed a nonwoven sheet to immobilize hygroscopic salts and constructed a polymeric hydrogel layer underneath. The porosity and huge swelling ratio of the PAEtMA network allow the water liquefied by $CaCl_2$ to pass through the polymer network from the nonwoven sheet via capillary force, thereby realizing the separation of the functions of vapor liquefaction and water storage in BiC materials to achieve high water adsorption and efficient water release. It is worth noting that although the treated non-woven sheet exhibits a strong rapid moisture adsorption capacity, as the vapor pressure of the calcium chloride solution increases with the increase in water adsorption, the evaporation and dissolution of water molecules will quickly reach a dynamic balance. This leads to the inability of the treated nonwoven sheet to store liquid water in large quantities. Therefore, the existence of the PAEtMA polymer network becomes a necessary condition for BiC to achieve high water adsorption capacity. This will be discussed further later.

We firstly characterized the surface morphology of the prepared BiC materials. We can clearly identify the rough nonwoven side and the relatively smooth hydrogel side using naked eye (**Figure 6.2A-i-iii**). After freeze drying, the nonwoven sheet was still closely connected with the PAEtMA hydrogel layer, and no obvious cracks were found at the interface (**Figure 6.2A-iv**). The microstructures of the surface of the nonwoven sheet, and the surface and cross-section of the PAEtMA network were characterized by SEM measurements (**Figure 6.2B**). We observed that the fibres of nonwoven sheet have a diameter of ca. 10 μm (**Figure 6.2B-i**). The unique microstructure of the nonwoven sheet provides large surface area for $CaCl_2$ immobilization and moisture liquefaction. In addition, the rough nonwoven surface offers large contact area to PAEtMA polymer network, improving interfacial connection. The polymer network has porous morphology, which is confirmed by both surface and cross-section images in **Figure 6.2B-ii** and **iii**) respectively.

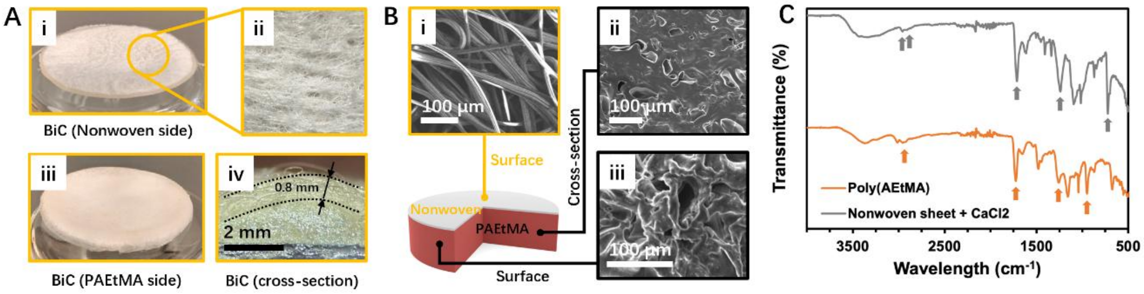

Figure 6.2 (A) Optic images of (i) surface of BiC (non-woven sheet side), (ii) optic microscopy image of non-woven fiber, (iii) the surface of BiC (polyAEtMA hydrogel side), (iv) optic microscopy image of the cross-section of BiC. (B) SEM images of (i) surface of non-woven sheet, (ii) cross-section and (iii) the surface of poly(AEtMA) hydrogel. (C) FT-IR spectra of the nonwoven sheet containing $CaCl_2$ (gray trace) and the PAEtMA hydrogel (orange trace).

The FT-IR spectra of the nonwoven substrate containing $CaCl_2$ and the obtained polymeric hydrogel layer were shown in **Figure 6.2C**. We observed the characteristic peaks at 1,250 cm^{-1} and 1,750 cm^{-1}, which can be attributed to the carbonyl-stretching (C-O and C=O, respectively) of the PET nonwoven sheet. With the introduction of $CaCl_2$ in the nonwoven sheet, we observed a distinct broad water peak at 3,000 to 3,700 cm^{-1}. This suggests that the $CaCl_2$ in the nonwoven sheet adsorbed water during the test. From the FT-IR spectrum of the PAEtMA hydrogel (orange trace), we observed the characteristic peaks at 1,480 cm^{-1} and 2,950 cm^{-1}, which are attributed to the stretching vibrations of N^+-C and C-H bonds of quaternary ammonium groups of PAEtMA, respectively. These results confirmed the successful preparation of BiC containing $CaCl_2$.

6.3.2 Water adsorption and desorption performance

We then evaluated the effects of the hygroscopic salts and the polymer hydrogels on the water production ability of BiCs though the vapor adsorption and desorption tests using a home-made setup. In the water adsorption experiments, BiC was placed in a plastic container immersed in an ice bath without touching the inner wall of the container (**Figure 6.3A**). The humidity (30-60% R.H.) is controlled by passing the dry air through different saturated salt solutions. Moist air with a fixed flow rate of 3.0 L min^{-1} and a fixed relative humidity flows in from the top of the container. During sunlight-assisted water desorption, BiCs were placed on a precision balance under the irradiation of a simulate sunlight (intensity = 1 kW m^{-2}, **Figure 6.3B**). Under optimal conditions, BiC can raise its PAEtMA hydrogel surface temperature up to 40.4 °C within 4 hours for photothermal evaporation (**Figure 6.4A&B**).

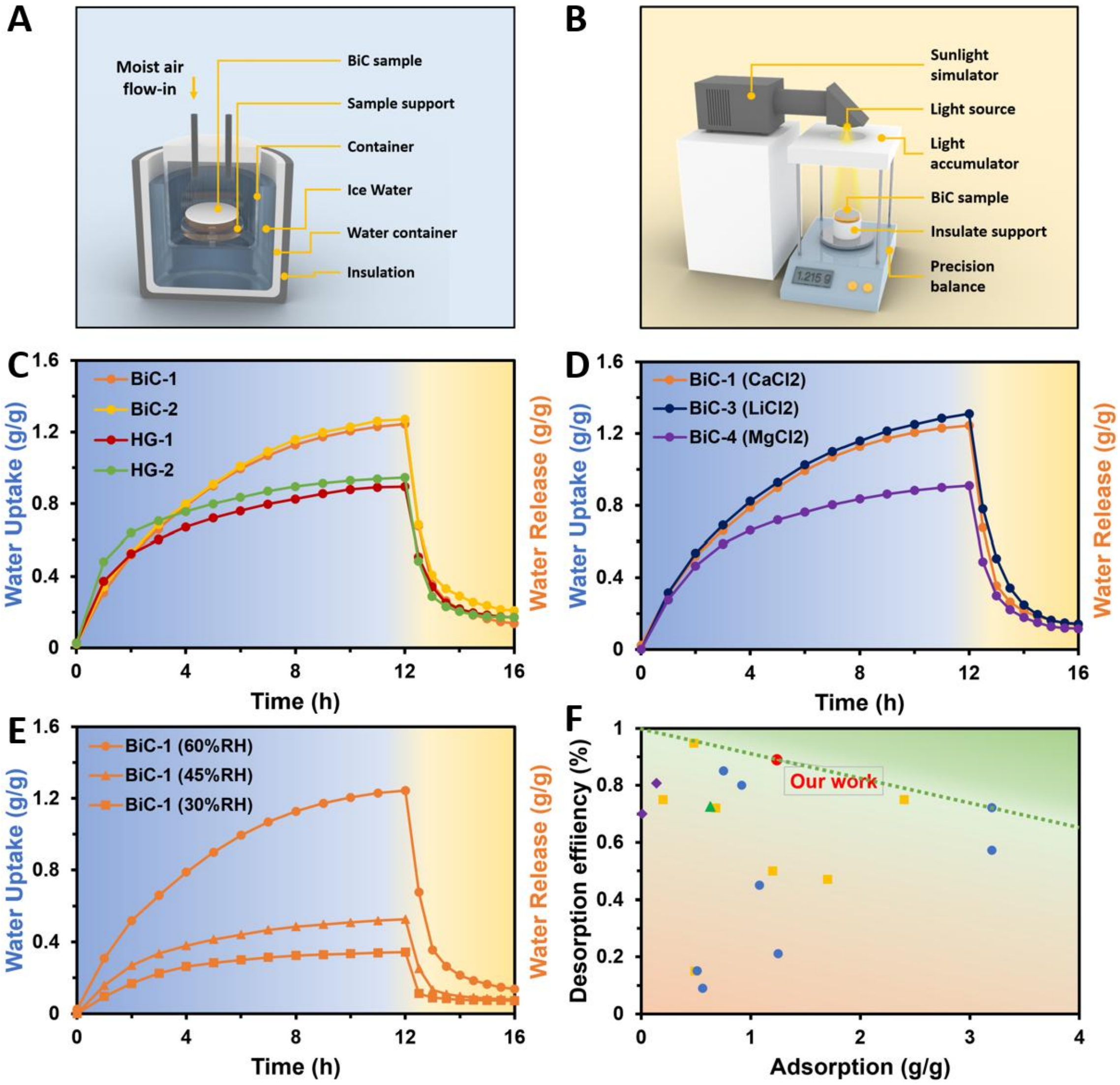

Figure 6.3 (A-B) Illustration of water adsorption and water desorption experiments, respectively. (C) In-door moisture capture and water release experiments of BiC-1 (orange trace), BiC-2 (yellow trace), HG-1 PAEtMA hydrogel (red trace) and HG-2 PAEtMA/$CaCl_2$ hybrid material (green trace). (D) Comparison of the in-door moisture capture and water release experiments of BiC-1 (1M $CaCl_2$ orange trace), BiC-3 (1M $LiCl_2$ dark blue trace), and BiC-4 (1M $MgCl_2$ purple trace) under 1.0 sun irradiation. (E) In-door moisture capture and water release experiments of BiC-1 at 30%, 45%, and 60% R.H. under 1.0 sun irradiation. (F) A trade-off (green dot line) between water adsorption capacity and water release efficiency of AWH materials: MOF and MOF composites (yellow rectangular)[59, 62, 73, 108, 110, 219-221], HICs

(purple diamond)[72, 114, 222], ILs (green triangular)[223], and hydrogels (blue dots)[1, 90, 94-95, 145-146, 183, 224-225].

We first optimized the loading of hygroscopic salts in BiC by tuning the concentration of the salt solution. In this study, we also prepared a control PAEtMA hydrogel without the nonwoven layer. As shown in **Figure 6.3C**, the bare PAEtMA hydrogel (HG-1, red trace) showed a water adsorption capacity of ca. 0.85 g g^{-1} under 60% R.H. While, when we introduced $CaCl_2$ into PAEtMA hydrogel, the resulting hybrid AWH material (HG-2, green trace) showed a water adsorption capacity of ca. 0.9 g g^{-1}. Interestingly, the HG-2 exhibited rapid water adsorption rate in the first 2 h, after which its adsorption rate gradually decreased. The amount of water collected in the first two hours accounts for ca. 67% of the total water adsorption in the 12 h water adsorption process. The rapid water adsorption is the result of the direct contact of water vapor and the hygroscopic salts and the quaternary ammonium groups. The subsequent decrease in water adsorption rate can be attributed to the formation of a saturated salt solution on the surface of the hygroscopic salts, resulting in an increase in vapor pressure, thereby inhibiting rapid liquefaction of water molecules. In contrast, the BiC with nonwoven-$CaCl_2$ (orange trace, 1M $CaCl_2$ solution, denoted as BiC-1) displayed an improved water liquefaction capacity, resulting in a higher water adsorption capacity of ca. 1.24 g g^{-1} within the same time frame. This is because the liquefied water would be transferred and stored in the PAEtMA hydrogel layer. This result thus proves that an independent water liquefaction layer containing hygroscopic salt can effectively enhance the water adsorption capacity of an AWH material. In addition, we found that further increasing the concentration of $CaCl_2$ solution (from 1 mol L^{-1} to 2 mol L^{-1}, denoted as BiC-2, yellow trace) did not significantly improve the water adsorption capacity. For BiC-2, due to its high hygroscopic salt content and strong hydrogen bonding between the hygroscopic salt and liquefied water, the transfer of liquefied water from WAL to the underlying PAEtMA is slower, which hinders the subsequent liquefaction of water vapor. During the subsequent water release, we observed that the BiC-2 showed lower water release efficiency than that of BiC-1, which could be attributed to its higher salt loading and stronger interaction with water molecules.

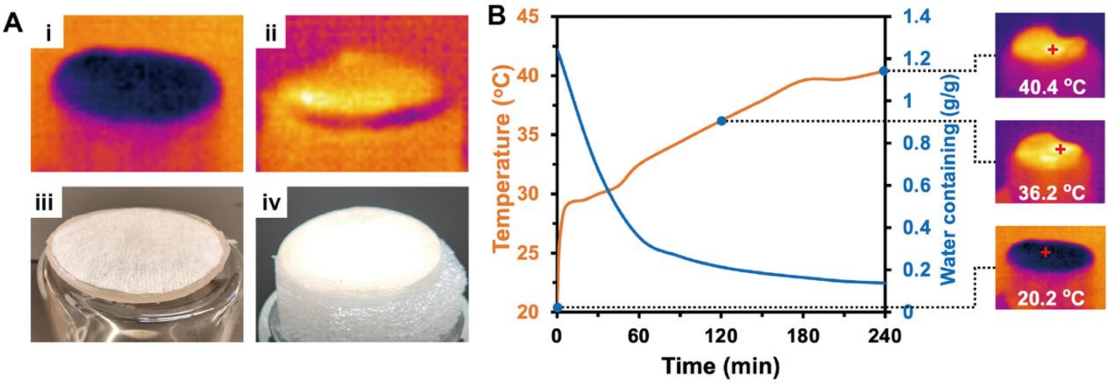

Figure 6.4 (A) Optic images of the prepared BiC (nonwoven side). (B) Surface temperature profile and the IR images of the BiC (hydrogel side) under the sunlight irradiation.

We further optimize the water liquefaction ability of BiC by varying the types of hygroscopic salts. Apart from $CaCl_2$, we also introduced widely used LiCl and $MgCl_2$ into the nonwoven sheet to afford BiC samples (denoted as BiC-3 and BiC-4, respectively in **Figure 6.3D**). Compared with BiC-1, the BiC-3 containing LiCl exhibited 5.3% enhanced water adsorption capacity at the expense of 3.4% lower water release efficiency. Since we did not incorporate PTM into the BiC material, we focused more on the water release efficiency within a similar range of water adsorption capacity. On the other hand, the water adsorption capacity of BiC-1 is 136.9% of that of BiC-4 containing $MgCl_2$. Furthermore, we also directly compared the water liquefaction capacity of nonwoven sheets (not BiC) containing $CaCl_2$ and $MgCl_2$ and found that the nonwoven incorporating $CaCl_2$ exhibited higher water liquefaction capacity (ca. 115.2% improvement, **Figure 6.5**). These results all indicate that the water adsorption capacity of BiCs is affected by hygroscopic salts.

Thereafter, we tested the water adsorption capacity of the BiC-1 under different R.H. conditions (30, 45 to 60% R.H.) at a moisture flow rate of 3 L min^{-1}. It is found that the water adsorption capacity of BiC-1 is 0.34, 0.53 and 1.24 g g^{-1} at 30%, 45% and 60% R.H., respectively (**Figure 6.3E**). Compared with the low 30% R.H., the water adsorption capacity of BiC-1 increased by 261.8% at 60% R.H. This result demonstrates the potential of BiC for efficient water adsorption under arid environment compared with most hydrogel based AWH materials, which typically displayed poor water adsorption capacity below 60% R.H.[146, 217, 225]

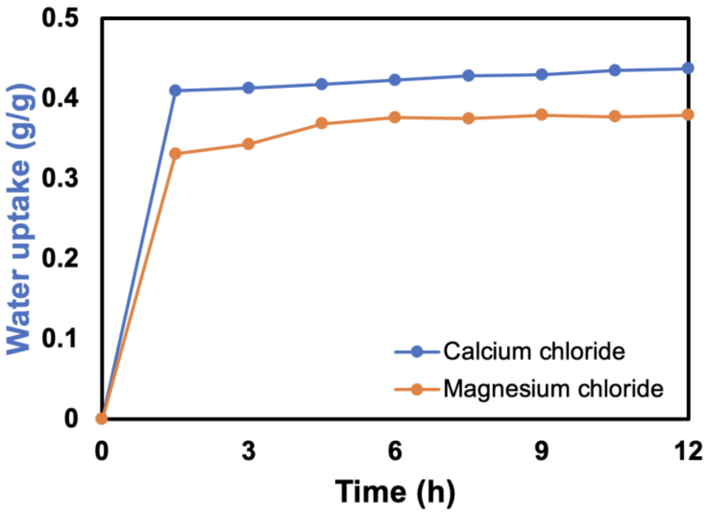

Figure 6.5 Water adsorption performance of non-woven sheets after soaking in 1M calcium chloride and magnesium chloride solutions.

We also prepared another BiC consisting of the same nonwoven layer but poly(3-acrylamidopropyl)trimethylammonium chloride (PAPtMA) hydrogel layer and denoted it as BiC-5. Notably, both the PAEtMA- and PAPtMA-based hydrogel layers are rich in ammonium groups (**Figure 6.6A**). The BiC-5 with PAPtMA hydrogel layer displayed a 14% lower water adsorption capacity. This result may be attributed to the higher molecular weight of the APtMA. Under the same monomer content, the PAEtMA network has more quaternary ammonium ions than that PAPtMA hydrogel layer. We then optimized the volume and density of the water-storage PAEtMA network and investigated this effect on the water adsorption capacity of BiC material. As mentioned above, we did not apply PTM in the preparation of BiCs, thus the excellent solar-assistant evaporation performance of BiC is attributed to its thin PAEtMA layer and high aspect ratio. We found that when we doubled the thickness of the PAEtMA hydrogel layer, water adsorption capacity of BiC-1 decreased from 1.24 g g^{-1} to 0.56 g g^{-1} (**Figure 6.6B**). Due to the constant water liquefaction rate of the WAL layer, filling a thicker PAGEMA layer with water requires a longer time (over 12 h). However, the water adsorption process over 12 h is not practical for AWH applications. Therefore, in this study, further increasing the thickness of the PAEtMA layer only increases the mass of BiC, significantly reducing the water adsorption capacity of BiC. Due to the difference in swelling ratio between nonwoven fiber and PAEtMA hydrogel, we must optimize the density of PAEtMA layer to control its mechanical stability and swelling ratio to find a balance between maintaining the structural integrity of BiCs and maximizing their water absorption capacity. As shown in **Figure 6.6C**, when we further decreased the density of the PAEtMA layer to below 20 wt%, we observed an increase in water adsorption capacity, but the resulting PAEtMA network became brittle. On the other hand, further increasing the mass content of PAEtMA to 40 wt% led to a decrease in the swelling ratio and hence the water adsorption capacity per gram of BiC also decreased.

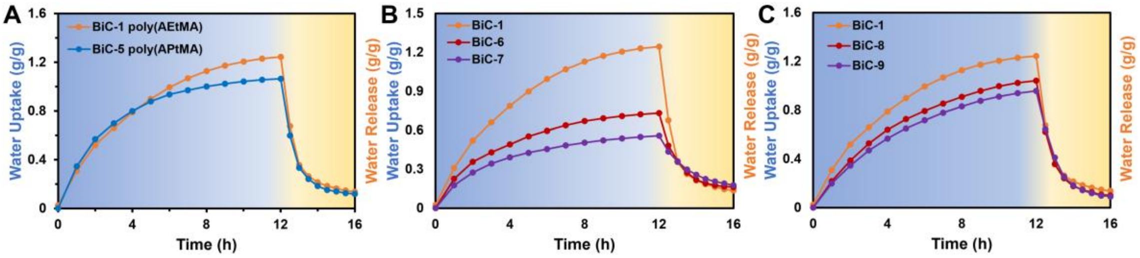

Figure 6.6 (A) Water adsorption and sunlight-assisted water desorption performance of BiCs containing PAEtMA (BiC-1) or PAPtMA (BiC-5) hydrogel layer, at 60%RH. (B) Water adsorption and sunlight-assisted water desorption performance of BiCs with different volume of hydrogel layers (BiC-1, BiC-6, and BiC-7 are of 2 mL, 3 mL, and 4 mL, respectively). (C)

Water adsorption and sunlight-assisted water desorption performance of BiCs with different mass contents (BiC-1, BiC-8, and BiC-9 are of 20 wt%, 30 wt%, and 40 wt%, respectively).

We further compared the AWH performance of BiC-1 with recently reported AWH materials (including metal-organic frameworks (MOFs) and their derivatives, hygroscopic inorganic compounds (HICs), ionic liquids (ILs), and hydrogels (**Figure 6.3F**). It is worth noting that in order to achieve high AWH performance, many studies reported using an air flow with higher R.H. as well as using a heating plate to drive evaporation. To be fair, we only compared the AWH data obtained under similar experimental conditions, e.g. below 60% R.H. and solar assisted evaporation. As seen, the MOF-based materials (yellow rectangular) generally exhibit high water adsorption capacity in low relative humidity environments, but have high residual water content even under sunlight irradiation. On the other hand, the hydrogel AWH materials (blue dots) generally show high sunlight-assisted desorption efficiency yet with a relatively low water adsorption capacity. As discussed above, the HICs (purple diamond) can quickly liquefy water vapor, but at the same time metal ions will dissolve in water to quickly form a saturated solution, preventing further moist liquefaction. In short, we can clearly observe a trade-off between the water adsorption capacity and the water release efficiency of AWH materials. In this study, the prepared BiC-1 exhibited excellent and balanced AWH performance, well ‘sitting’ at the frontline (aka. the upper bound) of the AWH trade-off.

6.3.3 Practical outdoor performance and durability

Thereafter, we conducted durability tests to determine the structural stability and the AWH performance of the BiC-1 subjected to multiple water adsorption/desorption cycles using a home-made water harvesting device. The water is produced by sunlight-assisted evaporation and subsequent condensation process. Under sunlight irradiation the water condensed, formed droplets, then flow towards the bottom of container for collection (**Figure 6.7A**). After ten water adsorption and release cycles (total 120 h), the obtained BiC-1 can still maintain its AWH performance with ca. 1.1 g g^{-1} water adsorption capacity and 84.6% water release efficiency (**Figure 6.7B**). The evaporated water was subsequently condensed in the device, achieving a total 0.75 kg kg^{-1} daily water production. The collected water was then characterized by ICP-MS to determine the salt concentration. The ion concentrations of Sydney tap water and laboratory deionized water were also measured for reference. As shown in **Figure 6.7C**, Sydney tap water had the highest Na^+ and Ca^{2+} ion concentrations of 12.69 mg L^{-1} and 11.69 mg L^{-1} respectively, followed by laboratory deionized water (<0.01 mg L^{-1} and 0.13 mg L^{-1}, respectively). The concentration of ions (Na^+, Ca^{2+}, Mg^{2+} and K^+) in the collected water is the lowest among them. The calibration curves of all ions are shown in **Figure 6.8A-D**.

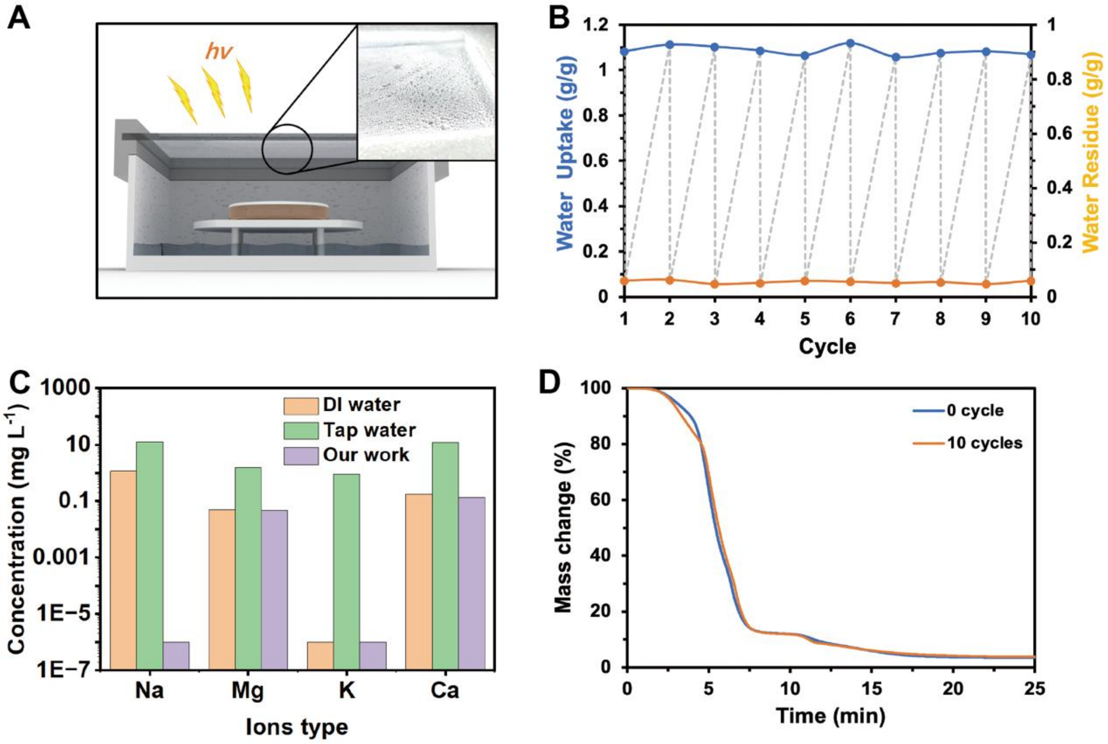

Figure 6.7 (A) Illustration of the home-made water harvesting device. (B) AWH performance of BiC-1 in 10-times cycling tests. (C) Ion concentrations of Sydney tap water, DI water and the collected water using BiC-1. (D) TGA curves for residue calcium chloride content in PAEtMA network before and after ten water adsorption/desorption cycles.

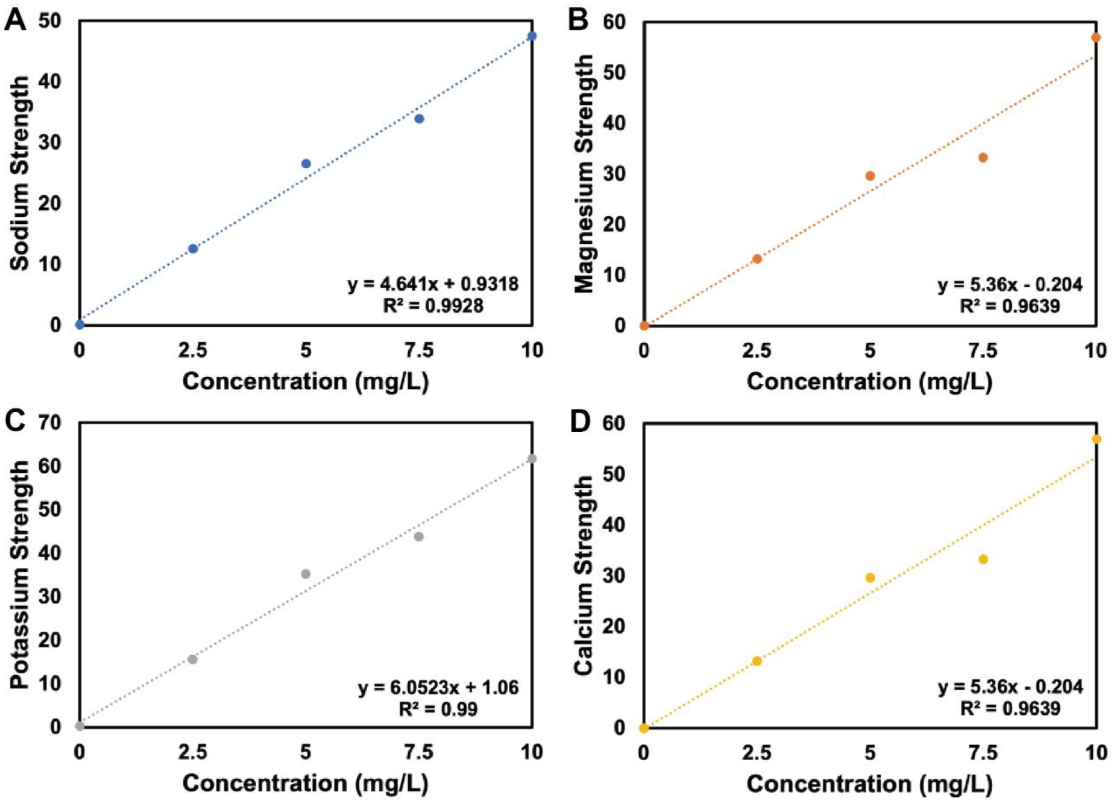

Figure 6.8 Calibration curves for solutions of (A) sodium ion, (B) magnesium ion, (C) potassium ion and (D) calcium ion.

Due to different swelling ratios of the nonwoven sheet and the PAEtMA hydrogel layer, strong repulsive tension may be generated at their interface during the water adsorption-desorption processes. We thus characterized the cross-section morphology of the BiC-1 after cycling tests to determine its structural stability. As shown in **Figure 6.9**, the PAEtMA hydrogel layer is still closely attached to the nonwoven sheet without obvious gaps or detachment. Moreover, for hydrogel AWH materials, the incorporated hygroscopic salts have been reported to leach from the polymer matrix to the produced water, resulting in performance decay and potentially environmental contamination issues[78]. For the BiC system, because the liquefied water finally flows to the PAEtMA hydrogel layer, we performed TGA measurements to verify if any $CaCl_2$ leached to the hydrogel layer. The as-prepared PAEtMA hydrogel layer of BiC-1 was measured by TGA first (blue trace, **Figure 6.7D**). After ten water adsorption-release cycles, the hydrogel layer of the BiC-1 was also removed, dried and characterized by TGA (orange trace). Interestingly, the two TGA traces are almost identical, the orange one shows only a slight increase (< 0.06 wt%) in the weight ratio of the residue. This result indicates that during the AWH processes, most of the $CaCl_2$ was retained in the nonwoven sheet of BiC material thus ensuring its high durability and stable AWH performance.

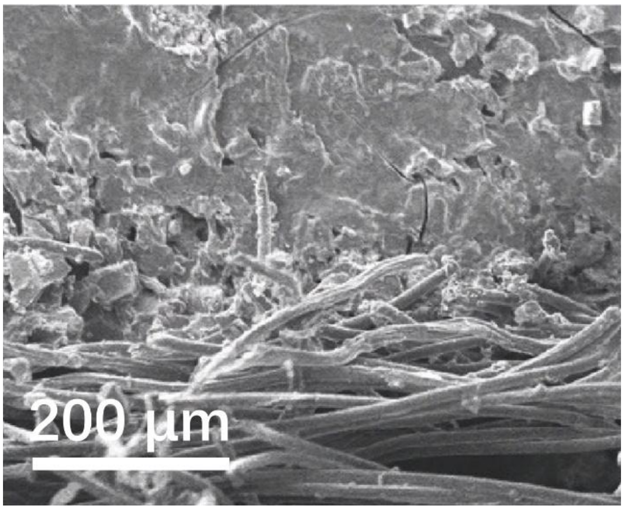

Figure 6.9 (A) Scanning electron microscope (SEM) image of the interface between nonwoven sheet and PAEtMA hydrogel layer after cycling test.

6.3.4 Conclusion

Inspired by the water capture process of Tillandsia air-plants, we developed an artificial composite material for efficient water production in low-moderate humidity (<60% RH) environments. The nonwoven surface treated with hygroscopic salts is applied to liquefy water vapor, and the PAEtMA hydrogel network beneath the nonwoven sheet has high porosity and a high swelling ratio for liquid water storage. The porous structure generates capillary force to drive the transport of liquid water from the nonwoven surface into the PAEtMA network. In addition, we also found that the BiC system can prevent the potential leaching of hygroscopic salts. We thus believe that the reported BiC material offers an alternative pathway for efficient AWH processes in harsh environments that do not require secondary energy and provides a potential solution for the recycling of discarded disposable masks in the post-COVID-19 era.

Chapter 7: Conclusion and Outlook

7.1 Conclusions

This thesis is dedicated to the development of cost effective fresh water production technology for AWH from unsaturated air using hydrogel composites. At the molecular level, we explore the structure-property relationships, and the thermodynamics as well as kinetics of water adsorption/desorption of AWH hydrogel materials. We found that additives favoring water adsorption tend to in turn constrain water desorption, leading to higher desorption temperatures as well as slower desorption rates. Subsequently, we further propose a novel "Divide and Conquer" strategy to achieve optimized water adsorption/desorption performance using dual layer Janus hydrogels. Additionally, we suggest an environmentally friendly recycling method for discarded masks in the post-COVID era. The main findings on hydrogel-based AWH composite materials are as follows:

For structure-property relationships of AWH hydrogel:

- Ionic polymer-based hydrogels (such as PAEtMA, PAMPS, and PAPtMA) exhibit an average water adsorption capacity approximately 40% higher than traditional non-ionic hydrogels (such as PAM and PNIPAM) under the same conditions. However, the difference in desorption efficiency is not significant, ranging between 62% and 85%.

- Simulation results of the polymer electrostatic potential difference indicate a positive correlation between the electrostatic potential difference, the swelling ratio of the hydrogel, and the water adsorption capacity. This suggests that molecular simulation could be a potential method for predicting the water adsorption performance of AWH hydrogels.
- There is no significant correlation between the pore size in the porous structure of hydrogels and the water adsorption capacity. However, pore density and pore size do affect the initial adsorption rate of hydrogels. Dense porous structures exhibit an average initial adsorption rate approximately 50% higher than that of non-porous hydrogel surfaces.
- Poly(2-acrylamido-2-methyl-1-propanesulfonic acid) (PAMPS) hydrogels are demonstrated to be suitable for all-weather AWH operation.

For water desorption study:

- PAM hydrogels incorporating a coordination network structure with iron ions had static water absorption capacities 80%, 20%, and 30% higher than the bare PAM hydrogel at low (30% RH), medium (60% RH), and high (90% RH) humidity, respectively.
- Under high humidity conditions, PAM hydrogels adsorb more water, with a higher proportion of intermediate water compared to free water in the hydrogel.

The desorption rate is also influenced by the water adsorption capacity.

- The enthalpy of evaporation of the PAM-GO hydrogel was 6.3% and 18.6% lower than that of the PAM-GO-Salt and bare PAM hydrogel, respectively. Correspondingly, the initial desorption rate were 27% and 160% higher, respectively. The lower enthalpy of evaporation indicates lower energy consumption for desorption, which is reflected in the higher initial evaporation rate.

For dual-layered Janus hydrogel:

- The water adsorption capacity of dual layer Janus hydrogels is approximately 60% higher compared to the samples by mixing PNIPAM-co-PAEtMA with PDA (Mn) NPs together. This indicates that the "Divide and Conquer" (independent functions) strategy reduces the interactions between additives, and thus enhance the potential to increase AWH performance.
- Increasing the amount of photothermal material in the LHL, raising the proportion of ionic monomers in the WAL, and increasing the ratio of WAL to LHL all positively impact the water adsorption capacity of the dual-layer hydrogel.
- The PDA (Mn) NPs photothermal material, used for the first time in AWH hydrogels, can raise the temperature of LHL from 23 °C to 45.4 °C within 4 h under sunlight. This represents a 4.6-fold increase in thermal conversion

compared to bare PNIPAM sample.

For biomimic hydrogel with non-woven layer:

- The non-woven fibers inside medical masks are treated with ethanol and calcium chloride solution, and used as a surface layer that is then coated with cross-linked PAEtMA layer. The incorporation of $CaCl_2$ in non-woven enhances the liquefaction ability of water molecules, resulting in an average 33% increase in water adsorption capacity.
- The water-absorption capacity of the AWH material containing calcium chloride was higher than that of both the magnesium chloride- and lithium chloride-containing BICs. In addition, nonwoven fibers containing lithium chloride can easily detach from the underlying PAEtMA layer.
- PAEtMA hydrogel containing calcium chloride-treated non-woven fibers achieved a static water adsorption capacity of 0.36 g g^{-1} under 30% RH environment. This indicates that such BIC material has great potential for water production in in desert or arid regions.
- Integrating non-woven fibers from masks as carriers of hygroscopic salts into AWH materials has been shown to achieve excellent water adsorption performance. This approach also offers a new method for recycling of disposed face masks in the post-COVID era.

7.2 Perspectives and Future Work

Current research on AWH hydrogel materials as focused on monomer selection, and the exploration of novel additives, including photothermal materials and vapor liquification chemicals. However, there are still knowledge gaps in kinetic and thermodynamics studies of water adsorption/desorption processes in AWH hydrogel. For AWH hydrogels, it is crucial to study the mechanism of water molecules during adsorption, storage, and desorption. This understanding should guide the design of the chemical structure and surface morphology of hydrogel materials. Due to the operation of AWH hydrogel in outdoor environments, they are susceptible to surface adhesion of bacteria and fine particulate matter. This could potentially damage the porous structure of the hydrogel and negatively affect its water adsorption/desorption processes. In addition, the design of AWH devices also faces challenges, especially in terms of improving energy conversion efficiency, reducing manufacturing costs, and reducing weight. This is essential for transitioning AWH materials from the laboratory to practical applications.

Therefore, future research on AWH hydrogels should emphasize the following aspects:

- Water Adsorption/Desorption Kinetics as well as Thermodynamic Studies of AWH Materials: We advocate the continued exploration of the entire process from the time a water molecule contacts the material surface to the time it leaves the hydrogels. Establishing correlations between water adsorption capacity and macroscopic parameters of the hydrogels (e.g. dimension, configuration, aspect ratio, surface morphology, pore size, pore wall thickness, pore density, etc.) and microscopic parameters (e.g. functional groups, electrostatic potential difference, cross-linking density, etc.) is crucial to address the selection of AWH materials.

- Using Computer Simulation and Big Data for Optimizing AWH Material Performance: Current research has partially validated the advantages of computer simulation in AWH material design. Molecular simulation techniques are considered capable of predicting water adsorption capacity of hydrogel materials. In addition, computational fluid dynamics simulations are also helpful in AWH device design and predicting water desorption efficiency. The role of big data manifests in leveraging the chemical properties of functional groups to aid in screening monomers and additives with AWH potential efficiently. This contributes to more effective design and synthesis of the next generation of AWH polymer composite materials in the future.
- Exploring the Prospects of Antibacterial Polymer Materials in AWH: Incorporating antibacterial properties into polymer materials is an important consideration for AWH. The introduction of ionic polymers may enhance water adsorption capacity while preventing bacterial growth. The selection of ionic polymers can be strategically based on various bactericidal principles, such as the differences in cell membrane surface components between Gram-negative and Gram-positive bacteria, which influence the appropriate bactericidal approach.

- Gradually Reducing Energy Dependence of AWH Devices: AWH devices should be closely integrated with hydrogel materials to achieve maximum efficiency. It is undeniable that separating water molecules from dry air requires energy, which comes from sunlight. However, solar radiation energy is not constant, necessitating energy storage devices such as batteries are required for use on cloudy days or at night. Therefore, saving energy input during the desorption process helps to reduce the volume of batteries and solar s, as well as meets the lightweight design requirements of future AWH devices.

References

[1] R. Li, Y. Shi, M. Alsaedi, M. Wu, L. Shi, P. Wang, *Environmental science & technology* **2018**, *52*, 11367-11377.

[2] D. K. Nandakumar, Y. Zhang, S. K. Ravi, N. Guo, C. Zhang, S. C. Tan, *Advanced materials (Weinheim)* **2019**, *31*, e1806730-n/a.

[3] F. Zhao, X. Zhou, Y. Liu, Y. Shi, Y. Dai, G. Yu, *Advanced materials (Weinheim)* **2019**, *31*, e1806446-n/a.

[4] M. A. Hanjra, M. E. Qureshi, *Food policy* **2010**, *35*, 365-377.

[5] P. H. Gleick, *Water in crisis, Vol. 100*, New York: Oxford University Press, **1993**.

[6] W. Emery, J. Meincke, *Oceanologica acta* **1986**, *9*, 383-391.

[7] D. Hinrichsen, H. Tacio, *The linkages between population and water. Washington, DC: Woodrow Wilson International Center for Scholars* **2002**, 1-26.

[8] C. A. Schlosser, K. Strzepek, X. Gao, C. Fant, É. Blanc, S. Paltsev, H. Jacoby, J. Reilly, A. Gueneau, *Earth's Future* **2014**, *2*, 341-361.

[9] X. Zhu, C. Zhang, J. Yin, H. Zhou, Y. Jiang, *Journal of Hydrologic Engineering* **2014**, *19*, 411-421.

[10] C. A. Rodriguez, K. W. Flessa, D. L. Dettman, *Conservation Biology* **2001**, *15*, 249-258.

[11] J. Briscoe, *International Journal of Water Resources Development* **1999**, *15*, 301-308.

[12] G. Micale, L. Rizzuti, A. Cipollina, *Seawater desalination: conventional and renewable energy processes, Vol. 1*, Springer Berlin Heidelberg, **2009**.

[13] I. C. Karagiannis, P. G. Soldatos, *Desalination* **2008**, *223*, 448-456.

[14] G. Wei, Z. Yang, B. Cui, B. Li, H. Chen, J. Bai, S. Dong, *Water resources management* **2009**, *23*, 1763-1780.

[15] M. A. Al-Sahlawi, *Desalination* **1999**, *123*, 143-147.

[16] R. Li, M. Wu, Y. Shi, S. Aleid, W. Wang, C. Zhang, P. Wang, *Journal of Materials Chemistry A* **2021**, *9*, 14731-14740.

[17] L. Hao, N. Liu, H. Bai, P. He, R. Niu, J. Gong, *Journal of Colloid and Interface Science* **2022**, *608*, 840-852.

[18] M. S. Irshad, X. Wang, M. S. Abbasi, N. Arshad, Z. Chen, Z. Guo, L. Yu, J. Qian, J. You, T. Mei, *ACS Sustainable Chemistry & Engineering* **2021**, *9*, 3887-3900.

[19] B. Pirouz, S. A. Palermo, M. Turco, *Water (Basel)* **2021**, *13*, 546.

[20] L. Caldas, A. Andaloro, G. Calafiore, K. Munechika, S. Cabrini, *Water and environment journal : WEJ* **2018**, *32*, 493-499.

[21] A. V. De Santo, A. Alfani, P. De Luca, *Annals of Botany* **1976**, *40*, 391-394.

[22] A. Rijke, *Journal of Experimental Biology* **1972**, *56*, 195-200.

[23] C. Joubert, G. Maclean, *African Zoology* **1973**, *8*, 141-152.

[24] S. C. Thickett, C. Neto, A. T. Harris, *Advanced Materials* **2011**, *23*, 3718-3722.

[25] Z. Chen, Z. Zhang, *Water science and technology* **2020**, *82*, 207-226.

[26] J. Ju, Y. Zheng, L. Jiang, *Accounts of chemical research* **2014**, *47*, 2342-2352.

[27] D. Chen, J. Li, J. Zhao, J. Guo, S. Zhang, T. A. Sherazi, S. Li, *Journal of colloid and interface science* **2018**, *530*, 274-281.

[28] P. Comanns, *Journal of Experimental Biology* **2018**, *221*, jeb153130.

[29] J. Li, Z. Guo, *Nanoscale* **2018**, *10*, 13814-13831.

[30] X. Wang, J. Zeng, X. Yu, C. Liang, Y. Zhang, *Applied Surface Science* **2019**, *465*, 986-994.

[31] P. Zhu, R. Chen, C. Zhou, Y. Tian, L. Wang, *Chemical engineering journal (Lausanne, Switzerland : 1996)* **2021**, *415*, 128944.

[32] M. N. Uddin, F. J. Desai, M. M. Rahman, R. Asmatulu, *Nanoscale advances* **2020**, *2*, 4627-4638.

[33] P. Moazzam, H. Tavassoli, A. Razmjou, M. E. Warkiani, M. Asadnia, *Desalination* **2018**, *429*, 111-118.

[34] J. Ju, K. Xiao, X. Yao, H. Bai, L. Jiang, *Advanced Materials* **2013**, *25*, 5937-5942.

[35] J. Li, R. Ran, H. Wang, Y. Wang, Y. Chen, S. Niu, P. E. Arratia, S. Yang, *Nature communications* **2021**, *12*, 1-8.

[36] Y. Shi, O. Ilic, H. A. Atwater, J. R. Greer, *Nature communications* **2021**, *12*, 2797-2797.

[37] W. Gindl-Altmutter, J. Keckes, *BioResources* **2012**, *7*, 1232-1237.

[38] M. E. Malainine, A. Dufresne, D. Dupeyre, M. Mahrouz, R. Vuong, M. R. Vignon, *Carbohydrate Polymers* **2003**, *51*, 77-83.

[39] M. Vignon, L. Heux, M.-E. Malainine, M. Mahrouz, *Carbohydrate Research* **2004**, *339*, 123-131.

[40] Y. Peng, Y. He, S. Yang, S. Ben, M. Cao, K. Li, K. Liu, L. Jiang, *Advanced functional materials* **2015**, *25*, 5967-5971.

[41] M. Cao, J. Ju, K. Li, S. Dou, K. Liu, L. Jiang, *Advanced functional materials* **2014**, *24*, 3235-3240.

[42] H. Zhou, M. Zhang, C. Li, C. Gao, Y. Zheng, *Small (Weinheim an der Bergstrasse, Germany)* **2018**, *14*, e1801335-n/a.

[43] Y. Cheng, S. Zhang, S. Liu, J. Huang, Z. Zhang, X. Wang, Z. Yu, S. Li, Z. Chen, Y. Zhao, Y. Lai, X. Qian, C. Xiao, *Journal of cleaner production* **2021**, *315*, 127862.

[44] X. Heng, M. Xiang, Z. Lu, C. Luo, *ACS applied materials & interfaces* **2014**, *6*, 8032-8041.

[45] S. Yi, J. Wang, Z. Chen, B. Liu, L. Ren, L. Liang, L. Jiang, *Advanced Materials Technologies* **2019**, *4*, 1900727.

[46] S. Feng, J. Delannoy, A. Malod, H. Zheng, D. Quéré, Z. Wang, *Science advances* **2020**, *6*, eabb4540-eabb4540.

[47] M. Mohamed, G. William, M. Fatouh, *Solar Energy* **2017**, *148*, 98-109.

[48] H. Jarimi, R. Powell, S. Riffat, *International Journal of Low-Carbon Technologies* **2020**, *15*, 253-276.

[49] L. Chen, X. Zhang, X. Cheng, Z. Xie, Q. Kuang, L. Zheng, *Nanoscale Advances* **2020**, *2*, 2628-2647.

[50] H. Li, M. Eddaoudi, M. O'Keeffe, O. M. Yaghi, *Nature* **1999**, *402*, 276-279.

[51] C. Janiak, *Angewandte Chemie (International ed.)* **1997**, *36*, 1431-1434.

[52] H. Li, M. Eddaoudi, T. L. Groy, O. M. Yaghi, *Journal of the American Chemical Society* **1998**, *120*, 8571-8572.

[53] I. A. Lazaro, R. S. Forgan, *Coordination Chemistry Reviews* **2019**, *380*, 230-259.

[54] C. Qiao, R. Zhang, Y. Wang, Q. Jia, X. Wang, Z. Yang, T. Xue, R. Ji, X. Cui, Z. Wang, *Angewandte Chemie (International ed.)* **2020**, *59*, 16982-16988.

[55] P. A. Kobielska, A. J. Howarth, O. K. Farha, S. Nayak, *Coordination chemistry reviews* **2018**, *358*, 92-107.

[56] X. Qian, R. Zhang, L. Chen, Y. Lei, A. Xu, *ACS sustainable chemistry & engineering* **2019**, *7*, 16007-16012.

[57] M. Maes, S. Schouteden, L. Alaerts, D. Depla, D. E. De Vos, *Physical chemistry chemical physics : PCCP* **2011**, *13*, 5587-5589.

[58] Z. Hasan, S. H. Jhung, *Journal of hazardous materials* **2015**, *283*, 329-339.

[59] S. M. Towsif Abtab, D. Alezi, P. M. Bhatt, A. Shkurenko, Y. Belmabkhout, H. Aggarwal, Ł. J. Weseliński, N. Alsadun, U. Samin, M. N. Hedhili, M. Eddaoudi, *Chem* **2018**, *4*, 94-105.

[60] A. Cadiau, J. S. Lee, D. Damasceno Borges, P. Fabry, T. Devic, M. T. Wharmby, C. Martineau, D. Foucher, F. Taulelle, C.-H. Jun, Y. K. Hwang, N. Stock, M. F. De Lange, F. Kapteijn, J. Gascon, G. Maurin, J.-S. Chang, C. Serre, *Advanced materials (Weinheim)* **2015**, *27*, 4775-4780.

[61] H. Furukawa, F. Gandara, Y.-B. Zhang, J. Jiang, W. L. Queen, M. R. Hudson, O. M. Yaghi, *Journal of the American Chemical Society* **2014**, *136*, 4369-4381.

[62] H. Kim, S. Yang, S. R. Rao, S. Narayanan, E. A. Kapustin, H. Furukawa, A. S. Umans, O. M. Yaghi, E. N. Wang, *Science (American Association for the Advancement of Science)* **2017**, *356*, 430-434.

[63] N. Hanikel, M. S. Prévot, O. M. Yaghi, *Nature nanotechnology* **2020**, *15*, 348-355.

[64] D. Kim, X. Liu, M. S. Lah, *Inorganic Chemistry Frontiers* **2015**, *2*, 336-360.

[65] G. Wißmann, A. Schaate, S. Lilienthal, I. Bremer, A. M. Schneider, P. Behrens, *Microporous and Mesoporous Materials* **2012**, *152*, 64-70.

[66] V. Bon, I. Senkovska, I. A. Baburin, S. Kaskel, *Crystal growth & design* **2013**, *13*, 1231-1237.

[67] D. Cunha, C. Gaudin, I. Colinet, P. Horcajada, G. Maurin, C. Serre, *Journal of Materials Chemistry B* **2013**, *1*, 1101-1108.

[68] J. H. Cavka, S. Jakobsen, U. Olsbye, N. Guillou, C. Lamberti, S. Bordiga, K. P. Lillerud, *Journal of the American Chemical Society* **2008**, *130*, 13850-13851.

[69] A. Schaate, P. Roy, T. Preuße, S. J. Lohmeier, A. Godt, P. Behrens, *Chemistry–A European Journal* **2011**, *17*, 9320-9325.

[70] Y. Hu, Z. Fang, X. Wan, X. Ma, S. Wang, S. Fan, M. Dong, Z. Ye, X. Peng, *Chemical engineering journal (Lausanne, Switzerland : 1996)* **2022**, *430*, 133086.

[71] L. G. Gordeeva, M. M. Tokarev, V. N. Parmon, Y. I. Aristov, *Reaction kinetics and catalysis letters* **1998**, *65*, 153-159.

[72] J. Wang, Y. Dang, A. G. Meguerdichian, S. Dissanayake, T. Kankanam-Kapuge,

S. Bamonte, Z. M. Tobin, L. A. Achola, S. L. Suib, *Environmental science & technology letters* **2020**, *7*, 48-53.

[73] R. Li, Y. Shi, M. Wu, S. Hong, P. Wang, *Nano Energy* **2020**, *67*, 104255.

[74] F. Deng, C. Wang, C. Xiang, R. Wang, *Nano energy* **2021**, *90*, 106642.

[75] Y. Chen, Z. Yu, Y. Ye, Y. Zhang, G. Li, F. Jiang, *ACS nano* **2021**, *15*, 1869-1879.

[76] F. Deng, C. Xiang, C. Wang, R. Wang, *Journal of materials chemistry. A, Materials for energy and sustainability* **2022**, *1*, 6576-6586.

[77] K. Yang, Y. Shi, M. Wu, W. Wang, Y. Jin, R. Li, M. W. Shahzad, K. C. Ng, P. Wang, *Journal of materials chemistry. A, Materials for energy and sustainability* **2020**, *8*, 1887-1895.

[78] H. Shan, Q. Pan, C. Xiang, P. Poredoš, Q. Ma, Z. Ye, G. Hou, R. Wang, *Cell reports physical science* **2021**, *2*, 100664.

[79] S. Zhang, Z. C. Zhang, *Green Chemistry* **2002**, *4*, 376-379.

[80] W. Huang, W. Zhu, H. Li, H. Shi, G. Zhu, H. Liu, G. Chen, *Industrial & engineering chemistry research* **2010**, *49*, 8998-9003.

[81] H. Qi, T. Wei, W. Zhao, B. Zhu, G. Liu, P. Wang, Z. Lin, X. Wang, X. Li, X. Zhang, *Advanced Materials* **2019**, *31*, 1903378.

[82] W. Zhang, Y. Xia, Z. Wen, W. Han, S. Wang, Y. Cao, R.-X. He, Y. Liu, B. Chen, *RSC advances* **2021**, *11*, 35695-33572.

[83] J. Carrete, M. García, J. R. Rodríguez, O. Cabeza, L. M. Varela, *Fluid phase equilibria* **2011**, *301*, 118-122.

[84] J. Xu, X. Liu, X. Ren, G. Gao, *European Polymer Journal* **2018**, *100*, 86-95.

[85] D. A. Gyles, L. D. Castro, J. O. C. Silva Jr, R. M. Ribeiro-Costa, *European Polymer Journal* **2017**, *88*, 373-392.

[86] Y. Guo, J. Bae, Z. Fang, P. Li, F. Zhao, G. Yu, *Chemical Reviews* **2020**, *120*, 7642-7707.

[87] W. Wang, B. Tang, B. Ju, Z. Gao, J. Xiu, S. Zhang, *Journal of Materials Chemistry A* **2017**, *5*, 958-968.

[88] B. Tang, M. Qiu, S. Zhang, *Solar energy materials and solar cells* **2012**, *105*, 242-248.

[89] Y. Yang, X. Yang, L. Fu, M. Zou, A. Cao, Y. Du, Q. Yuan, C.-H. Yan, *ACS Energy Letters* **2018**, *3*, 1165-1171.

[90] A. Entezari, M. Ejeian, R. Wang, *ACS materials letters* **2020**, *2*, 471-477.

[91] A. Entezari, Ejeian, M., & Wang, R, *ACS Materials Letters* **2020**, *2*, 471-477.

[92] F. Ni, N. Qiu, P. Xiao, C. Zhang, Y. Jian, Y. Liang, W. Xie, L. Yan, T. Chen, *Angewandte Chemie International Edition* **2020**, *59*, 19237-19246.

[93] P. A. Kallenberger, M. Fröba, *Communications Chemistry* **2018**, *1*, 1-6.

[94] B. Chen, X. Zhao, Y. Yang, *ACS applied materials & interfaces* **2019**, *11*, 15616-15622.

[95] A. Kabir, M. J. Dunlop, B. Acharya, R. Bissessur, M. Ahmed, *RSC advances* **2018**, *8*, 38100-38107.

[96] M. Wu, R. Li, Y. Shi, M. Altunkaya, S. Aleid, C. Zhang, W. Wang, P. Wang, *Materials Horizons* **2021**, *8*, 1518-1527.

[97] R. Li, Shi, Y., Alsaedi, M., Wu, M., Shi, L., & Wang, P, *Environmental science*

& technology **2018**, *52*, 11367-11377.

[98] J. Xu, T. Li, T. Yan, S. Wu, M. Wu, J. Chao, X. Huo, P. Wang, R. Wang, *Energy & environmental science* **2021**, *14*, 5979-5994.

[99] C. Lei, Y. Guo, W. Guan, H. Lu, W. Shi, G. Yu, *Angewandte Chemie (International ed.)* **2022**, e202200271-e202200271.

[100] S. Aleid, M. Wu, R. Li, W. Wang, C. Zhang, L. Zhang, P. Wang, *ACS Materials Letters* **2022**, *4*, 511-520.

[101] S. Jin, Liu, M., Chen, S., & Gao, C, *European polymer journal* **2008**, *44*, 2162-2170.

[102] H. Zhang, Niu, Q., Wang, N., Nie, J., & Ma, G, *European Polymer Journal* **2015**, *71*, 440-450.

[103] R. Pelton, *Journal of colloid and interface science* **2010**, *348*, 673-674.

[104] J. W. Larson, & McMahon, T. B, *Inorganic Chemistry* **1984**, *23*, 2029-2033.

[105] S. W. Benson, *Journal of Chemical Education* **1965**, *42*, 502.

[106] F. Zhao, Zhou, X., Liu, Y., Shi, Y., Dai, Y., & Yu, G, *Advanced Materials* **2019**, *31*, 1806446.

[107] A. Karmakar, P. G. Mileo, I. Bok, S. B. Peh, J. Zhang, H. Yuan, G. Maurin, D. Zhao, *Angewandte Chemie International Edition* **2020**, *59*, 11003-11009.

[108] A. J. Rieth, A. M. Wright, G. Skorupskii, J. L. Mancuso, C. H. Hendon, M. Dincă, *Journal of the American Chemical Society* **2019**, *141*, 13858-13866.

[109] F. Fathieh, M. J. Kalmutzki, E. A. Kapustin, P. J. Waller, J. Yang, O. M. Yaghi, *Science advances* **2018**, *4*, eaat3198-eaat3198.

[110] Y. Hu, Z. Fang, X. Ma, X. Wan, S. Wang, S. Fan, Z. Ye, X. Peng, *Applied Materials Today* **2021**, *23*, 101076.

[111] H. Maher, T. H. Rupam, K. A. Rocky, R. Bassiouny, B. B. Saha, *Energy* **2021**, 121741.

[112] Q. Wu, W. Su, Q. Li, Y. Tao, H. Li, *ACS Applied Materials & Interfaces* **2021**.

[113] Y. Tao, Q. Li, Q. Wu, H. Li, *Materials Horizons* **2021**, *8*, 1439-1445.

[114] X. Wang, X. Li, G. Liu, J. Li, X. Hu, N. Xu, W. Zhao, B. Zhu, J. Zhu, *Angewandte Chemie* **2019**, *131*, 12182-12186.

[115] X. Liu, W. Wang, S. Xie, Q. Pan, *Scientific Reports* **2021**, *11*, 1-10.

[116] C. Li, J. Zhu, M. Zhou, S. Zhang, X. He, *Materials* **2019**, *12*, 1782.

[117] D. K. Nandakumar, Zhang, Y., Ravi, S. K., Guo, N., Zhang, C., & Tan, S. C, *Advanced Materials* **2019**, *31*, 1806730.

[118] G. Yilmaz, Meng, F. L., Lu, W., Abed J., Peh, C. K. N., Gao, M., ... & Ho, G. W, *Science advances* **2020**, *6*, eabc8605.

[119] J. Lord, A. Thomas, N. Treat, M. Forkin, R. Bain, P. Dulac, C. H. Behroozi, T. Mamutov, J. Fongheiser, N. Kobilansky, *Nature* **2021**, *598*, 611-617.

[120] M. N. Sharif, H. Haider, A. Farahat, K. Hewage, R. Sadiq, *Environmental reviews* **2019**, *27*, 519-544.

[121] J. Nycander, M. Hieronymus, F. Roquet, *Geophysical research letters* **2015**, *42*, 7714-7721.

[122] D. Vollmer, I. J. Harrison, *Environmental research letters* **2021**, *16*, 011005.

[123] V. Srinivasan, E. F. Lambin, S. M. Gorelick, B. H. Thompson, S. Rozelle, *Water*

resources research **2012**, *48*, n/a.

[124] J. Y. Suen, M. T. Fang, P. M. Lubin, *IEEE transactions on terahertz science and technology* **2014**, *4*, 86-100.

[125] C. Prigent, C. Jimenez, P. Bousquet, *Journal of geophysical research. Atmospheres* **2020**, *125*, e2019JD030711-n/a.

[126] V. G. Gude, *Reviews in environmental science and biotechnology* **2017**, *16*, 591-609.

[127] D. T. Degefie, T. S. El-Madany, M. Held, J. Hejkal, E. Hammer, J. C. Dupont, M. Haeffelin, E. Fleischer, O. Klemm, *Atmospheric research* **2015**, *164-165*, 328-338.

[128] A. Entezari, O. C. Esan, X. Yan, R. Wang, L. An, *Advanced materials (Weinheim)* **2023**, e2210957-e2210957.

[129] F. Deng, Z. Chen, C. Wang, C. Xiang, P. Poredoš, R. Wang, *Advanced science* **2022**, *9*, 2204724-n/a.

[130] Z. Chen, S. Song, B. Ma, Y. Li, Y. Shao, J. Shi, M. Liu, H. Jin, D. Jing, *Solar energy materials and solar cells* **2021**, *230*, 111233.

[131] M. G. Gado, M. Nasser, A. A. Hassan, H. Hassan, *Process safety and environmental protection* **2022**, *160*, 166-183.

[132] X. Zhou, H. Lu, F. Zhao, G. Yu, *ACS Materials Letters* **2020**, *2*, 671-684.

[133] H. Lu, W. Shi, Y. Guo, W. Guan, C. Lei, G. Yu, *Advanced materials (Weinheim)* **2022**, *34*, e2110079-n/a.

[134] W. Shi, W. Guan, C. Lei, G. Yu, *Angewandte Chemie* **2022**, *134*, n/a.

[135] H. Furukawa, F. Gándara, Y.-B. Zhang, J. Jiang, W. L. Queen, M. R. Hudson, O. M. Yaghi, *Journal of the American Chemical Society* **2014**, *136*, 4369-4381.

[136] L. H. Chen, W. K. Han, X. Yan, J. Zhang, Y. Jiang, Z. G. Gu, *ChemSusChem* **2022**, *15*, e202201824-n/a.

[137] H. L. Nguyen, *Advanced materials (Weinheim)* **2023**, *35*, e2300018-n/a.

[138] Y. Liu, W.-K. Han, W. Chi, J.-X. Fu, Y. Mao, X. Yan, J.-X. Shao, Y. Jiang, Z.-G. Gu, *Applied catalysis. B, Environmental* **2023**, *338*, 123074.

[139] S. Jiang, L. Meng, W. Ma, G. Pan, W. Zhang, Y. Zou, L. Liu, B. Xu, W. Tian, *Materials chemistry frontiers* **2021**, *5*, 4193-4421.

[140] N. Li, L. Luo, C. Guo, J. He, S. Wang, L. Yu, M. Wang, P. Murto, X. Xu, *Chemical engineering journal (Lausanne, Switzerland : 1996)* **2022**, *431*, 134144.

[141] X. Sun, S. Agate, K. S. Salem, L. Lucia, L. Pal, *ACS applied bio materials* **2021**, *4*, 140-162.

[142] X. Qu, J. Liu, S. Wang, J. Shao, Q. Wang, W. Wang, L. Gan, L. Zhong, X. Dong, Y. Zhao, *Chemical engineering journal (Lausanne, Switzerland : 1996)* **2023**, *453*, 139785.

[143] H. Sai, A. Erbas, A. Dannenhoffer, D. Huang, A. Weingarten, E. Siismets, K. Jang, K. Qu, L. C. Palmer, M. Olvera de la Cruz, S. I. Stupp, *Journal of materials chemistry. A, Materials for energy and sustainability* **2020**, *8*, 158-168.

[144] P. Verma, A. Singh, F. A. Rahimi, T. K. Maji, *Journal of materials chemistry. A, Materials for energy and sustainability* **2021**, *9*, 1368-13614.

[145] G. Yilmaz, F. L. Meng, W. Lu, J. Abed, C. K. N. Peh, M. Gao, E. H. Sargent, G. W. Ho, *Science advances* **2020**, *6*.

[146] M. Wu, R. Li, Y. Shi, M. Altunkaya, S. Aleid, C. Zhang, W. Wang, P. Wang, *Materials horizons* **2021**, *8*, 1518-1527.

[147] P. A. Kallenberger, M. Fröba, *Communications chemistry* **2018**, *1*.

[148] A. Feng, S. Mao, C. Onggowarsito, G. Naidu, W. Li, Q. Fu, *ACS sustainable chemistry & engineering* **2023**, *11*, 5819-5825.

[149] T. Li, T. Yan, P. Wang, J. Xu, X. Huo, Z. Bai, W. Shi, G. Yu, R. Wang, *Nature water* **2023**, *1*, 971-981.

[150] T. Li, M. Wu, J. Xu, R. Du, T. Yan, P. Wang, Z. Bai, R. Wang, S. Wang, *Nature communications* **2022**, *13*, 6771-6771.

[151] J. Xu, T. Li, J. Chao, S. Wu, T. Yan, W. Li, B. Cao, R. Wang, *Angewandte Chemie* **2020**, *132*, 5240-5248.

[152] N. W. Arnell, *Global environmental change* **1999**, *9*, S31-S49.

[153] M. Salehi, *Environment International* **2022**, *158*, 106936.

[154] C. J. Vorosmarty, P. Green, J. Salisbury, R. B. Lammers, *science* **2000**, *289*, 284-288.

[155] N. W. Arnell, *Global environmental change* **2004**, *14*, 31-52.

[156] B. R. Scanlon, S. Fakhreddine, A. Rateb, I. de Graaf, J. Famiglietti, T. Gleeson, R. Q. Grafton, E. Jobbagy, S. Kebede, S. R. Kolusu, *Nature Reviews Earth & Environment* **2023**, *4*, 87-101.

[157] T. Oki, S. Kanae, *science* **2006**, *313*, 1068-1072.

[158] M. Tomaszkiewicz, M. Abou Najm, D. Beysens, I. Alameddine, M. El-Fadel, *Environmental Reviews* **2015**, *23*, 425-442.

[159] D. Carvajal, J.-G. Minonzio, E. Casanga, J. Muñoz, A. Aracena, S. Montecinos, D. Beysens, *Journal of Water Supply: Research and Technology—AQUA* **2018**, *67*, 357-374.

[160] K. F. Kaseke, L. Wang, *GeoHealth* **2018**, *2*, 327-332.

[161] D. Seo, J. Lee, C. Lee, Y. Nam, *Scientific reports* **2016**, *6*, 1-11.

[162] N. Hanikel, D. Kurandina, S. Chheda, Z. Zheng, Z. Rong, S. E. Neumann, J. Sauer, J. I. Siepmann, L. Gagliardi, O. M. Yaghi, *ACS central science* **2023**, *9*, 551-557.

[163] H. A. Almassad, R. I. Abaza, L. Siwwan, B. Al-Maythalony, K. E. Cordova, *Nature communications* **2022**, *13*, 4873.

[164] S. Laha, T. K. Maji, *Advanced Functional Materials* **2022**, *32*, 2203093.

[165] H. Shan, Q. Pan, C. Xiang, P. Poredoš, Q. Ma, Z. Ye, G. Hou, R. Wang, *Cell reports physical science* **2021**, *2*.

[166] H. Lu, W. Shi, Y. Guo, W. Guan, C. Lei, G. Yu, *Advanced Materials* **2022**, *34*, 2110079.

[167] R. Li, Y. Shi, L. Shi, M. Alsaedi, P. Wang, *Environmental science & technology* **2018**, *52*, 5398-5406.

[168] W. Shi, W. Guan, C. Lei, G. Yu, *Angewandte Chemie* **2022**, *134*, e202211267.

[169] M. Wang, E. Liu, T. Jin, S.-u. Zafar, X. Mei, M.-L. Fauconnier, C. De Clerck, *Water Research* **2023**, 121052.

[170] B. Tashtoush, A. Alshoubaki, *Energy* **2023**, *280*, 128186.

[171] Y. Meng, Y. Dang, S. L. Suib, *Cell Reports Physical Science* **2022**, *3*.

[172] M. Bilal, M. Sultan, T. Morosuk, W. Den, U. Sajjad, M. M. Aslam, M. W. Shahzad, M. Farooq, *International Communications in Heat and Mass Transfer* **2022**, *133*, 105961.

[173] W. Zeng, T. You, W. Wu, *Nano Energy* **2024**, 109572.

[174] S. Mao, A. Feng, S. Zhang, C. Onggowarsito, Q. Chen, D. Su, Q. Fu, *Journal of materials chemistry. A, Materials for energy and sustainability* **2023**, *11*, 2362-2237.

[175] C. Onggowarsito, S. Mao, X. S. Zhang, A. Feng, H. Xu, Q. Fu, *Energy & environmental science* **2024**, *17*, 288-299.

[176] F. Zhao, X. Zhou, Y. Shi, X. Qian, M. Alexander, X. Zhao, S. Mendez, R. Yang, L. Qu, G. Yu, *Nature nanotechnology* **2018**, *13*, 489-495.

[177] X. Zhou, F. Zhao, Y. Guo, Y. Zhang, G. Yu, *Energy & environmental science* **2018**, *11*, 1985-1992.

[178] P. H. Gleick, *Pacific Institute for Studies in Dev., Environment & Security. Stockholm Env. Institute, Oxford Univ. Press. 473p* **1993**, *9*, 1051-0761.

[179] Y. Tu, R. Wang, Y. Zhang, J. Wang, *Joule* **2018**, *2*, 1452-1475.

[180] A. Entezari, M. Ejeian, R. Wang, *Applied thermal engineering* **2019**, *161*, 114109.

[181] J. Xu, T. Li, J. Chao, S. Wu, T. Yan, W. Li, B. Cao, R. Wang, *Angewandte Chemie (International ed.)* **2020**, *59*, 5202-5210.

[182] G. Yilmaz, F. Meng, W. Lu, J. Abed, C. Peh, M. Gao, E. Sargent, G. Ho, *Science advances* **2020**, *6*, eabc8605.

[183] F. Zhao, X. Zhou, Y. Liu, Y. Shi, Y. Dai, G. Yu, *Advanced Materials* **2019**, *31*, 1806446.

[184] E. A. Müller, F. R. Hung, K. E. Gubbins, *Langmuir* **2000**, *16*, 5418-5424.

[185] P. K. Marwah, G. Paik, C. J. Issa, C. C. Jemison, M. B. Qureshi, T. M. Hanna, E. Palomino, K. R. Maddipati, D. Njus, *Neurotoxicology* **2022**, *90*, 10-18.

[186] M. Salomäki, T. Ouvinen, L. Marttila, H. Kivelä, J. Leiro, E. Mäkilä, J. Lukkari, *The Journal of Physical Chemistry B* **2019**, *123*, 2513-2524.

[187] B. Bolto, J. Gregory, *Water research* **2007**, *41*, 2301-2324.

[188] S. Kawamura, *Journal-American Water Works Association* **1991**, *83*, 88-91.

[189] E. M. Wilts, J. Herzberger, T. E. Long, *Polymer International* **2018**, *67*, 799-814.

[190] B. Bolto, *Journal of Water Supply: Research and Technology—AQUA* **2005**, *54*, 531-544.

[191] G. U. Bhaskar, S. Gupta, *Water, Air, and Soil Pollution* **1987**, *35*, 251-260.

[192] P. Wei, W. Chen, Q. Song, Y. Wu, Y. Xu, *Cellulose (London)* **2021**, *28*, 3723-3732.

[193] T. Alonso-García, C. A. Gervasi, M. J. Rodríguez-Presa, E. Gutiérrez-Pineda, S. E. Moya, O. Azzaroni, *Journal of physical chemistry. C* **2013**, *117*, 26680-26688.

[194] I. Yudovin-Farber, N. Beyth, E. I. Weiss, A. J. Domb, *Journal of nanoparticle research : an interdisciplinary forum for nanoscale science and technology* **2009**,

12, 591-603.

[195] A. Cadiau, J. S. Lee, D. Damasceno Borges, P. Fabry, T. Devic, M. T. Wharmby, C. Martineau, D. Foucher, F. Taulelle, C. H. Jun, *Advanced Materials* **2015**, *27*, 4775-4780.

[196] Q. Wu, W. Su, Q. Li, Y. Tao, H. Li, *ACS Applied Materials & Interfaces* **2021**, *13*, 38906-38915.

[197] A. J. Rieth, A. M. Wright, G. Skorupskii, J. L. Mancuso, C. H. Hendon, M. Dincă, *Journal of the American Chemical Society* **2019**, *141*, 13858-13866.

[198] S. M. T. Abtab, D. Alezi, P. M. Bhatt, A. Shkurenko, Y. Belmabkhout, H. Aggarwal, Ł. J. Weseliński, N. Alsadun, U. Samin, M. N. Hedhili, *Chem* **2018**, *4*, 94-105.

[199] H. Maher, T. H. Rupam, K. A. Rocky, R. Bassiouny, B. B. Saha, *Energy* **2022**, *238*, 121741.

[200] M. F. Chaplin, *Water and Life: The unique properties of H2O* **2007**, 69-86.

[201] N. N. Greenwood, A. Earnshaw, *Chemistry of the Elements*, Elsevier, **2012**.

[202] C. Czeslik, J. Jonas, *Chemical physics letters* **1999**, *302*, 633-638.

[203] T. E. de Oliveira, D. Mukherji, K. Kremer, P. A. Netz, *The Journal of chemical physics* **2017**, *146*, 034904.

[204] D. K. Nandakumar, Y. Zhang, S. K. Ravi, N. Guo, C. Zhang, S. C. Tan, *Advanced Materials* **2019**, *31*, 1806730.

[205] F. Fathieh, M. J. Kalmutzki, E. A. Kapustin, P. J. Waller, J. Yang, O. M. Yaghi, *Science advances* **2018**, *4*, eaat3198.

[206] J. Wang, Y. Dang, A. G. Meguerdichian, S. Dissanayake, T. Kankanam-Kapuge, S. Bamonte, Z. M. Tobin, L. A. Achola, S. L. Suib, *Environmental Science & Technology Letters* **2019**, *7*, 48-53.

[207] W. H. Organization, **1963**.

[208] I. M. Sayre, *Journal-American Water Works Association* **1988**, *80*, 53-60.

[209] P. Moszynski, *BMJ* **2006**, *333*, 986-986.

[210] R. Singh, *Journal of membrane science* **2008**, *313*, 353-354.

[211] E. Barbier, *The Water Paradox: Overcoming the Global Crisis in Water Management*, Yale University Press, New Haven, **2019**.

[212] Q. Li, Y. Ying, Y. Tao, H. Li, *Industrial & engineering chemistry research* **2022**, *61*, 1344-1354.

[213] H. Sun, Y. Song, B. Zhang, Y. Huan, C. Jiang, H. Liu, T. Bao, S. Yu, H. Wang, *Applied physics. A, Materials science & processing* **2021**, *127*.

[214] M. P. Silva, A. M. Ribeiro, C. G. Silva, K. Ho Cho, U. H. Lee, J. L. Faria, J. M. Loureiro, J.-S. Chang, A. E. Rodrigues, A. Ferreira, *Separation and purification technology* **2022**, *290*, 120803.

[215] N. Ha, J. Park, S. H. Park, E. Seo, J. H. Lim, S. J. Lee, *The New phytologist* **2021**, *231*, 1906-1922.

[216] T. Miranda, A. Roth-Nebelsick, A. Junginger, M. Ebner, *Flora. Morphologie, Geobotanik, Oekophysiologie* **2020**, *272*, 151692.

[217] S. Allison-Logan, Q. Fu, Y. Sun, M. Liu, J. Xie, J. Tang, G. G. Qiao, *Angewandte Chemie International Edition* **2020**, *59*, 21392-21396.

[218] S. Zhang, J. Fu, S. Das, K. Ye, W. Zhu, T. Ben, *Angewandte Chemie* **2022**, *134*, n/a.

[219] H. Maher, T. H. Rupam, K. A. Rocky, R. Bassiouny, B. B. Saha, *Energy (Oxford)* **2022**, *238*, 121741.

[220] Q. Wu, W. Su, Q. Li, Y. Tao, H. Li, *ACS applied materials & interfaces* **2021**, *13*, 38906-38915.

[221] Y. Tao, Q. Li, Q. Wu, H. Li, *Materials horizons* **2021**, *8*, 1439-1445.

[222] X. Y. Liu, W. W. Wang, S. T. Xie, Q. W. Pan, *Scientific reports* **2021**, *11*, 14412-14412.

[223] H. Qi, T. Wei, W. Zhao, B. Zhu, G. Liu, P. Wang, Z. Lin, X. Wang, X. Li, X. Zhang, J. Zhu, *Advanced materials (Weinheim)* **2019**, *31*, e1903378-n/a.

[224] C. Lei, Y. Guo, W. Guan, H. Lu, W. Shi, G. Yu, *Angewandte Chemie* **2022**, *134*, n/a.

[225] A. Karmakar, P. G. M. Mileo, I. Bok, S. B. Peh, J. Zhang, H. Yuan, G. Maurin, D. Zhao, *Angewandte Chemie* **2020**, *132*, 11096-11102.